RELATIVISTIC MEAN FIELD THEORY: METHODS AND APPLICATIONS

Thesis by

David Allan Wasson

In Partial Fulfillment of the Requirements

for the Degree of

Doctor of Philosophy

California Institute of Technology

Pasadena, California

1990

(Submitted June 23, 1989)

Acknowledgments

First, I would like to thank Steve Koonin for providing me with many interesting projects to work on and for creating a group in which one can freely work on a wide variety of topics. This thesis has also benefited greatly from many useful discussions with Ryoichi Seki, Xiangdong Ji, Robert Perry, Tom Cohen, and Martin Savage.

In addition, I thank all my colleagues and friends in Kellogg over the years for making this a fun place to work. I would particularly like to thank Eric Belz for developing computer software that has had a profound impact on the completion of this thesis. I have also benefited from the warm hospitality of the newly opened fifth floor office complex where most of this thesis was written. Finally, I thank my parents for their support throughout the years.

Financial support during my last three years here was provided AT&T Bell Laboratories. This thesis was written using software written by Dave Potterveld.

Abstract

We develop a method for performing one-loop calculations in finite systems that is based on using the WKB approximation for the high energy states. This approximation allows us to absorb all the counterterms analytically and thereby avoids the need for extreme numerical precision that was required by previous methods. In addition, the local approximation makes this method well suited for self-consistent calculations. We then discuss the application of relativistic mean field methods to the atomic nucleus. Self-consistent, one loop calculations in the Walecka model are performed and the role of the vacuum in this model is analyzed. This model predicts that vacuum polarization effects are responsible for up to five percent of the local nucleon density. Within this framework the possible role of strangeness degrees of freedom is studied. We find that strangeness polarization can increase the kaon-nucleus scattering cross section by ten percent. By introducing a cutoff into the model, the dependence of the model on short-distance physics, where its validity is doubtful, is calculated. The model is very sensitive to cutoffs around one GeV.

Table of Contents

List of Figures

List of Tables

Chapter 1
Introduction

This thesis studies many-particle systems in which relativistic effects are important. The focus is on mean-field theory. In this introduction, we first compare relativistic and non-relativistic many-particle systems. We then discuss various physical systems of interest where relativistic effects are important. Finally, we give an overview of the organization of this thesis.

1.1 Relativistic vs. Non-Relativistic Systems

In order to appreciate the issues involved with relativistic systems, we first review non-relativistic systems. A non-relativistic system of N fermions is typically described by a Hamiltonian,

$$H = \sum_i \frac{p_i^2}{2m} + \sum_{i<j} V(\mathbf{r}_i - \mathbf{r}_j), \tag{1.1}$$

where $V(\mathbf{r}_i - \mathbf{r}_j)$ represents the instantaneous energy of interaction between two particles. The quantum mechanical state of the fermions is described by the wavefunction

$$\Psi(\mathbf{r}_1, ..., \mathbf{r}_N) \tag{1.2}$$

that is antisymmetric under the interchange of particles and obeys

$$H\,\Psi(\mathbf{r}_1, ..., \mathbf{r}_N) = E\,\Psi(\mathbf{r}_1, ..., \mathbf{r}_N) \tag{1.3}$$

where E is the energy of the system. Fortunately, many of the systems of interest in nature are sufficiently semiclassical in nature that the wavefunction is much simpler than (1.3) [1] . In the semiclassical limit we can effectively describe each particle by its own single particle wavefunction, $\psi(\mathbf{x}_i)$. The resulting antisymmetrized many-body wavefunction in the Hartree-Fock approximation is

$$\Psi_{HF}(\mathbf{x}) = \frac{1}{\sqrt{N!}}\det[\psi_i(\mathbf{x}_j)]. \tag{1.4}$$

The ground state, in this approximation, is determined by minimizing H in the space of all Hartree-Fock wavefunctions yielding Schrodinger like equations for the single particle wavefunctions,

$$[-\frac{\hbar^2}{2m}\nabla^2 + U(\{\psi_j\})\,]\psi_i(\mathbf{x}) = \epsilon_i\psi_i(\mathbf{x}). \tag{1.5}$$

The potential U consists of both a local mean field generated by all the wavefunctions and a non-local piece that is due to the Pauli-exclusion principle. Specifying which single particle wavefunctions are occupied generates a self-consistent potential U. The ground state has the lowest N energy single-particle states occupied, as shown in Fig. 1.1.

Corrections beyond the Hartree-Fock approximation correspond to the introduction of correlations into the many particle wavefunction. When expressed in terms of a single-particle basis, the correlations appear as the mixture of particle-hole excitations into the wavefunction.

There are basically two reasons for which a many-body system will require a relativistic treatment. The first is kinematics. If the particles in the system are moving at relativistic speeds, then they must be described by relativistic equations.

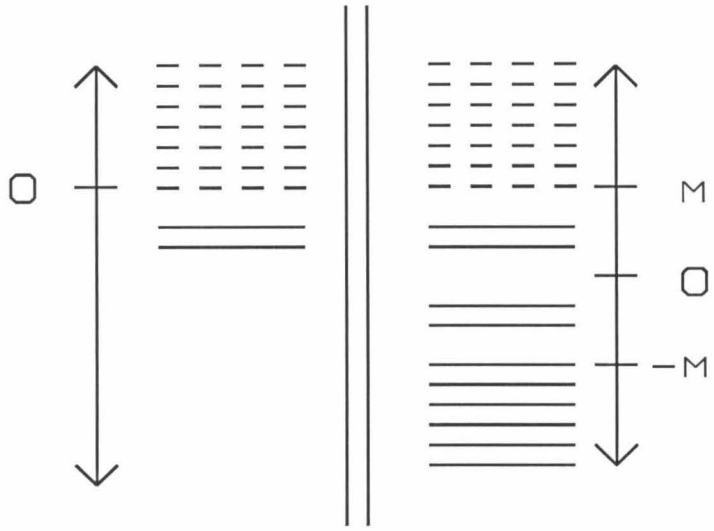

Figure 1.1 – Comparison of the non-relativistic and relativistic Hartree approximations for a system of fermions. Solid lines represent filled single particle levels and dashed lines empty single particle levels. The left side shows the non-relativistic levels and the right side the relativistic levels. In addition to the occupied valence orbitals, the relativistic system also consists of an infinite number of occupied negative energy orbitals greatly increasing the complexity of the system.

In additon, the retardation effects of their mutual interaction will be important. This leads to the replacement of the interaction potential by a field that mediates the interaction between the particles. Hence, relativistic systems need to be described by a Lagrangian such as

$$\mathcal{L} = \bar{\psi}(i\gamma^\mu \partial_\mu - m + g\phi)\psi + \frac{1}{2}\partial^\mu \phi \partial_\mu \phi - V(\phi). \tag{1.6}$$

This particular Lagrangian describes fermions of mass m interacting via a scalar field ϕ. When treating this system quantum mechanically, we need to quantize both the

fermion and meson degrees of freedom [2] . In such systems the vacuum takes on a complicated structure. The quantization of the fermions requires the existence of antifermions, and the resulting fermion vacuum is made of virtual fluctuations of fermion-antifermion pairs. In addition, the meson vacuum consists of the zero point fluctuations of the meson field.

This leads us to the second reason for which a many-body system requires a relativistic treatment. The presence of a bound system perturbs the vacuum, inducing a non-zero energy density in the vacuum. Since the system minimizes the total energy, this vacuum energy can play a large role in determining the structure of the system. This implies that all relativistic many-body problems are effectively infinite body problems and it is the primary reason that solving for relativistic bound states is much more difficult than for non-relativistic bound states. Finally note that these vacuum perturbations can be significant even if the velocities of the valence particles are non-relativisitic.

Like the non-relativistic many-body problem, the relativistic many-body problem simplifies in the semiclassical limit [3] . In this limit, the meson fields are replaced by their expectation values and the fermions are described in terms of single-particle wavefunctions that obey the Dirac equation

$$(-i\alpha \cdot \nabla - \beta(M - g_s\phi) - g_V V^0)\psi_i(\mathbf{x}) = \epsilon_i \psi_i(\mathbf{x}), \tag{1.7}$$

where ϕ is a scalar mean field and V^0 is a time component of a vector mean field. In general, much more complicated mean-field Lorentz structure is possible.

For a given mean-field, the energy eigenvalues take on both positive and negative values and are unbound from both above and below as opposed to the non-relativistic

single-particle energies that are bounded from below. In a non-interacting system the eigenvalues are

$$\epsilon^0_{\mathbf{k}} = \pm\sqrt{\mathbf{k}^2 + m^2}. \tag{1.8}$$

In order to maintain a stable system, one assumes that all the negative energy states are occupied. Holes in these states are interpreted as antiparticles. When the interaction is turned on, one follows the same prescription of filling up all the negative energy orbitals of the interacting system. Hence, a relativistic system with fermi energy ϵ_f has all its positive energy orbitals filled up to ϵ_f and its negative energy orbitals totally filled up as shown in Figure 1.1.

The energy of the fermions relative to the vacuum is

$$E_{\text{fermi}} = \sum_{0<\epsilon_i<\epsilon_f} \epsilon_i + \sum_{\epsilon_i<0} \epsilon_i - \epsilon^0_i. \tag{1.9}$$

The second term in (1.8) is the contribution that is due to the perturbation of the vacuum that is absent non-relativistically. This bare sum is generally infinite and is made finite by the renormalization procedure. As the ground state of the interacting system minimizes the total energy, this term can play a crucial role in determining the structure of the system. The perturbation of the Dirac sea contributes mass to the system and non-zero particle densities that act as an additional source term for the meson field. This approximation goes by the names of relativistic Hartree approximation (RHA) and one-fermion-loop approximation.

The first-order corrections to this approximation are obtained by introducing fluctuations into the mean meson fields. The meson vacuum consists of the zero-point fluctuations of the meson fields. The presence of the mean meson field disrupts

these fluctuations generating an energy,

$$E_{\rm bl} = \frac{1}{2}\sum_i(\omega_i - \omega_i^0), \tag{1.10}$$

which is known as the one-boson-loop approximation. The most famous example of this type of effect is the Casimir effect [4]. The presence of two conducting plates disturbs the vacuum modes of the electromagnetic field, lowering the energy of the vacuum. The closer the plates are placed, the lower the vacuum energy resulting in an attractive force between the two plates.

1.2 Physical Systems of Interest

Currently relativistic mean-field methods are used to study large-Z atoms, construct models of nucleons, and to construct models of the nucleus. The vacuum is known to be very important in the first two and its role in the third system is currently a subject of speculation.

Historically, the first system that these methods have been used to study is the atomic structure around highly charged ions. As the charge of the nucleus increases, the negative energy electron states become highly deformed, resulting in an increasing vacuum polarization charge density being induced around the nucleus. Since the charge is conserved, this polarization density has net charge zero and consists of negative charge near the nucleus and positive charge far away. This effect can be understood qualitatively by thinking of the vacuum as fluctuating electron-positron pairs in which case the electrons are attracted and the positrons repelled, setting up the vacuum polarization charge density. The effects of this on the postive enegy orbitals are well established for both electron and muon orbitals and are well understood using the Relativistic Hartree Approximation [5].

When the charge becomes large enough, the binding energy of the most bound electron becomes larger than $2m_e c^2$, in which case it is energetically favorable to create an $e^+ e^-$ pair with the e^- occupying the bound orbital and the positron escaping to infinity. Such large charges can be created by colliding two heavy ions at low energies ($\sim$ the Coulomb barrier). Although single positron emission has not been identified, narrow $e^+ e^-$ peaks have been observed. The origin of these peaks is currently a mystery. One line of thought is that these peaks might have an origin in the dynamics of the vacuum polarization structure in the highly charged environment, although to date no one has been able to perform a reliable calculation of the dynamics [6].

The next system where the vacuum plays a very important role is the structure of the nucleon [7] . The vacuum of QCD breaks the chiral invariance of the QCD Lagrangian. When interacting in this vacuum, quarks are confined. At short distances, however, perturbative QCD provides a good description. These two extremes of behavior are usually incorporated in terms of bag models. The nucleon is modeled as a bag, the outside of which is the real vacuum and the inside of which is the perturbative vacuum. Since the perturbative vacuum is higher energy than the real vacuum, it costs energy to increase the size of the bag. The valence quarks are confined inside the bag, and the competition between the uncertainty principle and the vacuum energy gives the nucleon a finite radius.

Confining the quarks in the bag results in a non-vanishing axial current at the bag boundary. This current can be absorbed by putting pions in the vacuum outside the bag and allowing them to form the $r > R$ portion of the skyrmion. The problem now is that the skyrmion generates non-zero baryon number outside the bag. This problem is surmounted by considering the negative energy quarks inside of the bag. The bag boundary conditions are not CP invariant, resulting in a negative baryon

number being generated in the vacuum inside of the bag. This baryon number exactly cancels the baryon number carried in the skyrmion outside the bag. Hence, by treating the inside of the bag in the relativistic Hartree approximation and the outside via a classical meson solution, a self-consistent nucleon model can be constructed that is the best currently available [7].

Given that the vacuum is so strongly perturbed in a nucleon, one might also expect that a nucleon would also strongly perturb the strange sector of the vacuum, resulting, for instance, in a strong scalar strangeness density being induced in the vacuum. This idea is currently a subject of much interest. Another idea is that the structure of the vacuum will be altered slightly in nuclear matter. Since the vacuum plays a large role in determining the structure of the nucleon, we would expect that this would cause the properties of nucleons in nuclear matter to change. Several models of the nucleon, in fact, predict that nucleons will swell by $\sim 10\%$ in nuclear matter [8] .

Within relativistic nuclear models [9] , it is also found that vacuum effects in the nucleus occur. This happens because the nuclear mean field in these models consists of a scalar and a vector piece that are individually large but essentially cancel each other in nuclear matter. The negative energy states , however, see the sum of these two fields. Using the same qualitative arguments as were applied to vacuum polarization around highly charged ions, we would expect to see non-negligible vacuum polarization effects in nuclei if these models are correct.

1.3 Organization of this Thesis

This thesis is organized as follows. Chapter 2 introduces the relativistic Hartree approximation along with the one-boson-loop approximation and studies their behavior in uniform systems. The calculation of these approximations for finite systems

is then discussed and local approximation methods are reviewed. Chapter 3 develops our method for performing these calculations in $1+1$ dimensional systems and Chapter 4 extends these methods to $3+1$ dimensions. This method is based on on the realization that the perturbation of the high energy states can be successfully treated using the WKB approximation. In Chapter 5 we apply the relativistic Hartree approximation to relativistic models of the nucleus. Here we discuss both the predictions and the validity of these models.

Chapter 2
The Relativistic Hartree Approximation

This chapter develops the relativistic Hartree approximation and its perturbative corrections via a saddle-point evaluation of the path integral. The first section reviews the effective action formalism that allows us to calculate the energy functional of the system in terms of a path integral, which when extremized gives the ground state of the system. The second section discusses the one-loop approximation to the effective action and sets up our general notation for one-loop calculations. The third section discusses one-loop corrections for uniform systems. The fourth section discusses finite systems and reviews various local approximations.

2.1 Effective Action Formalism

A thorough review of the effective action formalism is given in [10]. In this section, we review the aspects of the formalism that we will need in this thesis.

We begin by reviewing the simplest case of a self-interacting scalar field in $n+1$ dimensions as described by a Lagrangian $L = \int d^{(n+1)}x\, \mathcal{L}$ (our notation is $d^{(n+1)}x = d^n x dt$), where

$$\mathcal{L} = \frac{1}{2}\partial^\mu \phi \partial_\mu \phi - V(\phi). \tag{2.1}$$

Classically, this Lagrangian determines the dynamics of the classical field ϕ via the stationarity requirement

$$\frac{\delta L}{\delta \phi(x)} = 0 \Rightarrow \frac{\partial \mathcal{L}}{\partial \phi} - \partial_\mu \frac{\partial \mathcal{L}}{\partial(\partial_\mu \phi)} = 0. \tag{2.2}$$

In general, these equations will admit static solutions and time-varying solutions. All of these solutions correspond to a conserved energy that is calculated via the Hamiltonian $H = \int d^n x \, \mathcal{H}$, where

$$\mathcal{H} = \frac{1}{2}\left(\Pi^2 + |\nabla\phi|^2\right) + V(\phi) \tag{2.3}$$

and Π is conjugate momentum density,

$$\Pi = \frac{\partial \mathcal{L}}{\partial \partial_0 \phi} = \partial^0 \phi. \tag{2.4}$$

Static solutions have $\Pi = 0$ and $\mathcal{L} = -\mathcal{H}$ and hence satisfy

$$\frac{\delta H}{\delta \phi} = 0, \tag{2.5}$$

where the variation is with respect to static field configurations.

Quantum mechanically, ϕ and Π change from classical fields to operators that obey the commutation relation

$$[\phi(x,t), \Pi(x',t')] = i\hbar\delta^n(x-x')\delta(t-t'). \tag{2.6}$$

The system is characterized by state vectors $|\Psi(t)\rangle$ that obey the Schrodinger equation

$$H|\Psi(t)\rangle = i\hbar\frac{\partial}{\partial t}|\Psi(t)\rangle, \tag{2.7}$$

resulting in static solutions of energy E that evolve in time as

$$|\Psi(t)\rangle = \exp(-iEt)|\Psi(0)\rangle \tag{2.8}$$

and have an expectation value of the scalar field, $\bar{\phi}$, given by

$$\bar{\phi}(x) = \langle \Psi | \phi(x) | \Psi \rangle. \tag{2.9}$$

The quantum-mechanical problem is much more complicated than the corresponding classical problem. Nonetheless, it is possible to reformulate the quantum problem in the same language as the classical problem. This is done by constructing an effective action that is a functional of the expectation values of the scalar field. The physical states extremize the effective action, yielding the energy and scalar field expectation value of the quantum state.

First consider the calculation of the energy E and the expectation value of the scalar field, $\bar{\phi}(x) = \langle 0 | \phi(x) | 0 \rangle$, for the ground state $|0\rangle$. The energy E is related to the ground-state to ground-state amplitude Z as

$$\lim_{t \to \infty} e^{-iEt} = \lim_{t \to \infty} \langle 0 | e^{-iHt} | 0 \rangle = Z, \tag{2.10}$$

and hence the energy can be calculated from Z as

$$E \int dt = i \ln Z. \tag{2.11}$$

The ground-state to ground-state transition amplitude is given by the path integral,

$$Z = \int \mathcal{D}\phi \exp[i \int d^{(n+1)}x \, \mathcal{L}(\phi)]. \tag{2.12}$$

The expectation value of the scalar field can also be calculated directly in terms of a path integral as

$$\bar{\phi}(x) = \frac{\int \mathcal{D}\phi \, \phi(x) \exp[i \int d^{(n+1)}x \, \mathcal{L}(\phi)]}{\int \mathcal{D}\phi \exp[i \int d^{(n+1)}x \, \mathcal{L}(\phi)]}. \tag{2.13}$$

In order to generate the effective action, which for static systems is just minus the energy density, the energy associated with an arbitrary expectation value of the scalar field must be calculated. This is done within the path integral formalism by introducing a time-independent external source, $J(x)$, such that the expectation value of the scalar field is now some function $\phi_{cl}(x)$ that can be adjusted to any desired value by varying $J(x)$. The source is introduced by adding an additional term to the Lagrangian (2.1), $\mathcal{L}(\phi) \rightarrow \mathcal{L}(\phi) + J(x)\phi(x)$. The ground state of the system $|0\rangle_J$ now has energy

$$E[J] \int dt = i \ln Z[J] \equiv -\Omega[J] \tag{2.14}$$

and scalar field expectation value

$$\phi_{cl}(x) = \langle 0|\phi(x)|0\rangle = -i\frac{1}{Z[J]}\frac{\delta}{\delta J(x)}Z[J] = \frac{\delta}{\delta J(x)}\Omega[J] \tag{2.15}$$

where

$$Z[J] = \int \mathcal{D}\phi \exp[i \int d^{(n+1)}x \, \mathcal{L}(\phi) + J\phi]. \tag{2.16}$$

This energy is the sum of the energy of interaction of the scalar field with the external source and of the scalar field with itself. The energy that is due to the mutual interaction of the scalar field is extracted from (2.14) by subtracting off the contribution that is due to the external source (mathematically, a Legendre transformation), generating the effective action

$$S_{\text{eff}} = \Omega[J] - \int d^{(n+1)}x \, \phi_{cl}(x) J(x). \tag{2.17}$$

If ϕ_{cl} and $J(x)$ are regarded as independent functions, then from (2.15) it follows that S_{eff} is independent of J and hence $S_{\text{eff}} = S_{\text{eff}}(\phi_{cl})$. Differentiating (2.17) implies

$$\frac{\delta S_{\text{eff}}}{\delta \phi_{cl}(x)} = J(x). \tag{2.18}$$

Since $\phi_{cl}(x) = \bar{\phi}(x)$ when $J = 0$, the effective action is extremized at the expectation value of ϕ corresponding to the exact ground state, and from (2.14) the energy of this state is

$$E \int dt = -S_{\text{eff}}(\bar{\phi}). \tag{2.19}$$

The effective action can be calculated by performing the path integral (2.16). Exact evaluation of such path integrals, particularly for the non-asymptotically free theories that are dealt within this thesis, is not feasible. Hence, various approximation schemes need to be used. One method, to be discussed in the next section, is based on performing a saddle-point evaluation of this integral. It is also worth noting that the effective action is simply related to the Green's functions of the theory, for which a variety of approximation techniques are available. In particular the coefficients,Γ^n, of the functional Taylor series expansion of $S_{\text{eff}}(\phi_{cl})$ relative to the effective action evaluated at $\bar{\phi}$,

$$S_{\text{eff}}(\phi_{cl}) - S_{\text{eff}}(\bar{\phi}) = \sum_{n=1}^{\infty} \frac{1}{n!} \int d^4x_1 \cdots d^4x_n \Gamma^n(x_1, ..., x_n) \eta_{cl}(x_1) \cdots \eta_{cl}(x_n) \tag{2.20}$$

where $\eta(x) = \phi_{\text{cl}}(x) - \bar{\phi}(x)$, correspond to $-i$ times the one particle irreducible n-point functions of the field theory [2]. Hence, any set of one particle irreducible Feynman diagrams can be used to generate an approximation to S_{eff}.

The preceding formalism generalizes straightforwardly to other meson fields and fermions. For instance, if fermions are added so that the Lagrangian becomes

$$\mathcal{L} = \frac{1}{2}\partial^\mu \phi \partial_\mu \phi - V(\phi) + \bar{\psi}(i\partial\!\!\!/ - g\phi)\psi, \tag{2.21}$$

then $Z[J]$ is calculated by a functional integral over both the meson and fermion fields as

$$Z[J] = \int \mathcal{D}\phi\mathcal{D}\psi\mathcal{D}\bar{\psi}\exp[i\int d^{(n+1)}x\,\mathcal{L}(\phi,\psi,\bar{\psi}) + J(x)\phi(x)]. \tag{2.22}$$

Z[J] represents the ground-state to ground-state amplitude for states with zero baryon number. Usually, it is interesting to study systems with valence fermions, in which case there is a net baryon number. The above formalism still applies, with the vacuum state $|0\rangle$ referring to the ground state at finite baryon number. Finite baryon number is implemented into the formalism by adding a lagrange multiplier to the Lagrangian, $\mathcal{L} \rightarrow \mathcal{L} + \mu_f\psi^\dagger\psi$, which constrains the system to be at finite density. The generating functional is now

$$Z[J] = \int \mathcal{D}\phi\mathcal{D}\psi\mathcal{D}\bar{\psi}\exp[i\int d^{(n+1)}x\,\mathcal{L}(\phi,\psi,\bar{\psi}) + J(x)\phi(x) + \mu_f\psi^\dagger\psi] \tag{2.23}$$

and the effective action (2.17) gives the free energy of the system

$$\frac{-1}{\int dt}S_{\text{eff}} = \langle 0|H|0\rangle - \mu_f\langle 0|\psi^\dagger\psi|0\rangle. \tag{2.24}$$

2.2 One-Loop Approximation

It is straightforward to calculate the effective action in the semiclassical limit. The general methods are reviewed in [11] . The specific application to finite systems is due to Dashen, Hasslacher, and Neveu and is thoroughly described in [3]. We now review this method.

The basic idea is that in the semiclassical limit, each static field configuration $\tilde{\phi}$ that is a solution of the classical equation of motion with classical energy $\tilde{E}$ will correspond to some static quantum state $|\tilde{\phi}\rangle$ that has the same energy $\tilde{E}$; i.e., $|\tilde{\phi},t\rangle =$

$\exp[-it\int d^3x\mathcal{H}(\tilde{\phi})]|\tilde{\phi},0\rangle$. This connection, and its quantum corrections, can be made quantitative by evaluating the path integral of the generating functional in the saddle-point approximation.

First consider the scalar boson theory given by the Lagrangian (2.1). Let $\tilde{\phi}$ be a solution of the classical equation of motion in the presence of an external source J,

$$\frac{\delta[\int d^{(n+1)}x\,\mathcal{L}(\phi)+J(x)\phi(x)]}{\delta\phi}\Big|_{\phi=\tilde{\phi}}=0\Rightarrow\partial^\mu\partial_\mu\tilde{\phi}+V'(\tilde{\phi})=J(x). \tag{2.25}$$

It is convenient to add a total derivative to the action to bring it into the form

$$\mathcal{L}=-\frac{1}{2}\phi\partial^\mu\partial_\mu\phi-V(\phi)+J\phi. \tag{2.26}$$

Taylor expanding $\mathcal{L}(\phi)+J(x)\phi(x)$ about the classical solution results in

$$\mathcal{L}(\tilde{\phi}+\eta)+J(x)(\tilde{\phi}+\eta)=\mathcal{L}(\tilde{\phi})+J(x)(\tilde{\phi})+\frac{1}{2}\left[\partial^\mu\eta\partial_\mu\eta-V''(\tilde{\phi})\eta^2\right]+\mathcal{O}(\eta^3). \tag{2.27}$$

Assuming that only field configurations close to the classical solution contribute, the path integral results can be approximated as

$$Z[J]=\exp\left[i\int d^nx\,\mathcal{L}(\tilde{\phi})+J(x)\tilde{\phi}\right]\int\mathcal{D}\eta\,\exp\left[\frac{i}{2}\int d^4x\,\eta\{-\partial^\mu\partial_\mu-V''(\tilde{\phi})+i\epsilon\}\eta\right], \tag{2.28}$$

where an integration by parts has been performed in the integrand of the action and a term $i\epsilon\eta^2$ has been added in to make the path integral convergent, with limit $\epsilon\to 0$ being taken at the end of the calculation. The resulting Gaussian path integral is $\left[\det(-\partial^\mu\partial_\mu-V''(\tilde{\phi})+i\epsilon)\right]^{-1/2}$ that when combined with the identity $\det(A)=\exp(\mathrm{Tr}\log A)$ gives

$$Z[J]=\exp\left[i\left([\int d^{(n+1)}x\mathcal{L}(\tilde{\phi})+J\tilde{\phi}]+\frac{i}{2}Tr\log[-\partial^\mu\partial_\mu-V''(\tilde{\phi})+i\epsilon]\right)\right], \tag{2.29}$$

implying

$$\Omega[J] = \int d^{(n+1)}x\mathcal{L}(\tilde{\phi}) + J\tilde{\phi} + \frac{i}{2}\langle x|\log[-\partial^\mu\partial_\mu - V''(\tilde{\phi}) + i\epsilon]|x\rangle, \tag{2.30}$$

where we have evaluated the trace as $\mathrm{Tr}A = \int d^{(n+1)}x\langle x|A|x\rangle$. Functionally differentiating Ω with respect to J determines ϕ_{cl} to be

$$\phi_{cl} = \frac{\delta\Omega}{\delta J} = \tilde{\phi}. \tag{2.31}$$

The effective action is now determined via (2.17) to be

$$S_{\text{eff}}(\phi_{cl}) = \int d^{(n+1)}x\,\mathcal{L}(\phi_{cl}) + \mathcal{L}^{(1)}(\phi_{cl}), \tag{2.32}$$

where

$$\mathcal{L}^{(1)}(\phi_{cl}) = \frac{i}{2}\langle x|\log[-\partial^\mu\partial_\mu - V''(\phi_{cl}) + i\epsilon]|x\rangle. \tag{2.33}$$

It is the sum of the classical action, $\mathcal{L}$, and its first-order quantum correction, $\mathcal{L}^{(1)}$.

The semiclassical approximation to the effective action, as written, is infinite and needs to be renormalized. This turns out to be easy since the semiclassical approximation is simply the sum of all one-particle irreducible one-loop diagrams (recall that the effective action is the sum of all one particle irreducible diagrams). To see this, we expand $\mathcal{L}^{(1)}$ about the vacuum. Assume that the vacuum corresponds to the translationally invariant field $\phi_{cl} = \phi_v$ and we want to evaluate $\mathcal{L}^{(1)}$ for $\phi_{cl} = \phi_v + \eta(x)$, then

$$\mathcal{L}^{(1)} = \frac{i}{2}\langle x|\,\log\,[\,-\partial^\mu\partial_\mu - V''(\phi_v)] + \log\,[1 + \frac{-V''(\phi_v+\eta(x)) + V''(\phi_v)}{-\partial^\mu\partial_\mu - V''(\phi_v) + i\epsilon}]\,|x\rangle. \tag{2.34}$$

The first term is the one-loop effective action evaluated in the vacuum, $\mathcal{L}_0^{(1)}$, and the second term corresponds to a sum of one-loop diagrams where vertices are given by

$$\begin{aligned}\lambda(\eta) &= -V''(\phi_v + \eta(x)) + V'' \\ &= \sum_{j=1}^{\infty} \frac{1}{j!} V^{(j+2)}(\phi_v)\eta(x)^j\end{aligned} \tag{2.35}$$

that equals the sum of the vertex strength of the nth order vertices ($n > 2$), where $n-2$ of the external vertices are attached to the external field $\eta(x)$, and $\Delta_0^{-1} = -\partial^\mu\partial_\mu - V''(\phi_v)$ corresponds to the propagator. Taylor expanding the logarithm implies

$$\mathcal{L}^{(1)} - \mathcal{L}_0^{(1)} = \frac{i}{2}\langle x| \sum_{n=1}^{\infty} \frac{(-1)^{(n-1)}}{n} [\Delta_0\lambda(\eta)]^n |x\rangle, \tag{2.36}$$

that is -i times the sum of one-loop diagrams, the nth terms being one-boson-loop diagrams with n different λ vertices as shown in figure 2.1. For instance, the first term in the expansion is

$$\frac{i}{2}\langle x|\Delta_0\lambda(\eta)|x\rangle = -i\frac{1}{2}\int \frac{d^{(n+1)}p}{(2\pi)^{(n+1)}}[i\Delta_0(p)][i\lambda(x)]$$

that is equal to $-i$ times the sum of the diagrams in the first row of figure 2.1.

One-loop diagrams with n or less external legs are divergent. These divergences correspond to divergences in the coupling constants of the theory. These divergences are cured by adding to the Lagrangian terms $\mathcal{L}_{ct}(\eta)$ whose tree level contributions cancel the infinite parts of the corresponding one-loop graph and fix the finite part to give the physically desired coupling constants. These one-loop counterterms are discussed in detail in Appendix A. Since these counter terms make the one-loop graphs

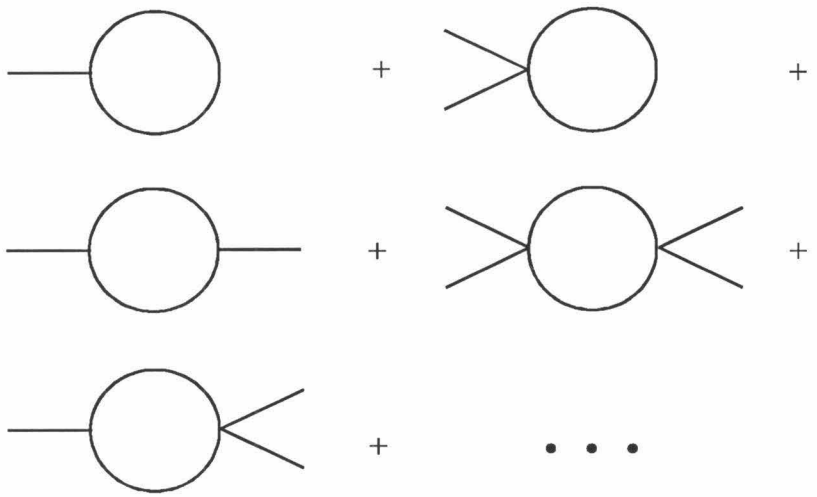

Figure 2.1 – Diagrams contributing to the one-boson-loop approximation to the effective action of a scalar boson theory with cubic and quartic interactions. Each vertex corresponds to a location in space and each external leg receives a value of η at that point in space. The effective action is determined by integrating these diagrams over all space-time points.

finite, they also suffice to make the effective action finite. Adding the counter terms into the effective action

$$S_{\text{eff}}(\phi_{cl}) = \int d^{(n+1)}x\, \mathcal{L}(\phi_{cl}) + \mathcal{L}^{(1)}(\phi_{cl}) + \mathcal{L}_{ct}(\phi_{cl}) \qquad (2.37).$$

makes the difference $S_{\text{eff}}(\phi_{cl}) - S_{\text{eff}}(\bar{\phi})$ finite. The individual effective actions are still divergent because of the zero-point energy of the infinite number of modes of oscillation of the scalar field in the vacuum. This infinite energy cancels any time the difference between any two effective actions is taken.

A simple physical description of the first quantum correction can be obtained by explicitly evaluating its contribution to the energy of the system [3] . From Eq. (2.19), the energy is $-Tr\,\mathcal{L}/\int dt$, where Tr denotes an integral over space-time. The space-time integral of the Lagrangian is conveniently evaluated by first performing the integral over time,

$$Tr\,\mathcal{L}^{(1)} = \frac{i}{2}\mathrm{Tr}' \int dt\, \langle t|\log[-\partial^\mu\partial_\mu - V''(\phi_{cl}) + i\epsilon]|t\rangle, \tag{2.38}$$

where Tr$'$ denotes trace over spatial degrees of freedom. For time-independent ϕ_{cl}, the operator is diagonal in the frequency basis $|\omega\rangle$ where $\langle t|\omega\rangle = \exp(i\omega t)$, implying

$$Tr\,\mathcal{L}^{(1)} = \frac{i}{2}\mathrm{Tr}' \int dt \int \frac{d\omega}{2\pi} \log[\omega^2 + \nabla^2 - V''(\phi_{cl}) + i\epsilon]. \tag{2.39}$$

Integrating by parts yields

$$Tr\mathcal{L}^{(1)} = \frac{i}{2}\int dt\,\mathrm{Tr}' \int \frac{d\omega}{2\pi} \frac{-2\omega^2}{-\omega^2 - \nabla^2 + V''(\phi_{cl}) - i\epsilon}, \tag{2.40}$$

where a constant from the boundary terms has been thrown away (since we are interested only in the difference in the action between different solutions). The spatial trace is conveniently performed in terms of the eigenfunctions of the operator in the denominator of Eq. 2.40,

$$[-\nabla^2 + V''(\phi_{cl})]\eta_n = \omega_n^2\eta_n, \tag{2.41}$$

resulting in

$$\mathrm{Tr}\,\mathcal{L}^{(1)} = \frac{i}{2}\int dt \int \frac{d\omega}{2\pi} \sum_n \frac{-2\omega^2}{-\omega^2 + \omega_n^2 - i\epsilon}. \tag{2.42}$$

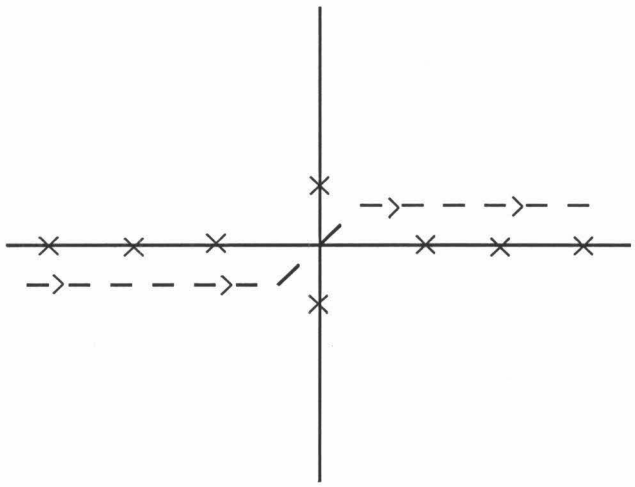

Figure 2.2 – Integration contour in the energy plane for boson-loop energy. The poles are symmetric about zero and can in general lie on the imaginary axis. The integration contour can be closed at infinity, in which case the poles on the imaginary axis give an imaginary contribution to the boson-loop energy.

The operator (2.41) is hermitian, so the eigenvalues ω_n^2 are real, implying that the ω_n are either real or imaginary. The frequency integral in (2.42) thus can, in general, have poles along the real and imaginary axis, as shown in Fig. 2.2.

The integration contour runs under the negative real axis and over the positive real axis. At infinity, the integrand is a constant independent of ϕ_{cl} so closing the contour at infinity contributes an infinite constant that vanishes when the difference between two solutions is computed. Letting ω_n denote the root of the eigenvalue that occurs on the positive real axis or negative imaginary axis, the integral in (2.42)

becomes

$$Tr\,\mathcal{L}^{(1)} = \int dt \frac{i}{2\pi}(2\pi i)\sum_n \frac{2\omega_n^2}{2\omega_n} = -\frac{1}{2}\int dt \sum_n \omega_n. \tag{2.43}$$

This energy corresponds to a sum over the zero-point modes of oscillation of the scalar quantum field in the presence of the background scalar field ϕ_{cl}. Hence, the semiclassical approximation is equivalent to assuming that the modes of the scalar field are non-interacting except through the mean field ϕ_{cl}. Higher-order quantum corrections would build in the interactions betweens these modes of oscillation.

The energy of the system is calculated from the renormalized effective action given in Eq. (2.37) via eq. (2.19), implying

$$E = E_{\text{classical}} + \frac{1}{2}\sum_n \omega_n + E_{\text{bl}}^{\text{ct}},$$

where $E_{\text{classical}}$ is the energy of the classical field configuration,

$$E_{\text{classical}} = -\int d^n x \mathcal{L}(\phi_{cl}), \tag{2.44}$$

and $E_{\text{bl}}^{\text{ct}}$ is the contribution of the one-loop boson counterterms,

$$E_{bl}^{ct} = -\int d^n x \mathcal{L}_{ct}(\phi_{cl}). \tag{2.45}$$

If some of the ω_n are imaginary, then E will be complex, indicating that the one-loop approximation has broken down. This occurs when some modes of the meson field are found to be damped instead of oscillatory, so that the separation of the problem into an average field with small quantum fluctuations about it is no longer sensible. More about the breakdown of the one-loop approximation will be discussed in Chapter 3.

The above energy is still infinite because of the infinite energy stored in the vacuum. The relevant physical energy is the difference between the energy of this state and the vacuum. The scalar field in the vacuum has frequencies ω_n^0 given by

$$[-\nabla^2 + V''(\bar{\phi})]\eta_n = \omega_n^{0\,2}\eta_n, \tag{2.46}$$

implying that the boson-loop energy is

$$E_{bl} = \frac{1}{2}\sum_n \left(\omega_n - \omega_n^0\right) + E_{bl}^{ct}. \tag{2.47}$$

This term gives the first-order quantum correction to the classical solution. Observe that this formalism works for both spatially dependent and independent classical solutions, and therefore can be used to describe excitations in the theory which correspond to extended objects.

Now consider the Lagrangian with fermions added in (2.21) that yields the generating functional

$$Z[J] = \int \mathcal{D}\phi\mathcal{D}\bar{\psi}\mathcal{D}\psi \exp[i\int d^{(n+1)}x\, \mathcal{L}(\phi) + \bar{\psi}(i\gamma^\mu\partial_\mu - g\phi + i\epsilon)\psi + J(x)\phi(x)]. \tag{2.48}$$

The path integral over fermions is Gaussian and can be evaluated exactly since $\int \mathcal{D}\bar{\psi}\mathcal{D}\psi\, \exp[i\bar{\psi}A\psi] = \det(A) = \exp[\mathrm{tr}\, \log A]$, resulting in

$$Z[J] = \int \mathcal{D}\phi\, \exp\left[i\int d^{(n+1)}x\, (\mathcal{L}(\phi) + J(x)\phi(x)) - i\mathrm{Tr}\log(i\gamma^\mu\partial_\mu - g\phi + i\epsilon)\right] \tag{2.49}$$

where Tr is a trace over space-time and spinor indices. This effective boson Lagrangian can now be treated in the same manner as the pure boson theory with Lagrangian

$$\mathcal{L}_{\text{eff}} = \mathcal{L}(\phi) - i\mathrm{tr}\langle x|\log(i\gamma^\mu\partial_\mu - g\phi + i\epsilon)|x\rangle, \tag{2.50}$$

where tr is the remaining trace over spinor indices. Because of the presence of the fermion logarithm in the effective Lagrangian, the classical solution of this Lagrangian incorporates quantum effects that are due to the fermions. As in the boson case, $\tilde{\phi}$ corresponds to the classical extremum of the Lagrangian plus the source term,

$$\frac{\delta \mathcal{L}_{\text{eff}}(\phi) + J(x)\phi(x)}{\delta \phi(x)}\Big|_{\phi=\tilde{\phi}} = 0. \tag{2.51}$$

Ignoring all fluctuations about this classical solution gives the approximation

$$\Omega[J] = \int d^{(n+1)}x\, \mathcal{L}(\tilde{\phi}) - i\text{Tr}\log(i\gamma^\mu \partial_\mu - g\tilde{\phi} + i\epsilon) + J(x)\tilde{\phi}(x) \tag{2.52}$$

that implies $\phi_{cl} = \tilde{\phi}$ and generates the effective action

$$S_{\text{eff}} = \int d^{(n+1)}x\, \mathcal{L}(\phi_{cl}) - i\text{Tr}\log(i\gamma^\mu \partial_\mu - g\tilde{\phi}_{cl} + i\epsilon). \tag{2.53}$$

By expanding the fermion logarithm in the same manner as the boson logarithm, it is seen to be equivalent to the sum of fermion one-loop diagrams with external legs corresponding to ϕ_{cl}. Hence, this approximation is known as the fermion one-loop approximation. The effective action is renormalized by adding the appropriate one-loop fermion counterterms, $\mathcal{L}^{ct}_{fl}$, to the Lagrangian, as shown in Appendix A. The energy contribution that is due to the fermion logarithm is

$$E_{fl} = \frac{i}{\int dt}\text{Tr}' \int dt \langle t|\log(i\gamma^\mu \partial_\mu - g\phi + i\epsilon)|t\rangle \tag{2.54}$$

that becomes, after evaluating the logarithm matrix element in frequency space and integrating by parts,

$$E_{fl} = -i\int \frac{d\omega}{2\pi}\text{Tr}' \frac{-\gamma^0\omega}{-\gamma^0\omega + i\gamma^i\partial_i - g\phi_{cl} - i\epsilon}. \tag{2.55}$$

Evaluating the trace in terms of the eigenstates of

$$[i\gamma^j \partial_j + g\phi_{cl}]\psi_i(x) = \gamma^0 \omega_i \psi_i(x) \tag{2.56}$$

gives

$$E = -\frac{i}{2\pi} \int d\omega \sum_n \frac{\omega}{\omega - \omega_n + i\epsilon} = \sum_{\omega_n < 0} \omega_n, \tag{2.57}$$

where the integration contour is given in Fig. 2.3. The fermion vacuum can be thought of as being an infinite system of fermions in which all of the negative energy states of the Dirac operator (2.56) are occupied. The one-loop energy is the sum over the energy of these occupied states.

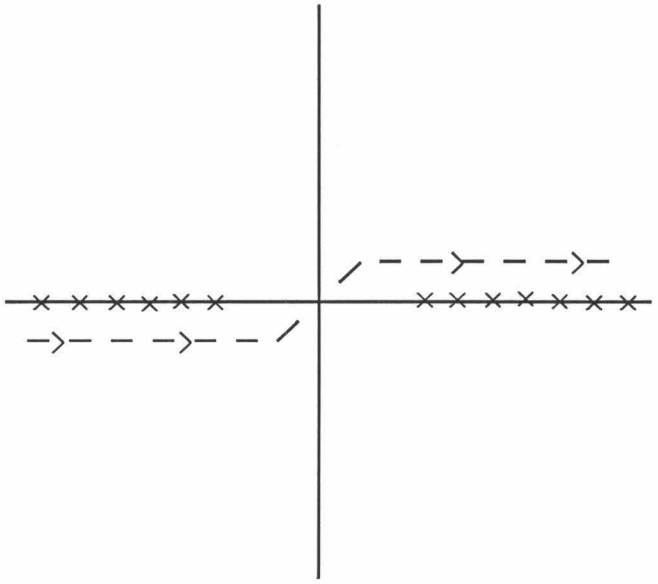

Figure 2.3 – Integration contour in the energy plane for the fermion-loop energy at zero chemical potential. All poles occur along the real axis.

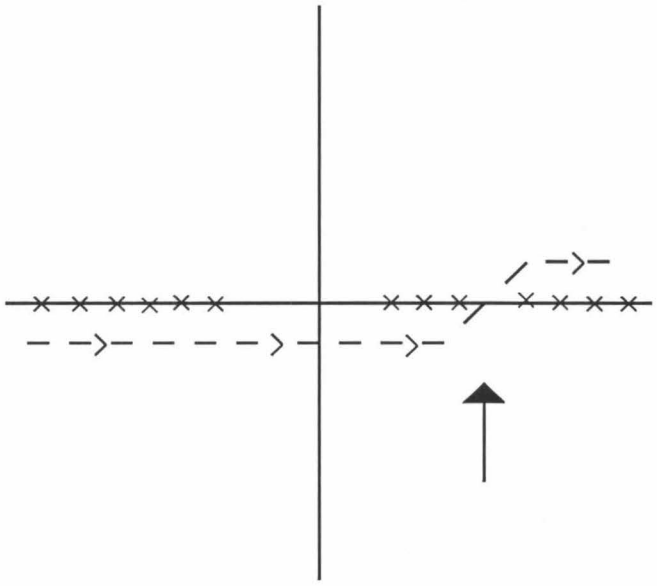

Figure 2.4 – Integration contour in the energy plane for the fermion-loop energy at finite chemical potential. The arrow denotes the value of the chemical potential

The energy relative to the vacuum, which with the inclusion of the one-loop counterterms is finite, is

$$E_{\rm fl} = \sum_{\omega_i<0} \omega_i - \omega_i^0 + E_{fl}^{ct}(\phi_{\rm cl}), \tag{2.58}$$

where

$$[i\gamma^j \partial_j + g\bar{\phi}]\psi_i^0(x) = \gamma^0 \omega_i^0 \psi_i^0(x). \tag{2.59}$$

Frequently, we will be interested in systems with finite baryon density. At the one-loop level this corresponds to occupying some of the positive energy eigenstates of (2.56), which is equivalent to deforming the integration contour also to circle these positive energy states, as shown in Fig. 2.4.

This result follows from using the generating functional $Z(J,\mu_f)$ as given in Equation 2.23. The one-loop effective action is

$$S_{\rm eff}(\phi_{cl},\mu_f) = -iTr\log\left[i\gamma_\mu\partial^\mu - g\phi_{cl} + \mu_f\gamma^0 - i\epsilon\right]. \tag{2.60}$$

This action generates the one-loop free energy $F = E - \mu_f N$, where $F_{fl} = -S_{\rm eff}\int dt$. Our previous results imply that

$$F_{fl} = -i\int\frac{d\omega}{2\pi}{\rm Tr}\frac{-\gamma^0\omega}{-\gamma^0(\omega+\mu_f)+i\gamma^i\partial_i+g\phi_{cl}-i\epsilon}. \tag{2.61}$$

Using the basis states of Eq. 2.56, the trace becomes

$$F_{fl} = -\frac{i}{2\pi}\int d\omega\sum_n\frac{\omega}{\omega+\mu_f-\omega_n+i\epsilon} = \sum_{\omega_n-\mu_f<0}(\omega_n-\mu_f). \tag{2.62}$$

The effect of the chemical potential is to shift the poles in the propagator by μ_f but to leave the integration contour unchanged from that of Fig. 2.2. From the free energy, the one-loop energy is calculated to be

$$\begin{aligned} E_{fl} =& F_{fl} + \mu_f\langle 0|N|0\rangle \\ =& \sum_{\omega_n-\mu_f<0}(\omega_n-\mu_f) + \sum_{\omega_n-\mu_f<0}\mu_f \\ =& \sum_{\omega_n<\mu_f}\omega_n. \end{aligned} \tag{2.63}$$

This result is equivalent to performing the energy integral in Equation 2.57, using the contour shown in Figure 2.4.

The one-fermion-loop approximation is equivalent to the independent particle approximation. The fermion wavefunction is assumed to be decomposable into a product of single-particle wavefunctions all of which see the same potential in which all

the negative energy states and the positive energy states with energy below the fermi energy are occupied. All correlations, including exchange correlations, are ignored. Hence, this approximation is known as the relativistic Hartree approximation (RHA).

The fermion-loop energy is conveniently separated into two parts

$$E_{fl} = E_{\text{valence}} + E_{\text{vacuum}}, \tag{2.64}$$

where

$$E_{\text{valence}} = \sum_{0<\omega_n<\mu_f} \omega_n \tag{2.65}$$

is the energy of the valence fermions and

$$E_{\text{vacuum}} = \sum_{\omega_n<0} (\omega_n - \omega_n^0) + E_{\text{ct}}^{\text{fl}}(\phi) \tag{2.66}$$

is the energy that is due to the perturbation of the vacuum by ϕ. The total energy in the RHA approximation is

$$E_{\text{RHA}} = E_{\text{valence}} + E_{\text{vacuum}} + E_{\text{meson}}, \tag{2.67}$$

where E_{meson} is the classical energy of the scalar field

$$E_{\text{meson}} = \int d^3x \, \frac{1}{2}(\nabla\phi)^2 + V(\phi). \tag{2.68}$$

The scalar field corresponding to the ground state of the system is determined by minimizing this energy ($\delta E_{\text{RHA}}/\delta\phi = 0$), yielding the equation of motion

$$\nabla^2\phi - V'(\phi) = \frac{\delta E_{fl}}{\delta\phi(x)}. \tag{2.69}$$

Since the Dirac Equation (2.56) implies

$$\omega_n = \int d^n x \, \psi^\dagger(x)\gamma^0[i\gamma^j\partial_j + g\phi_{cl}]\psi_i(x), \tag{2.70}$$

it follows that

$$\frac{\delta E_{fl}}{\delta\phi(x)} = g_s \sum_{0<\omega_n<\mu_f} \bar{\psi}_n\psi_n + g_s \sum_{\omega_n<0} (\bar{\psi}_n\psi_n + \frac{\delta E_{ct}(\phi)}{\delta\phi(x)}). \tag{2.71}$$

This is equal to the sum of the scalar density of the valence particles,

$$\rho_s^{\text{valence}} = \sum_{0<\omega_n<\mu_f} \bar{\psi}_n\psi_n, \tag{2.72}$$

and the scalar density induced in the Dirac sea by ϕ,

$$\rho_s^{\text{vacuum}} = \sum_{\omega_n<0} \bar{\psi}_n\psi_n + \frac{1}{g_s}\frac{\delta E_{ct}(\phi)}{\delta\phi(x)}. \tag{2.73}$$

The scalar densities act as a source of the scalar meson field,

$$\nabla^2\phi - V'(\phi) = g_s(\rho_s^{\text{valence}} + \rho_s^{\text{vacuum}}) = g_s\rho_s. \tag{2.74}$$

This is the equation that must be solved in order to perform a relativistic Hartree calculation.

2.3 Uniform Systems

One-loop corrections are straightforward to evaluate in uniform systems where they correspond to the effective potentials. Such calculations were first performed by Coleman and Weinberg [12]. In this section, we evaluate these corrections in a manner that is consistent with our approach to finite systems and discuss the nature of the one-loop corrections to uniform systems. These calculations also demonstrate the renormalization procedure in our computational approach.

First consider self-interacting scalar bosons in 1+1 dimensions as described by the Lagrangian

$$\mathcal{L}(\phi) = \frac{1}{2}\partial^\mu\phi\partial_\mu\phi - V(\phi). \tag{2.75}$$

Static, uniform systems correspond to a value of ϕ_{cl} that is independent of space and time with a corresponding energy density

$$\epsilon = \frac{E}{\int d^3x} = V_{\text{eff}}(\phi_{cl}). \tag{2.76}$$

Classically, the energy density of this system is $V(\phi)$ for time and spatially independent fields ϕ. The vacuum of the system corresponds to the value of the field $\phi = \phi_v$ that minimizes the energy, implying that $V'(\phi_v) = 0$ and $V''(\phi_v) > 0$. According to Eq. (2.47), the one-loop correction to the energy density is $\epsilon_{bl}(\phi_c) = \frac{1}{2}\sum_i(\omega_i - \omega_i^0) - \mathcal{L}_{\text{ct}}(\phi)$, where the ω_i are the eigenvalues of $-\nabla^2 + V''(\phi_c)$ and hence take on the values $\omega_i = \sqrt{k_i^2 + V''(\phi_{cl})}$. Therefore, the one-boson-loop correction is

$$\epsilon_{bl}(\phi_c) = \lim_{\Lambda\to\infty}\frac{1}{2}\int_{-\Lambda}^{\Lambda}\frac{dk}{2\pi}\left(\sqrt{k^2 + V''(\phi_c)} - \sqrt{k^2 + V''(\phi_v)}\right) - \mathcal{L}_{\text{ct}}(\phi, \Lambda). \tag{2.77}$$

Evaluating the integral gives

$$\lim_{\Lambda\to\infty}\frac{1}{4\pi}\Big[\Lambda\sqrt{\Lambda^2+V''(\phi_c)}-\Lambda\sqrt{\Lambda^2+V''(\phi_v)}$$
$$V''(\phi_c)\log\big(\frac{\Lambda+\sqrt{\Lambda^2+V''(\phi_c)}}{\sqrt{V''(\phi_{cl})}}\big)-V''(\phi_v)\log\big(\frac{\Lambda+\sqrt{\Lambda^2+V''(\phi_v)}}{\sqrt{V''(\phi_v)}}\big)\Big]$$

$$=\frac{1}{8\pi}\Big[\lim_{\Lambda\to\infty}V''(\phi_c)-V''(\phi_v)$$
$$V''(\phi_c)\log\big(\frac{4\Lambda^2}{V''(\phi_c)}\big)-V''(\phi_v)\log\big(\frac{4\Lambda^2}{V''(\phi_v)}\big)\Big] \tag{2.78}$$

$$=\frac{1}{8\pi}\lim_{\Lambda\to\infty}\Big[V''(\phi_c)-V''(\phi_v)$$
$$-V''(\phi_c)\log\big(\frac{V''(\phi_c)}{V''(\phi_v)}\big)+(V''(\phi_c)-V''(\phi_v))\log\big(\frac{4\Lambda^2}{V''(\phi_v)}\big)\Big].$$

It follows that the counterterm must be

$$-\mathcal{L}_{\rm ct}(\phi,\Lambda)=-\frac{1}{8\pi}(V''(\phi_c)-V''(\phi_v))\log\big(\frac{4\Lambda^2}{V''(\phi_v)}\big)+\text{finite terms.} \tag{2.79}$$

The finite terms are picked so that certain values of the parameters in the classical Lagrangian have the same meaning in the full quantum energy. For instance, demanding that

$$\frac{\partial E}{\partial\phi}\Big|_{\phi=\phi_v}=0 \tag{2.80}$$

is satisfied requires no additional finite piece to be added to the counterterm. Note that this expression can also be obtained by explicitly renormalizing the divergent one-loop Feynman graphs at zero external momentum and calculating the contribution of these counterterms to the energy, as shown in Appendix A. Additional finite counterterms can be added if one also wants to obtain a specific relation between higher derivatives of the energy and the parameters of the Lagrangian.

Thus, our final expression for the one-boson-loop energy is

$$\epsilon_{bl}(\phi_c) = \frac{1}{8\pi}\Big[V''(\phi_c) - V''(\phi_v) - V''(\phi_c)\log\big(\frac{V''(\phi_c)}{V''(\phi_v)}\big)\Big], \tag{2.81}$$

implying that our expression for the total energy is $V_{\text{eff}}(\phi_{cl}) = V(\phi_{cl}) + E_{bl}(\phi_{cl})$.

In order to understand the effect of the boson-loop energy on the energy functional, we consider a specific example of a boson field with a quartic self-interaction described by

$$V(\phi) = \frac{1}{2}m^2\phi^2 + \frac{1}{4}\lambda\phi^4 \tag{2.82}$$

that has $\phi_v = 0$ and $V''(\phi_v) = m^2$. The corresponding one-loop effective potential is

$$V_{\text{eff}}(\phi_c) = V(\phi) + \frac{1}{8\pi}\Big(3\lambda\phi^2 - (3\lambda\phi^2 + m^2)\log\big[\frac{3\lambda\phi^2 + m^2}{m^2}\big]\Big). \tag{2.83}$$

These potentials are plotted in Fig. 2.5.

The boson-loop contribution is negative and decreases monotonically with increasing field strength. The rate at which it decreases ($\sim \phi^2\log\phi$) is slower than the classical energy increase ($\sim \phi^4$), so that the total energy of the system always increases with increasing field strenth. Hence, the general structure of the effective potential is unchanged by including the first quantum correction. Also note that since the classical energy depends on a higher power of ϕ than the quantum correction, the quantum correction becomes negligible for large values of ϕ, as shown in Figure 2.6.

The above statements apply to any potential for which $V''(\phi_{cl})$ is positive and grows more slowly than $V(\phi_{cl})$. The one-loop approximation breaks down if $V''(\phi_{cl})$ is less than zero. This occurs because the low momentum, single-particle modes correspond to an imaginary energy as disussed in the previous section. Such a situation

effective potential must be convex and the loop expansion is not strong enough to change the convexity of the classical potential.

Now consider a system of fermions with mass M interacting through a scalar meson as described by the Lagrangian

$$\mathcal{L} = \frac{1}{2}\partial^\mu\phi\partial_\mu\phi - \frac{1}{2}m^2\phi^2 + \bar{\psi}(i\gamma^\mu\partial_\mu - M + g\phi)\psi. \tag{2.84}$$

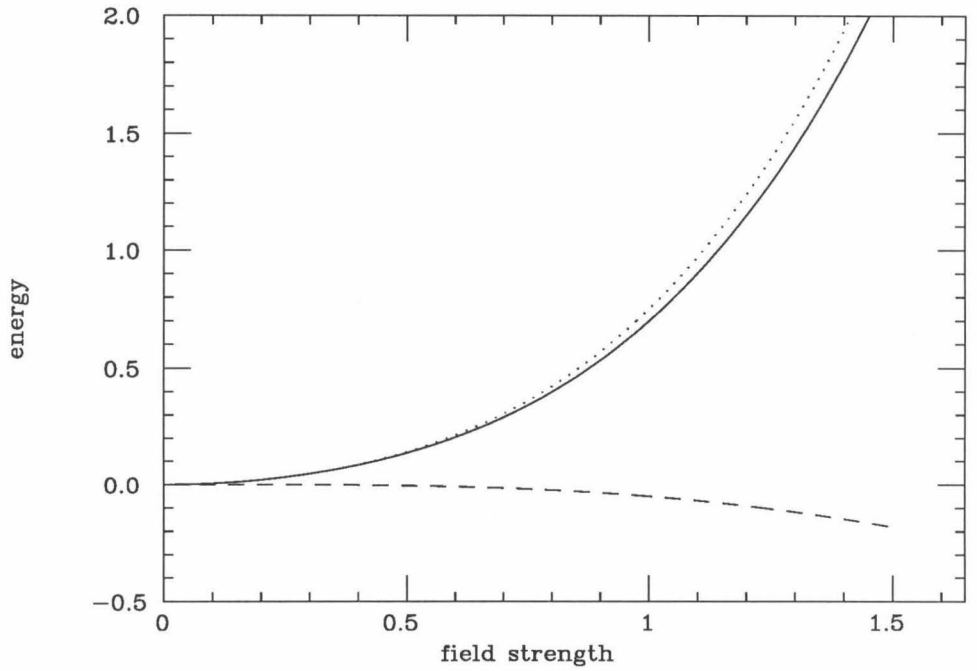

Figure 2.5 – Effective potential for a massive scalar field with a quartic self-interaction in 1+1 dimensions as given by eq. (2.82) with $m = \lambda = 1$ The solid line is the effective potential, the dotted line is the classical potential, and the dashed line is the one-boson-loop energy.

arises in potentials that have more than one minimum, which are the type of potentials that give rise to solitons. This is a reflection of the fact that the full quantum effective potential must be convex and the loop expansion is not strong enough to change the convexity of the classical potential.

Now consider a system of fermions with mass M interacting through a scalar meson as described by the Lagrangian

$$\mathcal{L} = \frac{1}{2}\partial^\mu\phi\partial_\mu\phi - \frac{1}{2}m^2\phi^2 + \bar{\psi}(i\gamma^\mu\partial_\mu - M + g\phi)\psi. \tag{2.84}$$

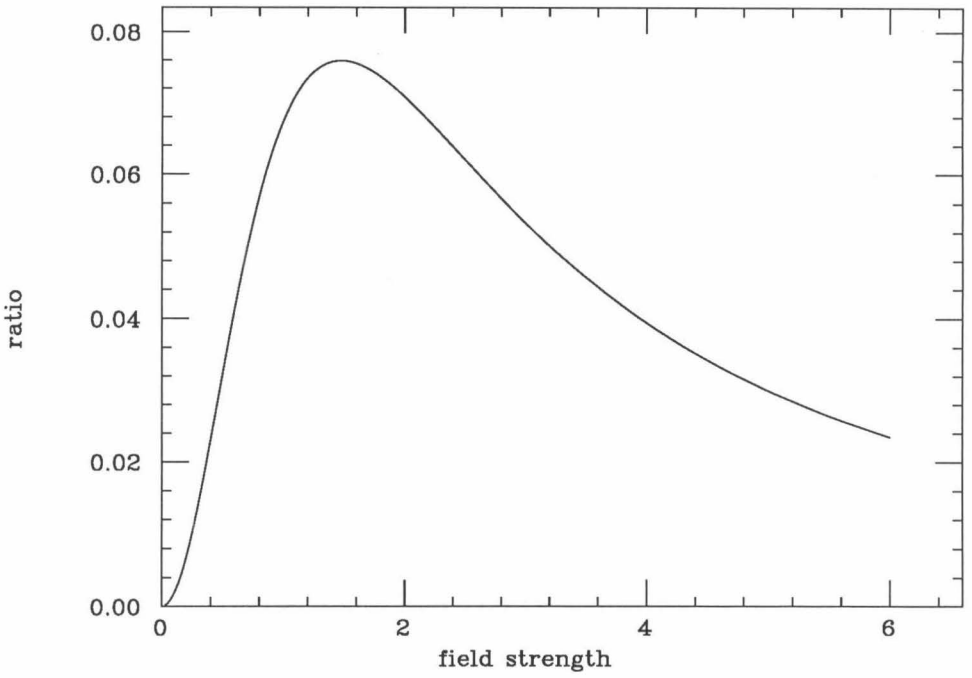

Figure 2.6 – Ratio of the boson-loop energy to the classical energy. At large field strengths the quantum correction becomes negligible compared to the classical energy.

It is convenient to define the effective mass M^* to be

$$M^* = M - g\phi. \tag{2.85}$$

The vacuum expectation value of the scalar field is zero. In a uniform background field of strength ϕ, the energy spectra of the Dirac equation is $\omega_i = \sqrt{k_i^2 + (M^*)^2}$; hence, the one-fermion-loop energy density is

$$\epsilon_{\text{vacuum}} = -\int_{-\Lambda}^{\Lambda} \frac{dk}{2\pi}\left(\sqrt{k^2 + (M^*)^2} - \sqrt{k^2 + M^2}\right) - \mathcal{L}_{ct}(\phi). \tag{2.86}$$

This integral is of the same form as Eq. (2.77), so by picking

$$-\mathcal{L}_{ct} = \frac{1}{4\pi}[(M^*)^2 - M^2]\log\left(\frac{4\Lambda^2}{M^2}\right), \tag{2.87}$$

the one-loop effective potential is found to be

$$V_{eff}(\phi) = \frac{1}{2}m^2\phi^2 - \frac{1}{4\pi}\left[(M^*)^2 - M^2 - (M^*)^2 \log\left(M^*/M\right)^2\right]. \tag{2.88}$$

This potential is shown in Figure 2.7.

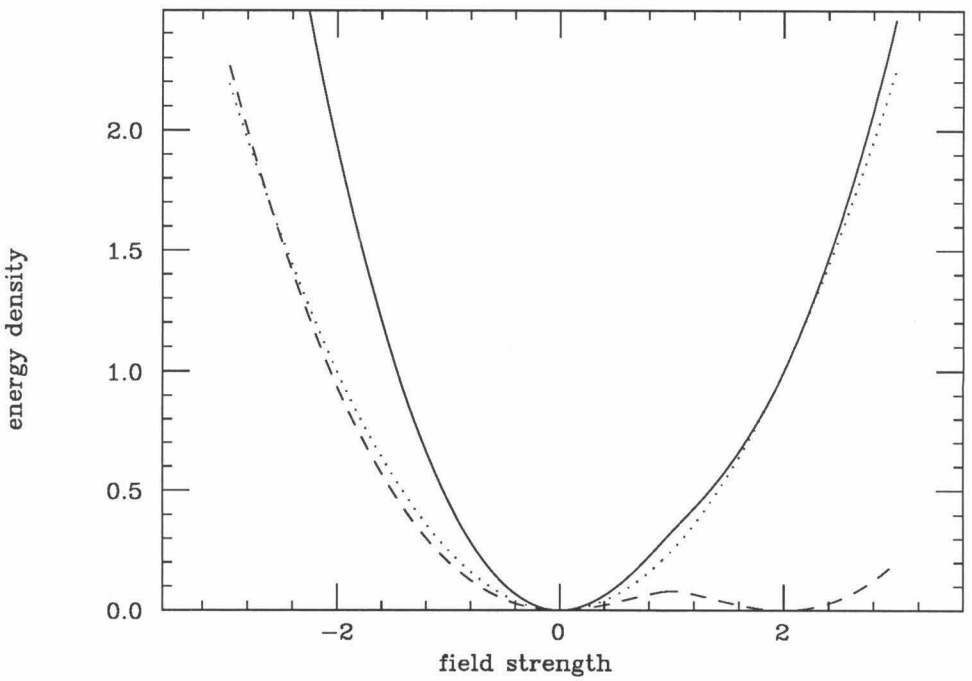

Figure 2.7 – One-fermion-loop effective potential in 1+1 dimensions. The solid line is the total effective potential, the dashed line is the fermion-loop contribution, and the dotted line is the classical contribution for the Lagrangian (2.84) with $m = M = g = 1$.

The contribution of the Dirac sea is positive and symmetric about $\phi = M$, so that the one-loop effective potential no longer has the symmetry of the classical potential, although the minimum of the potential remains at $\phi = 0$. Observe that the energy of the Dirac sea grows faster than the classical potential with increasing

field strength, so that the effective potential at large field strengths is dominated by the Dirac sea.

Now consider the effective potential at finite density, which is generated by adding in the energy of the occupied valence orbitals, $\epsilon_{\text{valence}}$,

$$\begin{aligned}\epsilon_{\text{valence}} &= \int_{-k_f}^{k_f} \frac{dk}{2\pi}\sqrt{k^2+(M^*)^2} \\ &= \frac{1}{2\pi}\Big[k_f\sqrt{k_f^2+(M^*)^2} + (M^*)^2 \log\Big(\frac{k_f+\sqrt{k_f^2+(M^*)^2}}{(M^*)^2}\Big)\Big].\end{aligned} \tag{2.89}$$

The shape of the effective potential is shown in Fig 2.8. The minimum of $\epsilon_{\text{valence}}$ occurs at $g\phi = M(M^* = 0)$, moving the minimum of the effective potential towards positive ϕ. Observe that for large values of the field (or equivalently, the effective mass M^*) at fixed fermi momentum, the classical energy scales like M^{*2}, the valence energy like M^*, and the vacuum energy like $M^{*2}\log M^*$, meaning that in large external fields the vacuum will be the dominant contribution to the energy.

If there is no external field, then the system sits at the minimum of the effective potential. The value of the scalar field at the minimum is generated by the scalar density of the valence particles (ρ_s^{valence}) and the induced scalar density in the vacuum (ρ_s^{vacuum}). Specifically, the value of the mimumum is determined by $\frac{\partial V_{\text{eff}}(\phi)}{\partial\phi} = 0$, implying

$$-m_s^2\phi^2 = -g_s[\rho_s^{\text{valence}} + \rho_s^{\text{vacuum}}], \tag{2.90}$$

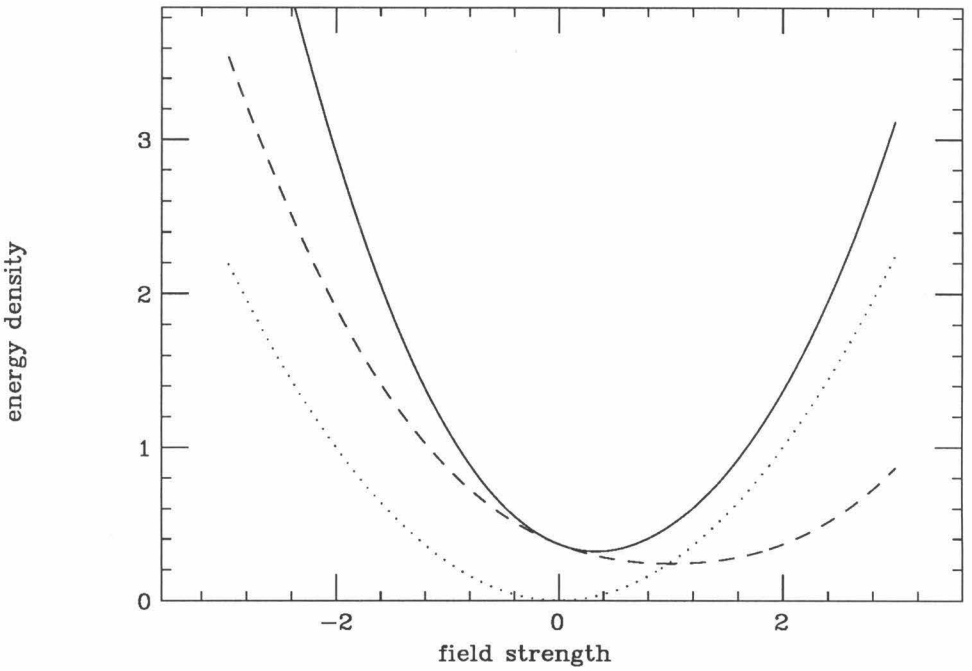

Figure 2.8 – One-fermion-loop effective potential in 1+1 dimensions at finite density for the Lagrangian (2.84) with $m = M = g = 1$ and $k_f = 1$. The solid line is the total effective potential, the dashed line is the fermion-loop contribution, and the dotted line is the classical contribution. The minimum of the effective potential is now greater than zero.

where

$$\rho_s^{\text{valence}} = \frac{\partial \epsilon_{\text{valence}}}{\partial M^*}$$

$$= \frac{k_f M^*}{\sqrt{k_f^2 + M^{*2}}} + 2M^* \log\left(\frac{k_f + \sqrt{k_f^2 + M^{*2}}}{M^*}\right) \qquad (2.91)$$
$$- M^* + \frac{M^{*3}}{(k_f + \sqrt{k_f^2 + M^{*2}})\sqrt{k_f^2 + M^{*2}}}$$

and

$$\rho_s^{\text{vacuum}} = \frac{1}{2\pi} M^* \log\left(\frac{M^*}{M}\right)^2. \qquad (2.92)$$

The effective mass is determined implicitly by solving (2.90). At large fermi momentum this equation simplifies to

$$\frac{m_s^2}{g_s^2}(M^* - M) + \frac{M^*}{\pi}\log(\frac{2k_f}{M}) = 0, \tag{2.93}$$

which implies that

$$M^* \propto \frac{1}{\log(\frac{k_f}{M})}. \tag{2.94}$$

This logarithmic decrease with fermi momentum at large fermi momentum is shown in Fig. 2.9, where the M^* is plotted vs. k_f for $g_s = m_s = M = 1$.

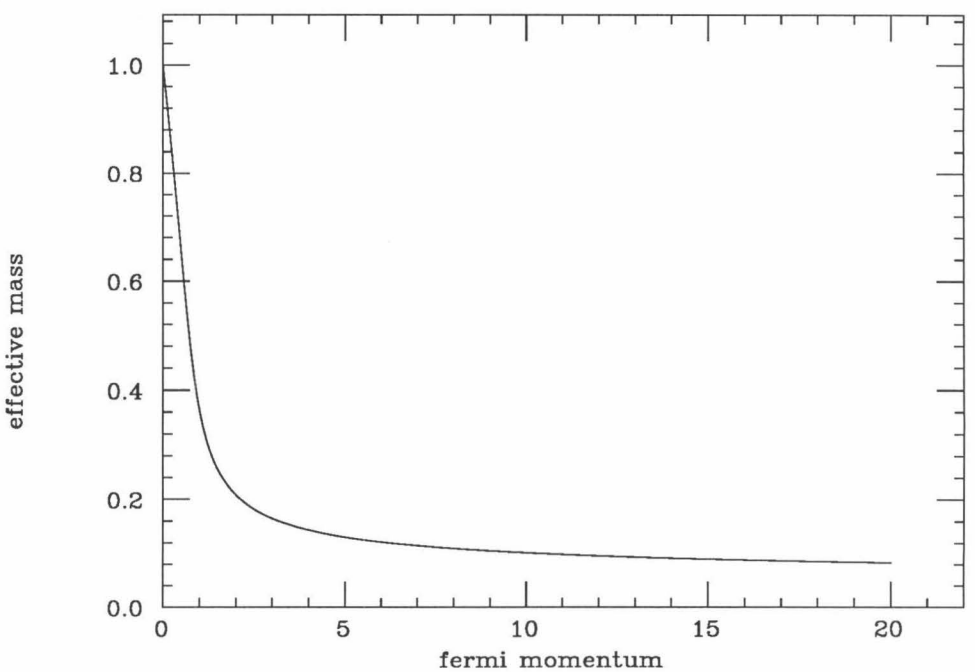

Figure 2.9 – Effective mass as a function of fermi momentum for fermions coupled to a scalar field. The effective mass decreases logarithmically with the fermi momentum.

Because the effective mass decreases so slowly with fermi momentum, the classical energy and the vacuum energy increase logarithmically only with the fermi momentum, while the valence energy increases with the square of the fermi momentum. Hence, at large fermi momentum the valence energy dominates. Even when the valence sector dominates the energy, the vacuum can still play an important role in other quantities. For instance, the ratio of the scalar density that is due to the valence particles to that which is due to the vacuum scales only like $\log(k_f)/\log(\log k_f)$, resulting in a very slow variation in this ratio. Thus, even when the vacuum is contributing negligibly to the total energy, it can still be contributing quite strongly to the scalar density. This effect is shown explicitly in Fig. 2.10 for the case $m_s = g = M = 1$.

The fermion effective potential changes significantly when one goes from one to three spatial dimensions. In three spatial dimensions, the vacuum energy is

$$\epsilon_{\text{vacuum}} = \lim_{\Lambda\to\infty} -2\int_{-\Lambda}^{\Lambda} \frac{dk}{(2\pi)^3} 4\pi k^2 \left(\sqrt{k^2+(M^*)^2} - \sqrt{k^2+M^2}\right) - \mathcal{L}_{ct}(\phi,\Lambda), \quad (2.95)$$

which is evaluated to equal

$$\begin{aligned}\epsilon_{\text{vacuum}} = \lim_{\Lambda\to\infty} -\frac{1}{\pi^2}\Big[&\frac{1}{4}(M^{*2}-M^2)\Lambda^2 + \frac{1}{8}(M^4 - M^{*4})\log\left(\frac{2\Lambda}{M}\right) \\ &\frac{M^{*4}}{8}\log\left(\frac{M^*}{M}\right) - \frac{1}{32}(M^{*4}-M^4)\Big] - \mathcal{L}_{ct}(\phi,\Lambda),\end{aligned} \quad (2.96)$$

implying that

$$-\mathcal{L}_{ct}(\phi,\Lambda) = \frac{1}{\pi^2}\Big[\frac{1}{4}(M^{*2}-M^2)\Lambda^2 + \frac{1}{8}(M^4-M^{*4})\log\left(\frac{2\Lambda}{M}\right)\Big] + \text{finite terms.} \quad (2.97)$$

Since in 3+1 dimensions scalar self-interactions of order 4 and less are renormalizable, we pick the finite parts of the counterterms to cancel the terms of order 4 and less in ϵ_{vacuum}; i.e.,

$$\left.\frac{\partial\epsilon_{\text{vacuum}}}{\partial M^*}\right|_{M^*=M} = \cdots = \left.\frac{\partial^4\epsilon_{\text{vacuum}}}{\partial M^{*4}}\right|_{M^*=M} = 0, \quad (2.98)$$

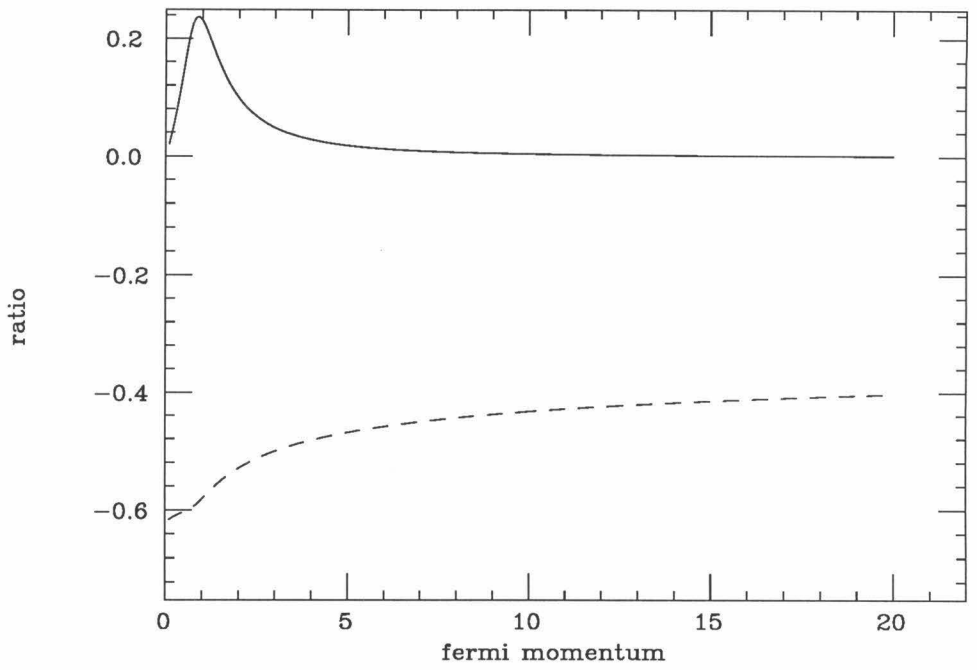

Figure 2.10 – Relative contributions of sea and valence fermions as a function of fermi momentum. The solid line shows the ratio of the vacuum energy to the valence energy. This decreases rapidly with the fermi momentum since the valence energy is proportional to k_f^2, while the vacuum energy is proportional to $\log k_f$. The dashed line shows the ratio of the vacuum-scalar density to the valence-scalar density. This quantity decreases very slowly with increasing k_f.

resulting in the final expression

$$\begin{aligned}\epsilon_{\text{vacuum}} = &-\frac{1}{8\pi^2}\Big[M^{*4}\log\left(\frac{M^*}{M}\right) + M^3(M-M^*) \\ &-\frac{7}{2}M^2(M-M^*)^2 + \frac{13}{3}M(M-M^*)^3 - \frac{25}{12}(M-M^*)^4\Big].\end{aligned} \tag{2.99}$$

For large values of M^* this expression scales like $M^{*4}\log(M^*/M)$, which is negative, while the classical meson potential scales only like M^{*2}, implying that the effective potential diverges to minus infinity as $|M^*| \to \infty$. For $M^* \sim M$ the vacuum energy is positive and concave up so that the minimum at $M^* = M$ is preserved. The effective

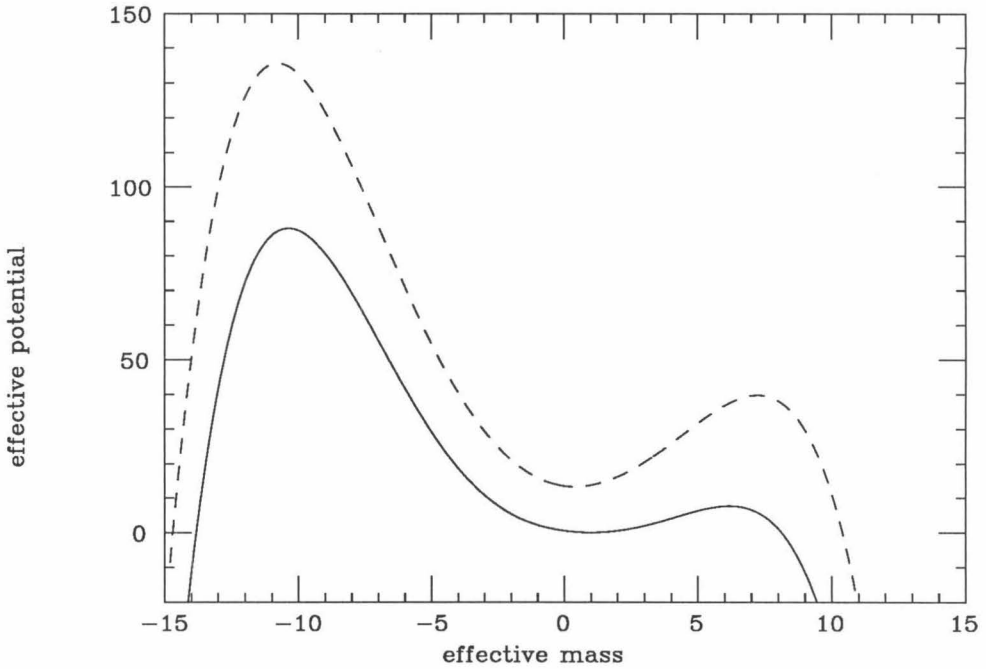

Figure 2.11 – One-fermion-loop effective potential for fermions coupled to a scalar field in 3+1 dimensions. The solid line shows the effective potential for $k_f = 0$ and the dashed line for $k_f = 4$, where $g_s = 1$ and $m_s = M = 1$. The minimum in the classical potential is now only a local minimum in the one-loop effective potential that becomes better defined as the fermi momentum is increased.

potential for $m_s = M = g_s = 1$ is shown in Fig. 2.11. This instability at large field strengths indicates that the one-loop approximation is failing in this regime.

Since the physical minimum in the effective potential remains well-defined, the fact that it is only a local minimum has no effect on the isolated system. At finite

density, the energy of the valence fermions in three spatial dimensions is

$$\begin{aligned}\epsilon_{\text{valence}} &= \int_0^{k_f} \frac{d^3k}{(2\pi)^3}\sqrt{k^2+(M^*)^2} \\ &= \frac{2}{\pi^2}\Big[\frac{k_f}{4}(k_f^2+M^{*2})^{3/2} - \frac{k_f}{8}M^{*2}\sqrt{k_f^2+M^{*2}} \\ &\quad - \frac{1}{8}M^{*2}\log\Big(\frac{k_f+\sqrt{k_f^2+M^{*2}}}{M^*}\Big)\Big].\end{aligned} \tag{2.100}$$

Adding this to the effective potential makes the physical minimum more pronounced, as shown in Fig. 2.11. Hence, physical solutions exist at all densities. As in the one-dimensional case, the effective mass at the minimum decreases very slowly with fermi momentum so that at large densities $\epsilon_{\text{valence}}$ dominates the energy distribution.

Finally, consider self-interacting scalar bosons in 3+1 dimensions. The effective potential is simply obtained from Eq. (2.99) by multiplying by $-1/2$ and by replacing M^{*2} with $V''(\phi)$. In this case the effective potential becomes dominated at large fields by the vacuum energy. Since the boson-loop correction represents the first term in a perturbative expansion of the energy density, when the boson-loop correction is large compared to the classical energy, it will not provide a good representation of the full quantum energy. Hence, unlike the 1+1 dimensional case, the semi-classical approximation breaks down in strong background fields.

In summary, we have examined the one-loop quantum corrections in finite systems. For a self-interacting scalar field in 3+1 dimensions and a fermion field in any number of dimensions, the one-loop vacuum energy pieces become the dominant contribution in large external fields implying that the loop expansion is not convergent in this regime. A result of this is that the one-loop fermion vacuum is unstable with respect to large fields. At finite fermion density, the energy of the isolated system becomes dominated by the valence particles at large fermi momentum and the instability associated with the vacuum energy becomes less important.

2.4 Finite Systems

We now discuss one-loop corrections in finite systems, which is the primary topic of this thesis. As discussed in Section 2.2, in order to evaluate one-loop corrections in finite systems, we need to find the eigenvalues of some spatially varying differential operator

$$\mathcal{O}(x)\Psi_i = \lambda_i \Psi_i \tag{2.101}$$

and then sum up the eigenvalues while subtracting counterterms and vacuum eigenvalues,

$$E_{loop} = \sum_{\omega_i^0 < \Lambda} \omega_i - \omega_i^0 + E_{ct}[\phi(x), \Lambda], \tag{2.102}$$

where $\epsilon_i = \lambda_i < 0$ for fermions and $\epsilon_i = \sqrt{\lambda_i}$ for bosons.

In some special situations, where we can solve for the ω_i analytically, the evaluation of Eq. 2.102 proceeds in the same way as the previous section (see Appendix C). Unfortunately, for a general background field, the energy eigenvalues must be determined numerically, the sum $\sum_{\omega_i^0<\Lambda}(\omega_i - \omega_i^0)$ evaluated explicitly , and then the counterterm subtracted. This has to be done at a large cutoff in order to get the energy correct. At these large cutoffs both the sum and counterterm (both of which diverge as a function of the cutoff) are very large. Hence, to calculate their difference accurately, these terms must be calculated individually to very large precision, resulting in a large computational burden. Nonetheless, such energy calculations can be carried out, either by directly evaluating the sum [13] or by indirectly evaluating it using Green's function techniques [14]. It should be noted, however, that these calculations have the desirable attribute of being readily adaptable to parallel processing computers by having each processor calculate a specific energy interval in the sum of

Equation (2.102). The application of such computers to this problem could make the brute force technique more tractable.

Simply being able to calculate the energy is only the first step; we must then find the value of the scalar field that minimizes it. This requires the ability to calculate the induced densities in the vacuum (ρ_{vacuum}) and then to solve an equation of the form

$$\mathcal{O}[\phi(x)] = \rho_{\text{vacuum}}[\phi(x)]. \tag{2.103}$$

Since ρ_{vacuum} depends on $\phi(x)$ both non-linearly and non-locally, the solution to (2.103) also requires a large numerical effort. Typically, it is solved in some iterative fashion such as

$$\mathcal{O}[\phi^{(n+1)}(x)] = \rho_{\text{vacuum}}[\phi^n(x)], \tag{2.104}$$

where we guess an initial solution, calculate the induced density, invert the operator $\mathcal{O}$ to obtain a new solution, and keep on going until convergence is obtained. For this approach to be computationally feasible, we clearly need a fairly quick way to calculate the density.

This motivates us to consider various local approximations to the effective action. Recall that for uniform systems the effective action is simply given by the effective potential that can be calculated analytically. The induced densities are then simply calculated by taking the derivative of the effective potential. If the background field is slowly varying in a way to be quantified shortly, then it will look locally like a uniform system. This generates the local density approximation (LDA) [15],

$$E_{\text{LDA}} = \int d^n x V_{\text{eff}}[\phi(x)] \tag{2.105}$$

and

$$\rho_{\rm LDA}(x) = \frac{\delta E_{\rm LDA}}{\delta\phi(x)} = \frac{\partial V_{\rm eff}(\phi)}{\partial\phi}(x), \tag{2.106}$$

which allows Eq. (2.103) to be solved efficiently.

The LDA is the first term in a systematic expansion of the effective action in terms of derivatives of the background field [11]. The Lorentz invariant effective action can be expanded as

$$S_{\rm eff} = -\int d^{(n+1)}(x) V_{\rm eff}[\phi(x)] + \frac{1}{2} Z[\phi(x)]\partial_\mu\phi(x)\partial^\mu\phi(x) + \mathcal{O}(\partial^4), \tag{2.107}$$

where each of the coefficients can be calculated analytically in terms of Feynman diagrams in the vacuum. For instance, as mentioned previously, the effective potential is determined by all Feynman diagrams with external legs at zero-external momentum. Correspondingly, Z is determined by diagrams with two external legs corresponding to momenta k and $-k$ and the rest of the legs at zero external momenta, etc. Hence, it is straightforward to derive the coefficients of an expansion of the effective action in powers of derivatives. A technique for doing this, along with the expansions that will be needed in this thesis, is given in Appendix B.

The convergence of these derivative expansions has been studied extensively by Li,Perry, and Wilets [14]. By dimensional analysis, as we add more and more derivatives, we must divide by terms of dimension mass in order to keep the effective action dimensionless. For example, consider the expansion of the fermion one-loop effective action in $1+1$ dimensions where the fermions are coupled to a scalar field. Since the scalar field is dimensionless, the expansion must involve terms that look like $[M^*(x)]^{-2}\partial^\mu\phi(x)\partial_\mu\phi(x)$, meaning that derivative expansion is related to an expansion

in inverse powers of the effective mass of the field. The criteria for convergence are then

$$\frac{1}{M^*(x)}\frac{\partial\phi(x)}{\partial x} << 1\,,\ \frac{1}{M^*(x)^2}\frac{\partial^2\phi(x)}{\partial^2 x} << 1,\ \ldots. \tag{2.108}$$

When the derivative expansion (DE) is convergent, it can be used to generate a reliable local approximation to effective action that leads to the approximation

$$E_{DE} = \int d^n x\, V_{\rm eff}(\phi) + \frac{1}{2}Z(\phi)(\nabla\phi)^2 + \mathcal{O}(\partial^4) \tag{2.109}$$

and

$$\rho_{\rm vacuum}(x) = \frac{\partial V_{\rm eff}(\phi)}{\partial\phi}(x) - \nabla\cdot[Z(\phi)\nabla\phi(x)] + \mathcal{O}(\partial^4). \tag{2.110}$$

This method is used in Chapter five to study bound systems of massive fermions interacting with scalar and vector mesons, where such expansions are found to be convergent.

The advantage of the derivative expansion is that it provides a local approximation to the non-local effective action that allows self-consistent calculations to be pursued efficiently. When the derivative expansion diverges, we will show in the next chapter that the primary problem is due to the existence of strongly bound discrete states. The contribution of the remaining states can still be dealt with effectively via a local approximation, as will be shown in Chapter 3.

As a last issue, we examine the stability of the vacuum with respect to small, spatially varying perturbations as has been studied by several people [16] . We sketch their argument here. Consider fermions of mass m coupled to a scalar field of mass M,

in which case the one-loop energy (we assume that we are studying a static system) in $3+1$ dimensions is

$$E = \int d^3x \frac{1}{2}(|\nabla\phi|^2 + M^2\phi^2) + \frac{i}{\int dt}\mathrm{Tr}\Big[\log(G_0^{-1} - g\phi) - \log(G_0^{-1}) + i\mathcal{L}_{\mathrm{ct}}\Big], \quad (2.111)$$

where we have included the vacuum subtraction and the counterterms and defined the inverse free fermion Greens function

$$G_0^{-1} = i\gamma^\mu\partial_\mu - m. \quad (2.112)$$

We evaluate (2.112) for small fields by expanding the fermion logarithm up to second order in the field,

$$E = \int d^3x \frac{1}{2}(|\nabla\phi|^2 + M^2\phi^2) - \frac{ig^2}{2\int dt}\mathrm{Tr}G_0\phi G_0\phi - \mathrm{C.T.} \quad (2.113)$$

Note that the term linear in ϕ is exactly cancelled by the counterterm, leaving the term quadratic in the field and the counterterms that are quadratic in the field. Since $\phi(p) = \delta(p^0)\phi(\vec{p})$ for a static field, we can easily evaluate the trace as

$$\begin{aligned}\mathrm{Tr}G_0\phi G_0\phi =& \int \frac{d^4k}{(2\pi)^4}\frac{d^4k'}{2\pi)^4} G_0(k)\langle k|\phi|k'\rangle G_0(k')\langle k'\phi|\phi|\phi\rangle \\ =&\delta(0)\int \frac{d^4k}{(2\pi)^4}\frac{d^4p}{(2\pi)^4}\delta(p^0)\phi(\vec{p})G_0(k)G_0(k-p)\phi(-\vec{p}).\end{aligned} \quad (2.114)$$

Inserting this result into the energy and recalling that $\delta(0) = \int dt$, we obtain

$$E = -\frac{1}{2}\int \frac{d^3p}{(2\pi)^3}\,\phi(\vec{p})G_1^{-1}(\tilde{\phi})\phi(\vec{p}), \quad (2.115)$$

where $\tilde{p}$ is the four vector $(0,\vec{p})$ and

$$G_1^{-1}(\tilde{p}) = -\vec{p}^2 - M^2 + g^2\int \frac{d^4k}{(2\pi)^4}\frac{d^3p}{(2\pi)^3}G_0(k)G_0(k-\tilde{p}) + \mathcal{L}_{\mathrm{ct}} \quad (2.116)$$

is the inverse scalar boson Green's function at the one-fermion-loop level. The above Green's function is equal to a standard Feynman integral for a one-loop diagram with two external vertices carrying a space-like four momentum that with our standard zero-momentum renormalization conventions gives

$$G_1^{-1}(\tilde{p}) = -\vec{p}^2 - M^2 + \frac{1}{\pi^2}\Big[\frac{1}{|\vec{p}|}(\frac{1}{4}\vec{p}^2 + m^2)^{3/2}\log\Big(\frac{\sqrt{\frac{1}{4}\vec{p}^2 + m^2)} + \frac{1}{2}|\vec{p}|}{\frac{1}{4}\vec{p}^2 + m^2) - \frac{1}{2}|\vec{p}|}\Big) - \frac{1}{3}\vec{p}^2 - m^2\Big]. \tag{2.117}$$

For small $\vec{p}$,

$$G_1^{-1}(\tilde{p}) \sim -\vec{p}^2 - m^2 < 0, \tag{2.118}$$

implying that the energy is greater than zero and hence that the vacuum is stable with respect to long wavelength fluctuations. On the other hand, for large $\vec{p}$

$$G_1^{-1}(\tilde{p}) \sim \frac{g^2}{8\pi^2}\vec{p}^2\log\Big(\frac{\vec{p}^2}{m^2}\Big) > 0 \tag{2.119}$$

implying that the energy is negative and hence that the vacuum is unstable with respect to short wavelength fluctuations in the one-loop approximation. The larger g, the larger the wavelength at which this instability sets in. Because of this instability, the one-loop approximation cannot be used for systems that have fields that vary too quickly in space.

Chapter 3
The WKB Method in 1+1 Dimensions

In this chapter, we develop a method for the exact calculation of one-loop corrections to finite systems and apply it to 1+1 dimensional theories. The first section introduces the method for the calculation of boson-loop corrections and discusses its relation to the local approximations of the previous chapter. In the second section, the method is applied to concrete calculations and compared to "brute force" methods. Problems associated with self-consistency are discussed. The third section extends the method to the calculation of fermion-loop corrections and the fourth section discusses self-consistent fermion-loop corrections for couplings to scalar fields.

3.1 WKB Method for Boson-Loop Energy

We first consider calculating the boson-loop energy correction to a spatially varying scalar field, $\phi_{cl}(x)$, in a system governed by the Lagrangian

$$\mathcal{L}(\phi) = \frac{1}{2}\partial^\mu\phi\partial_\mu\phi - V(\phi). \tag{3.1}$$

Assume that the vacuum is described by the uniform field ϕ_v and denote

$$M^2(x) = V''(\phi_{cl}(x)) \tag{3.2}$$

and

$$M^2 = V''(\phi_v). \tag{3.3}$$

In order for a spatially varying object to have finite energy, it must have zero-energy density infinitely far away from its center implying that

$$M(\pm\infty) = M. \tag{3.4}$$

As discussed in previous sections, the boson-loop correction is

$$E_{bl}(\phi_{cl}) = \lim_{\Lambda\to\infty}\Big[\frac{1}{2}\sum_{\omega_i^0<\Lambda}(\omega_i - \omega_i^0) + E_{ct}(\phi_{cl},\Lambda_p)\Big], \tag{3.5}$$

where $\Lambda_p = \sqrt{\Lambda^2 - M^2}$ is the three momentum cutoff corresponding to the energy cutoff Λ. The counterterm is given explicity by (see Appendix A and Section 2.3)

$$\begin{aligned} E_{ct}(\phi_{cl},\Lambda_p) &= -\frac{1}{4\pi}\log\Big[\frac{\Lambda_p + \sqrt{\Lambda_p^2 + M^2}}{M}\Big](M^2(x) - M^2) \\ &= -\frac{1}{4\pi}\log\Big[\frac{\Lambda + \sqrt{\Lambda^2 - M^2}}{M}\Big](M^2(x) - M^2). \end{aligned} \tag{3.6}$$

The energy eigenvalues ω_i^0 are determined by

$$[-\nabla^2 + M^2]\eta_n^0(x) = \omega_i^{0\,2}\eta_n^0(x). \tag{3.7}$$

The solutions of this equation are plane waves with energy $\omega^{n\,2} = k_n^2 + M^2$, so that the energy spectrum of the solutions is a continuum stretching from energy M to infinity. The energy eigenvalues ω_n are detemined by

$$[-\nabla^2 + M^2(x)]\eta_n(x) = \omega_n^2\eta_n(x), \tag{3.8}$$

which is equivalent to the usual Schrödinger equation with a potential $M^2(x)$. The spectra of (3.8) will in general consist of a discrete spectrum of localized states with

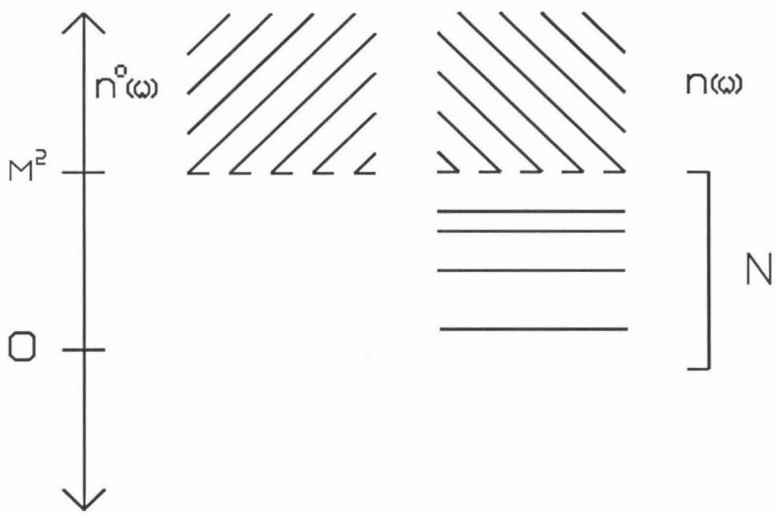

Figure 3.1 – Energy spectrum of scalar boson vacuum modes. The vertical axis is ω^2. The first column is the spectra in the vacuum that consists of a continuum stretching from M^2 to ∞ described by a density of states $n^0(\omega)$. The second column is the spectra in the presence of a background field that consists of N bound states and a continuum stretching from M^2 to ∞ described by a density of states $n(\omega)$.

$\omega_n^2 < M^2$ and a continuum of asymptotic plane-wave states with $\omega_n^2 > M^2$. The energy spectra of both of these equations is shown in Figure 3.1.

The sum over states in the continuum can be replaced by an integral over a density of states,

$$\begin{aligned} \sum \omega_i^0 &= \int_M^\infty \omega n^0(\omega) d\omega \\ \sum \omega_i &= \sum_{\omega_i^2 < M^2} \omega_i + \int_M^\infty \omega n(\omega) d\omega. \end{aligned} \tag{3.9}$$

As pointed out by Dashen, Hasslacher, and Neveu [3] , these sums can be conveniently expressed in terms of the phase shifts of the continuum solutions. In order to derive this dependence, we place the system in a box of length $2L$ and impose periodic boundary conditions

$$\eta(-L) = \eta(L). \tag{3.10}$$

For simplicity, assume that $M^2(x)$ is symmetric so that the solutions can be classified by their parities. The vacuum solutions corresponding to even (e) and odd (o) parity are

$$\begin{aligned} {}^e\eta_n^0(x) &= \cos(k_n^0 x) \\ {}^o\eta_n^0(x) &= \sin(k_n^0 x),\ k_n^0 = \frac{2\pi n}{L}, \end{aligned} \tag{3.11}$$

implying that for large L the density of states per momentum interval is

$$\begin{aligned} n_e^0(k_n) = n_o^0(k_n) &= \frac{1}{k_{n+1} - k_n} \\ &= \frac{2\pi}{L} \end{aligned}. \tag{3.12}$$

This can be converted to a density of states per energy level as

$$\begin{aligned} n_{e,o}^0(\omega_n) = \frac{1}{\omega_{n+1} - \omega_n} &= \frac{dk}{d\omega} n_{e,o}^0(k_n) \\ &= \frac{\omega}{\sqrt{\omega^2 - M^2}} \frac{2\pi}{L}. \end{aligned} \tag{3.13}$$

Since $M^2(x) = M$ at large distances, asymptotically the continuum solutions of Eq. (3.8) that have energy ω_n will look like

$$\begin{aligned} {}^e\eta_n(x \to \infty) &= \cos\left(k_n x + \frac{1}{2}\delta^e(k_n)\right) \\ {}^o\eta_n^0(x \to \infty) &= \sin\left(k_n x + \frac{1}{2}\delta^o(k_n)\right), \end{aligned} \tag{3.14}$$

where $k_n \equiv \sqrt{\omega_n^2 - M^2}$. Note that, in general, $\delta^e(k) \neq \delta^o(k)$. Equality occurs only if the potential is reflectionless. The wave numbers are determined by the periodic boundary conditions to be

$$2k_nL + \delta^{e,o}(k_n) = 2\pi n, \tag{3.15}$$

implying that the difference between adjoining momenta, $\Delta k = k_{n+1} - k_n$, is given as

$$2L\Delta k + \frac{d\delta^{e,o}}{dk}\Delta k = 2\pi,$$

which implies

$$\begin{aligned} \frac{1}{\Delta k} =& \frac{L}{\pi} + \frac{1}{2\pi}\frac{d\delta^{e,o}}{dk} \\ =& n^o(k) + \frac{1}{2\pi}\frac{d\delta^{e,o}}{dk}. \end{aligned} \tag{3.16}$$

Hence, the density of states per energy interval for the even and odd solutions can be written as

$$n_{e,o}(\omega) = n^0_{e,o}(\omega) + \frac{1}{2\pi}\frac{d\delta^{e,o}(\omega)}{d\omega}, \tag{3.17}$$

implying that the total density of states, $n = n_e + n_o$, is

$$n(\omega) = n^0(\omega) + \frac{1}{\pi}\frac{d\delta(\omega)}{d\omega}, \tag{3.18}$$

where

$$\delta(\omega) = \frac{1}{2}\Big(\delta^e(\omega) + \delta^o(\omega)\Big). \tag{3.19}$$

Suppose that Equation (3.8) has N bound states. The total number of states of the two Schrödinger equations must be equal,

$$N + \int_M^\infty n(\omega)d\omega = \int_M^\infty n^0(\omega)d\omega, \tag{3.20}$$

which implies that

$$\begin{aligned} N = -\int_M^\infty \Big(n(\omega) - n^0(\omega)\Big) &= -\int_M^\infty \frac{1}{\pi}\frac{d\delta}{d\omega}d\omega \\ &= \frac{1}{\pi}\Big(\delta(M) - \delta(\infty)\Big). \end{aligned} \tag{3.21}$$

If the potential is finite, then $\delta(\infty) = 0$, implying

$$N\pi = \delta(M). \tag{3.22}$$

This means that the phase shift at threshold is directly related to the number of bound states.

Now consider the calculation of the energy sums (3.9). Since we need to sum over the same number of states in the two systems before subtracting, we need two different cutoffs in each continuum. The cutoffs are related implicitly by

$$N + \int_M^{\bar{\Lambda}} n(\omega)d\omega = \int_M^{\Lambda} n^0(\omega)d\omega. \tag{3.23}$$

Using Equations (3.18) and (3.22) this relation becomes

$$\int_{\bar{\Lambda}}^{\Lambda} n(\omega)d\omega = N + \int_M^{\Lambda} \frac{1}{\pi}\frac{d\delta}{d\omega}d\omega = \frac{1}{\pi}\delta(\Lambda). \tag{3.24}$$

It will be shown a little later that at large energies, $\delta(\omega) \propto \omega^{-1}$. This fact combined with Eq. (3.13) that says that the density of states becomes constant at large energies implies

$$(\bar{\Lambda} - \Lambda) \propto \frac{1}{\Lambda} \text{ as } \Lambda \to \infty. \tag{3.25}$$

In terms of these cutoffs, the boson-loop energy is

$$\begin{aligned} E_{bl} =& \frac{1}{2} \sum_{\omega_i^2 < M^2} \omega_i + \lim_{\Lambda \to \infty} \Big[\frac{1}{2} \int_M^{\bar{\Lambda}} \omega n(\omega) d\omega - \frac{1}{2} \int_M^{\Lambda} \omega n^o(\omega) d\omega + E_{ct}(\Lambda) \Big] \\ =& \frac{1}{2} \sum_{\omega_i^2 < M^2} \omega_i + \lim_{\Lambda \to \infty} \Big[\frac{1}{2} \int_M^{\Lambda} \omega [n(\omega) - n^o(\omega)] d\omega + \frac{1}{2} \int_{\Lambda}^{\bar{\Lambda}} \omega n(\omega) d\omega + E_{ct}(\Lambda) \Big]. \end{aligned} \tag{3.26}$$

This expression can be simplified by noting that

$$\begin{aligned} \int_M^{\Lambda} \omega [n(\omega) - n^o(\omega)] d\omega &= \int_M^{\Lambda} \omega \frac{1}{\pi} \frac{d\delta}{d\omega} d\omega \\ &= \frac{1}{\pi} \Big[\omega \delta \Big|_M^{\Lambda} - \int_M^{\Lambda} \delta d\omega \Big] \\ &= \frac{1}{\pi} \Big[\Lambda \delta(\Lambda) - N\pi M - \int_M^{\Lambda} \delta d\omega \Big] \end{aligned} \tag{3.27}$$

and

$$\begin{aligned} \lim_{\Lambda \to \infty} \int_{\Lambda}^{\bar{\Lambda}} \omega n(\omega) d\omega &= \lim_{\Lambda \to \infty} \Lambda \int_{\Lambda}^{\bar{\Lambda}} n(\omega) d\omega \\ &= \lim_{\Lambda \to \infty} -\frac{1}{\pi} \Lambda \delta(\Lambda). \end{aligned} \tag{3.28}$$

The first equality in Eq. (3.28) follows from (3.25) and the last equality from (3.24). Combining (3.27) and (3.28) with (3.26) gives our final expression for the boson-loop energy,

$$E_{bl} = \frac{1}{2} \sum_{\omega_i^2 < M^2} (\omega_i - M) + \lim_{\Lambda \to \infty} \Big[-\frac{1}{2\pi} \int_M^{\Lambda} \delta(\omega) d\omega + E_{ct}(\Lambda) \Big], \tag{3.29}$$

which agrees with that of Reference [3] .

Equation (3.29) is an exact expression for the boson-loop energy in terms of the energies of the bound states and the phase shifts of the continuum states. Observe that since $\delta(M) \propto N$, the energies of the bound states end up being calculated relative to M as is sensible since the presence of the potential pulls the bound states down from the continuum threshold, implying an energy shift of $\omega_i - M$. Also, the continuum contribution is given simply as an integral over the phase shift. Since the phase shift generally varies smoothly, this integral can be evaluated accurately with only knowledge of δ at a sparse number of points. For a general background field, the phase shift is very straightforward to calculate numerically. If $\eta(x)$ is an exact solution of Eq. (3.8) that has the asymptotic form given by Eq. (3.14), then $kx_n + \frac{1}{2}\delta(k) \rightarrow n\pi$ as $x_n \rightarrow \infty$ where x_n is the nth zero of $\eta(x)$ greater than zero and k is the asymptotic momentum of $\eta(x)$. Hence,

$$\delta(k) = \lim_{n\rightarrow\infty} n\pi - kx_n. \tag{3.30}$$

This limit is easy to perform computationally by integrating (3.8) from x=0 towards infinity, counting each zero as it occurs, and computing $n\pi - kx_n$ until this value converges. This convergence occurs rapidly once the integration has extended past the range of the potential. This procedure leads to a very efficient method for "brute force" evaluating the boson-loop energy.

The calculation of the phase shift integral can be significantly improved by using the WKB approximation to get an analytical expression for the phase shift valid at large energies. The WKB approximation [17] states that solutions of

$$(\nabla^2 + k^2(x))\phi(x) = 0 \tag{3.31}$$

can be approximated by

$$\phi(x) \sim \frac{1}{\sqrt{k(x)}} \exp[i \int_0^x k(z)\, dz] \tag{3.32}$$

when the wavelength is much shorter than the distance scale over which k varies,

$$\frac{1}{k^2}\frac{dk}{dz} << 1. \tag{3.33}$$

Hence, the WKB solution becomes increasingly accurate at higher energies. For such solutions, the phase shift is simply computed as

$$\delta^{WKB}(k) = \int_{-\infty}^{\infty} [k(z) - k(\infty)]\, dz. \tag{3.34}$$

Since this gives the phase shift exactly at high energies, we can use this result to derive the scaling of the phase shift at high energies. Recall that $k^2(x) = \omega^2 - M^2(x)$, so

$$\begin{aligned} \delta^{WKB}(\omega) &= \int_{-\infty}^{\infty} dx \sqrt{\omega^2 - M^2(x)} - \sqrt{\omega^2 - M^2} \\ &= -\frac{1}{2}\Big(M^2(x) - M^2\Big)\frac{1}{\omega} + \mathcal{O}(\omega^{-3}). \end{aligned} \tag{3.35}$$

This verifies the scaling law ($\delta \propto 1/\omega$ at large ω) that was used earlier.

We now apply the WKB approximation towards evaluating the boson-loop energy. Inserting the WKB approximation for the energy states above some energy $\bar{\Lambda}$ in $\int \delta d\omega$ implies

$$\int_{\bar{\Lambda}}^{\Lambda} \delta^{\mathrm{WKB}}\, d\omega = \int_{\bar{\Lambda}}^{\Lambda} d\omega \int_{-\infty}^{\infty} dx \sqrt{\omega^2 - M^2(x)} - \sqrt{\omega^2 - M^2}. \tag{3.36}$$

Performing the energy integral gives

$$\begin{aligned}\int_{\bar{\Lambda}}^{\Lambda} \delta^{\mathrm{WKB}}\, d\omega = \int_{-\infty}^{\infty} dx\, \frac{1}{2}\Big[&\Lambda\sqrt{\Lambda^2 - M^2(x)} - \Lambda\sqrt{\Lambda^2 - M^2} \\ &- M^2(x)\log(\Lambda + \sqrt{\Lambda^2 - M^2(x)}) + M^2\log(\Lambda + \sqrt{\Lambda^2 - M^2}) \\ &- (\text{lower limit of integration})\Big].\end{aligned} \tag{3.37}$$

This integral is logarithmically divergent. Upon isolating this divergence the integral becomes

$$\begin{aligned}\int_{\bar{\Lambda}}^{\Lambda} \delta^{\mathrm{WKB}}\, d\omega &= \int_{-\infty}^{\infty} dx\, \frac{1}{2}\Big[\Lambda\sqrt{\Lambda^2 - M^2(x)} - \Lambda\sqrt{\Lambda^2 - M^2} \\ &\quad - M^2(x)\log\Big(\frac{\Lambda + \sqrt{\Lambda^2 - M^2(x)})}{\Lambda + \sqrt{\Lambda^2 - M^2}}\Big) \\ &\quad - (\text{lower limit of integration}) \\ &\quad + (M^2 - M^2(x))\log(\Lambda + \sqrt{\Lambda^2 - M^2})\Big] \\ &= \int_{-\infty}^{\infty} dx\, \alpha(\phi, \bar{\Lambda}, \Lambda) + \frac{1}{2}(M^2 - M^2(x))\log\Big(\frac{\Lambda + \sqrt{\Lambda^2 - M^2}}{M}\Big),\end{aligned} \tag{3.38}$$

where $\alpha(\phi, \bar{\Lambda}, \Lambda)$ denotes the finite part of the integral. As $\Lambda \to \infty$, this becomes an analytic expression denoted $\alpha(\phi, \bar{\Lambda})$. When this expression is inserted into the formula for the boson-loop energy (3.29), the infinite part is completely cancelled by the counterterm. If we evaluate the phase shift exactly below $\bar{\Lambda}$ and use the WKB approximation for higher energies, then the boson-loop energy is

$$E_{bl} = \frac{1}{2}\sum_{\omega_i^2 < M^2} (\omega_i - M) - \frac{1}{2\pi}\int_M^{\bar{\Lambda}} \delta(\omega) d\omega - \frac{1}{2\pi}\lim_{\Lambda\to\infty}\int_{-\infty}^{\infty} dx\, \alpha\Big(\phi(x), \bar{\Lambda}\Big). \tag{3.39}$$

This expression can be made arbitrarily exact by increasing $\bar{\Lambda}$. All of the high-energy behavior has been incorporated into an analytical expression α, which was our primary

goal. Because of this, there is no need to calculate things to very high precision in order to get a convergent result. By using Eq. (3.39), we need only to calculate the individual terms to the same precision at which the final answer is desired.

It is interesting to ask how this WKB approximation relates to the local density approximation discussed in Chapter 2. Consider a potential $M^2(x)$ that has value $(M^*)^2 < M^2$ in a region of length $2L$ and then rises up to M^2 in a region of space small compared to L, as shown in Fig. 3.2. We now evaluate the boson-loop energy corresponding to this choice of $M^2(x)$, using the WKB method for the entire

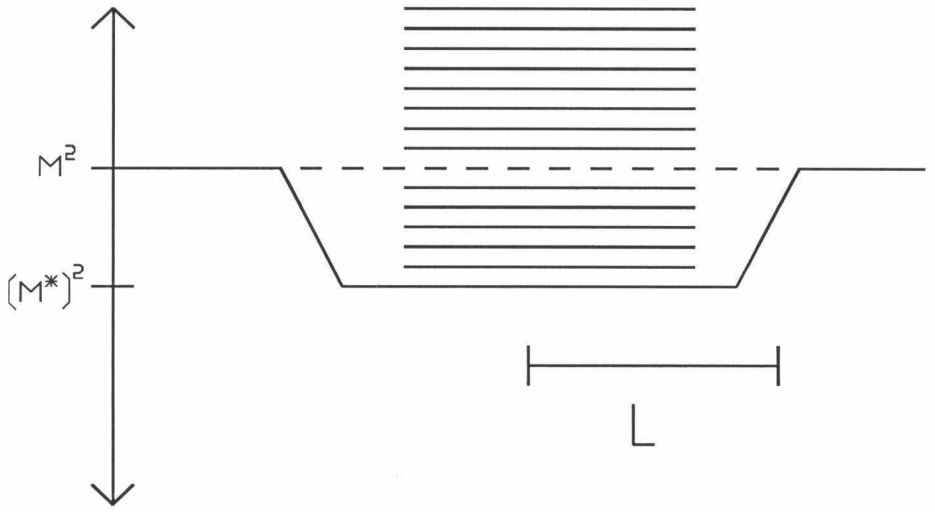

Figure 3.2 – WKB method for slowly varying potentials. The solid line shows $M^2(x)$ as a function of x for a case in which it equals $(M^*)^2$ over a length $2L$ that is large compared to the distance over which it changes values. In this case, the wavefunctions in the regime $-L < x < L$ can be approximated as plane waves with mass M^*, in which case the WKB approximation and the local density approximation give identical results.

continuum.

For large L,

$$\begin{aligned}\lim_{\Lambda\to\infty}\int_M^\Lambda d\omega\,\delta_{\rm WKB}(\omega) = \lim_{\Lambda\to\infty}\int_{-L}^{L} dx\int_M^\Lambda d\omega\,\sqrt{\omega^2-(M^*)^2}-\sqrt{\omega^2-M^2}\\ =\frac{1}{2}\Big[\frac{1}{2}(M^2-(M^*)^2)-M\sqrt{M^2-(M^*)^2}\\ -(M^*)^2\log\Big(\frac{M}{M+\sqrt{M^2-(M^*)^2}}\Big)\\ +(M^2-(M^*)^2)\log(\frac{2\Lambda}{M})\Big],\end{aligned} \tag{3.40}$$

implying

$$\lim_{\Lambda\to\infty}\Big[-\frac{1}{2\pi}\int_M^\Lambda d\omega + E_{\rm ct}(\Lambda)\Big] = \\ -\frac{1}{4\pi}\Big[\frac{1}{2}(M^2-(M^*)^2) - M\sqrt{M^2-(M^*)^2} \\ -(M^*)^2\log\Big(\frac{M}{M+\sqrt{M^2-(M^*)^2}}\Big)\Big]. \tag{3.41}$$

Also, if L is large the bound states will be similar to plane waves over the interior of the potential that die off rapidly at distances greater than L; hence,

$$\frac{1}{2}\sum_{\omega_i^2<M^2}(\omega_i - M) = \int_{-L}^{L}dx\int_{-\sqrt{M^2-(M^*)^2}}^{\sqrt{M^2-(M^*)^2}}\frac{dk}{2\pi}(\sqrt{k^2+(M^*)^2}-M) \\ = \int_{-L}^{L}\frac{1}{4\pi}\Big[-M\sqrt{M^2-(M^*)^2} \\ +(M^*)^2\log\Big(\frac{\sqrt{M^2-(M^*)^2}+M}{M^*}\Big)\Big]. \tag{3.42}$$

Combining (3.42) and (3.41) gives

$$E_{\rm bl} = \int_{-L}^{L}dx\,\frac{1}{8\pi}\Big[(M^*)^2 - M^2 - (M^*)^2\log\big(\frac{(M^*)^2}{M^2}\big)\Big] \tag{3.43}$$

that is identical with the expression for the LDA (see Chapter 2, Eq. (2.81)). Hence, for slowly varying potentials, the WKB approximation agrees with the local density approximation.

3.2 Boson-Loop Calculations

We now apply the WKB method to explicit boson-loop calculations. We begin by calculating the boson-loop corrections to the kink soliton. As these corrections have been calculated previously, this provides a good testing ground for the WKB method. We then go on to discuss the problem of including these corrections self-consistently.

The kink soliton is determined from the scalar boson Lagrangian (3.1) with

$$V(\phi) = -\frac{1}{2}M^2\phi^2 + \frac{1}{4}\lambda\phi^4. \tag{3.44}$$

This potential, which is graphed in Fig. 3.3 for $m = \lambda = 1$, has two degenerate minima at

$$|\phi| = \frac{m}{\sqrt{\lambda}}. \tag{3.45}$$

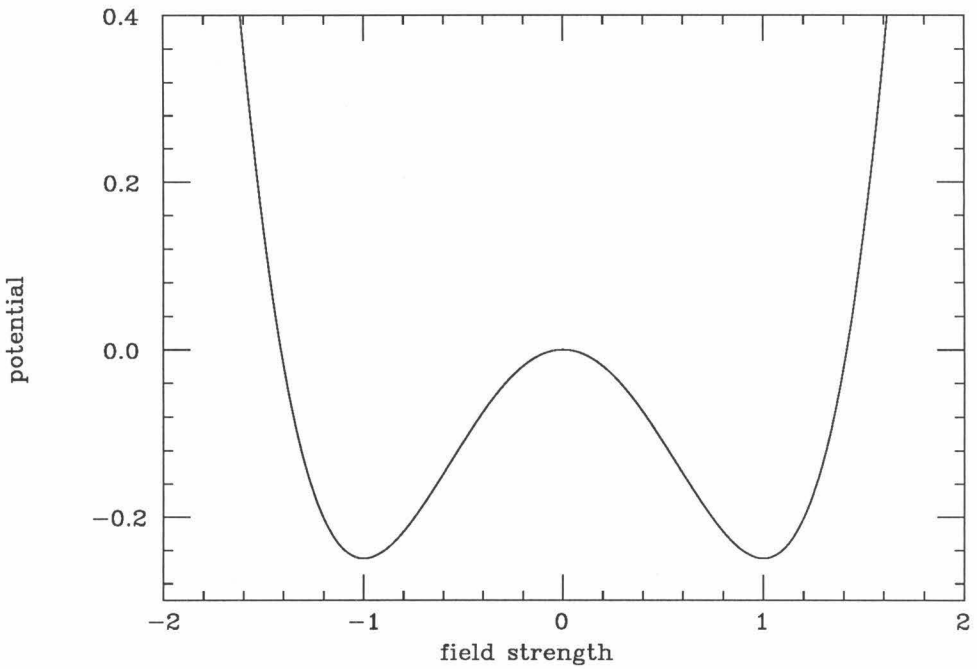

Figure 3.3 – Classical potential , Eq. (3.44) with $m = \lambda = 1$, that gives rise to the Kink soliton. The potential has two degenerate vacuums at $\phi = \pm 1$ and an unstable maximum at $\phi = 0$. The kink soliton is a classically stable solution that occupies the left vacuum at $x = -\infty$ and the right vacuum at $x = +\infty$. The region of the potential between $\phi = -1$ and $\phi = 1$ is concave down so that local expressions for the boson-loop energy are inapplicable.

In addition to these translationally invariant static solutions, the classical equation of motion,

$$(\partial^\mu \partial_\mu - m^2 + \lambda\phi^2)\phi = 0, \tag{3.46}$$

also admits a localized static solution,

$$\phi_k(x) = \frac{m}{\sqrt{\lambda}} \tanh\left(\frac{mx}{\sqrt{2}}\right), \tag{3.47}$$

called the kink soliton [18]. This solution occupies both of the local minima of the classical potential, connecting one minimum at $x = -\infty$ with the other minimum at $x = +\infty$, resulting in a non-zero energy density centered at zero. The classical energy of the kink soliton is

$$E_{\text{classical}} = \int_{-\infty}^{\infty} dx \, \frac{1}{2}(\nabla\phi_k)^2 + V(\phi_k) = \frac{2\sqrt{2}}{3}\frac{m^3}{\lambda}. \tag{3.48}$$

Upon quantizing the theory one expects to see particle states corresponding to both scalar mesons and solitons. The modes of oscillation of the scalar field about the solution ϕ obey the Klein-Gordon equation with the potential

$$M^2(x) = V''(\phi) = -m^2 + 3\lambda\phi^2 \tag{3.49}$$

that equals $2m^2$ in the vacuum states. Hence, quantum excitations in the vacuum consist of scalar mesons with mass $\sqrt{2}m$. We can also quantize about the kink soliton, generating a set of of quantum states representing one kink soliton plus any number of mesons.

We now calculate the one boson-loop energy corresponding to the classical kink solution. The modes of oscillation of the scalar field with respect to the kink are given by

$$[-\nabla^2 - m^2 + 3\lambda\phi_k(x)^2]\eta_n = \omega_n^2\eta_n \tag{3.50}$$

and consist of a continuum starting at $\omega_n^2 = 2m^2$ and some discrete states. The continuum modes can be interpreted as scattering states of scalar mesons off the kink soliton, while the discrete states correspond to vibrational modes of the soliton.

Solving Eq. (3.50) yields two bound states with energies

$$\omega_{\text{bound}} = 0 \text{ and } \sqrt{\frac{3}{2}}m. \tag{3.51}$$

The $\omega = 0$ state corresponds to the translational mode of the kink. Since the underlying theory is translationally invariant, the classical kink solution can exist centered at any point in space. One "mode of oscillation" consists of giving the kink a uniform boost, in which case it will keep on moving and never come back, corresponding to a period of infinity and therefore a frequency of zero. Hence, any finite solution found in a translationally invariant theory will have such a mode.

The phase shift can also be calculated analytically (see Appendix C) to be

$$\delta(k) = 2\pi - 2\arctan(\frac{\sqrt{2}k}{m}) - 2\arctan(\frac{k}{\sqrt{2}m}) \tag{3.52}$$

where $\omega^2 = k^2 + 2m^2$. Inserting this into the equation for the boson-loop energy we find [3] that

$$E_{\text{bl}} = [\frac{1}{2\sqrt{6}} - \frac{3}{\pi\sqrt{2}}]m = -0.47111\, m. \tag{3.53}$$

We now apply our WKB method to the same problem. The WKB phase shift is calculated using Eq. (3.34). The results are plotted in Fig. 3.4, along with the exact phase shift. Observe that at $k = 0$ the actual phase shift is 2π, reflecting the existence of the two bound states, while the WKB phase shift is about 20% larger. As the energy is increased, the two rapidly approach each other, becoming indistinguishable when $k \sim m$. This implies that to get an accurate result, we will have to use the exact phase shifts up to this point.

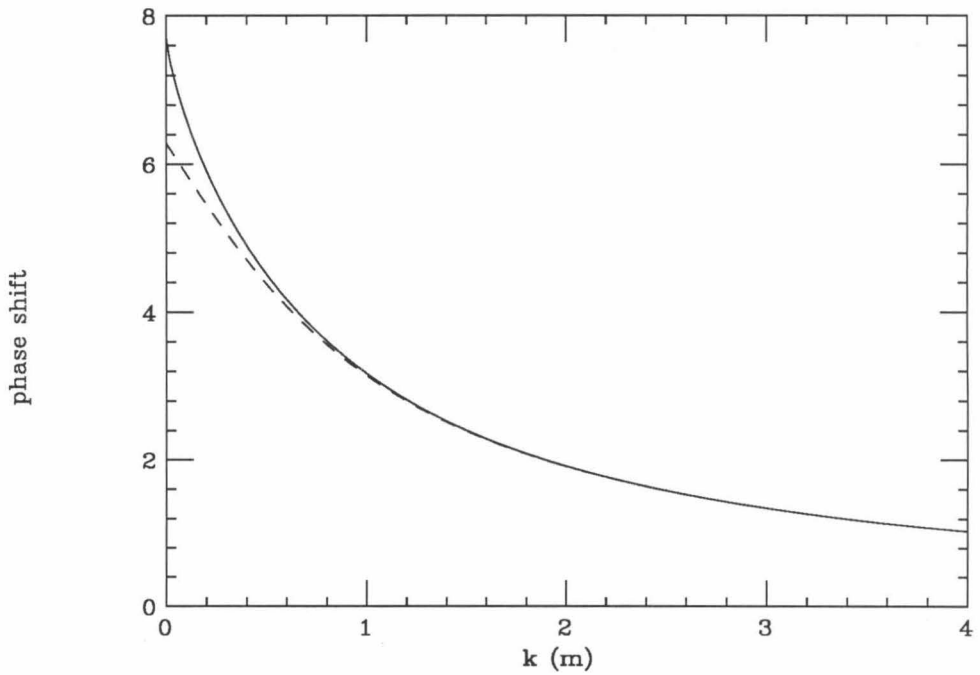

Figure 3.4 – Phase shifts for the kink soliton vs. momentum. The dashed line is the exact phase shift and the solid line is the WKB phase shift.

This is confirmed by actually calculating the loop energy, shown in Table 3.1. Exact phase shifts are used for energies below $\bar{\Lambda}$. Although the exact phase shifts are known analytically, in these calculations the exact phase shift was calculated

numerically using the algorithm given by Equation (3.30) in order to test out the full machinery of our numerical method. More details about the numerical method are given in Appendix D. When the WKB approximation is used for the entire phase shift, the energy is calculated to an accuracy of 2%. This accuracy rapidly improves by inserting the exact phase shift at low energies, with an accuracy of 0.05% being obtained when $\bar{\Lambda}$ is twice the scalar boson mass. This accuracy can be obtained by calculating seven exact phase shifts and using Simpson's rule. The exact phase shift integrals are evaluated most efficiently if they are discretized in momentum space, using

$$\int \delta(\omega) d\omega = \int \delta(k) \frac{k}{\sqrt{k^2 + 2m^2}} dk. \tag{3.54}$$

$\bar{\Lambda}/\sqrt{2}m$	$-E_{\rm bl}/m$	accuracy
1.0	0.4787	$\sim 2\%$
1.1	0.4738	
2.0	0.4713	$\sim 0.5\%$
4.0	0.47112	
8.0	0.47111	

Table 3.1 – Calculation of boson-loop correction to kink soliton using the WKB method. Exact phase shifts are used for energies below $\bar{\Lambda}$ and WKB phase shifts above. The exact answer is $E_{\rm bl} = -0.47111\, m$.

One remaining question is how much of the finite part of the answer the WKB approximation gets right. This is answered by comparing how accurate a brute force calculation up to maximum energy $\bar{\Lambda}$ is compared to a WKB calculation that uses exact phase shifts up to this same energy. The brute-force calculations are performed

by using Eq. (3.29) directly. This involves evaluating the phase shift integral and the couterterm separately and then adding them together. Results of such a calculation are shown in Table 3.2.

$\Lambda/\sqrt{2}m$	$-E_{\rm bl}/m$	accuracy
1.1	0.6068	$\sim 50\%$
2.0	0.4952	$\sim 5\%$
4.0	0.4766	
8.0	0.4724	
16.0	0.4714	$\sim 0.5\%$
32.0	0.4712	

Table 3.2 – Brute-force calculation of boson-loop correction to kink soliton. Exact phase shifts are integrated up to energy Λ

The convergence of the brute-force calculation is much slower than the WKB, indicating that the WKB gets the finite contribution of the high energies very accurately. For instance, to get the accuracy of the WKB approximation with $\bar{\Lambda} = 2\sqrt{2}m$ with the brute-force method requires a cutoff of $\bar{\Lambda} = 16\sqrt{2}m$, meaning that the brute-force calculation requires at least 8 times as much computation. In fact, the actual computation required is greater since the phase shift integral must be computed much more accurately in the brute force calculation than the WKB calculation, since the integral is dominated by the diverging counterterm contribution that is subtracted after the calculation.

Since the actual scalar field should minimize the effective action, we are motivated now to try to minimize the one-loop approximation to the effective action. This runs into immediate problems. Since the boson-loop energy is negative, the soliton

wants to expand in order to minimize its total energy. When it expands, all of the bound states of (3.8) become more bound. In particular, the translation mode eigenvalue becomes negative ($\omega_0^2 < 0$), implying that the boson-loop approximation has broken down (see Section 2.2).

In order to see this explicitly, Fig. 3.5 plots the energy of the dilated kink as a function of a scale factor a where the dilated kink soliton $\phi_a(x)$ is defined by

$$\phi_a(x) = \phi_k(x/a). \tag{3.55}$$

For $a < 1$ the soliton is smaller and the translational mode contributes a real portion to the energy, while for $a > 1$ the soliton is larger and the translation mode contributes an imaginary part of the energy. The disappearance of the translation mode from the real part of the spectrum is reflected by a kink in the curve of Fig. 3.5.

This breakdown indicates that it is inconsistent to minimize the one-loop approximation. The problem is that the boson-loop correction is the first-order quantum correction to the exact classical solution. When we attempt to minimize this energy, we are adding in higher loop effects but not in any systematic manner. This allows the energy to become complex. In this case, the problem is due to applying the saddle-point approximation to a problem with a broken translational symmetry because the approximation is not valid for fluctuations that translate the finite system, as the translated states all have the same energy. Alternative quantization schemes have to be used in which the translational degree of freedom is explicitly taken into account [18]. A discussion of these methods is outside the scope of this thesis.

In order to understand the WKB approximation better, consider the boson-loop corrections to a background field of the form

$$\phi(x) = 1 - \frac{\phi_b}{1 + \exp(\frac{x^2 - R^2}{T^2})}, \tag{3.56}$$

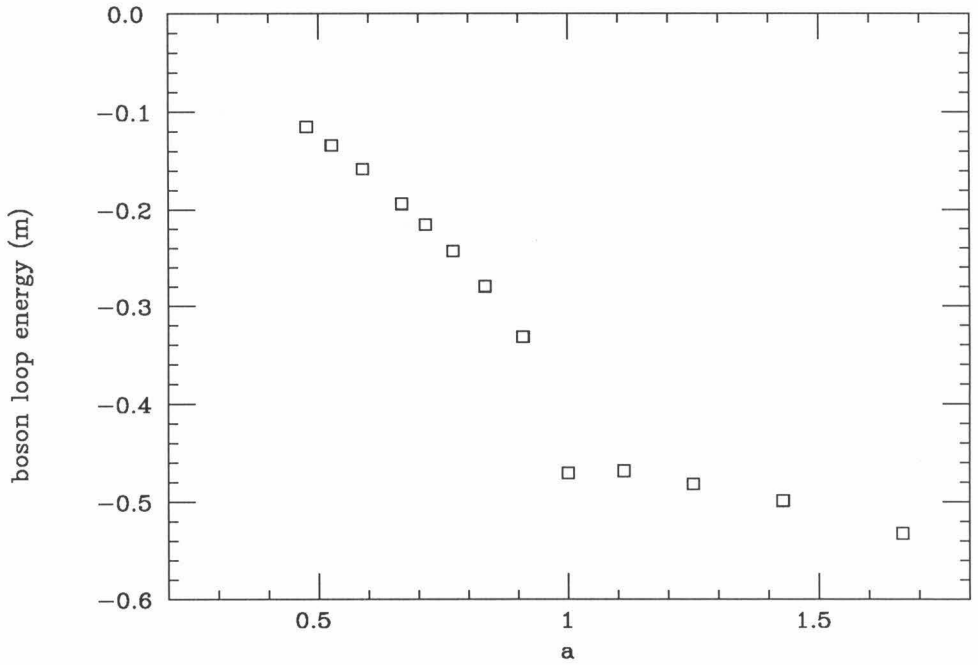

Figure 3.5 – One-loop energy of the kink soliton as a function of scale a. For $a > 1$, the energy is complex and only the real part is shown.

where ϕ_b, R, and T are parameters that allow us to adjust the depth and surface thickness of the background field. The potential in the Lagrangian is assumed to be the kink potential with $m = \lambda = 1$, implying

$$V''(\phi) = 3\phi^2 - 1. \tag{3.57}$$

Observe that if at any point $\phi < \sqrt{3}/3$, then the local density approximation will fail. Table 3.3 shows the results of calculations for various sets of parameters, both exact, using the LDA, and using the WKB approximation for the entire continuum. The exact calculations are performed using the WKB method with $\bar{\Lambda} = 2\sqrt{2}$. Also

ϕ_b	R	T	$-E_{\rm bl}$	$\omega^2_{\rm bs}$	$-E_{\rm LDA}$	$-E_{\rm WKB}$
0.2	1	0.5	0.021	1.52	0.024	0.030
0.3	1	0.5	0.047	1.20	0.056	0.058
0.4	1	0.5	0.083	0.90	0.106	0.092
0.5	1	0.5	0.129	0.63	-	0.133
0.6	1	0.5	0.188	1.97	-	0.186
				0.39		
0.2	10	5.0	0.240	1.87	0.242	0.242
				1.70		
				1.52		
				1.35		
				1.20		
				1.07		
				0.98		

Table 3.3 – Comparison of boson-loop energy with local density approximation for the background field of Eq. (3.56). The first three columns are the parameters that describe the background field, $E_{\rm bl}$ is the exact boson-loop energy, $\omega^2_{\rm bs}$ is the energy squared of the bound states , $E_{\rm LDA}$ is the boson-loop energy calculated via the local density approximation, and $E_{\rm WKB}$ is the energy calculated using the WKB approximation in the entire continuum.

displayed in the table are the energies of the bound states. For some of these parameters, the one-loop energy has also been calculated by Li, Perry, and Wilets [14]. Our results agree with theirs.

The first five parameter sets increase the strength of the field up to and past the point where the local density approximation fails. These fields are all characterized by one bound state, except at the largest field strenth. We first examine the results

for the LDA. The LDA is accurate to about 20% up to the point where it abruptly fails. Notice, however, that the actual energy is perfectly continuous through this point. The primary reason for the inaccuracy of the local density approximation in this regime is that the boson-loop energy is significantly influenced by the energy of the isolated bound state, an effect that is largely missed by the LDA. It is interesting to note that the E_{WKB} calculations, which know about the isolated bound state but treats the continuum locally, even do worse at the low field values. This is because, as the bound state moves away from the continuum, there is still significant distortion in the continuum from its leaving, and local approximations miss this. The LDA, by missing both the distortion in the continuum and the isolated bound state, is able to do better than the WKB. As the field strength is increased and the bound state moves farther away from the continuum, the WKB does better than the LDA and becomes an increasingly good approximation to the full calculation. Finally, if the field strength is increased much beyond the maximum value shown in the table, the value of ω^2 of the most bound state becomes negative and the boson-loop correction turns complex.

The sixth parameter set increases the size of the field, keeping the strength the same as in the first set. Here there are 7 bound states instead of one. In this case the accuracy of the LDA is improved by an order of magnitude and the full WKB gives a nearly identical result, as is expected from the results in Section 3.1.

3.3 WKB Method for Fermion Vacuum Energy

We now develop the WKB method for the calculation of the one-fermion-loop energy in the presence of a background scalar field. As with the bosons, we implement the phase-shift method of [3] and apply the WKB approximation. The Lagrangian

is

$$\mathcal{L} = \mathcal{L}_{\text{boson}} + \bar{\psi}(i\gamma^\mu \partial_\mu - g\phi)\psi, \tag{3.58}$$

where the gamma matrices are taken to be

$$\gamma^0 = \begin{pmatrix} 0 & -i \\ i & 0 \end{pmatrix} \text{ and } \gamma^1 = \begin{pmatrix} i & 0 \\ 0 & -i \end{pmatrix}. \tag{3.59}$$

Note that in $1+1$ dimensions the fermions are spinless. Also, since $\mathcal{L}$ has dimension $(\text{mass})^2$ and ϕ is dimensionless, the dimension of ψ is $(\text{mass})^{1/2}$ and the dimension of g is $(\text{mass})^1$. We write the wavefunction as

$$\psi(x) = \begin{pmatrix} iF \\ G \end{pmatrix} \exp(-i\omega t) \tag{3.60}$$

that implies the relations

$$\begin{aligned} \psi^\dagger \psi &= F^2 + G^2 \\ \bar{\psi}\psi &= -2FG \end{aligned}. \tag{3.61}$$

In terms of F and G, the Dirac equation is

$$\frac{\partial}{\partial x}\begin{pmatrix} F \\ G \end{pmatrix} = \begin{pmatrix} g\phi & \omega \\ -\omega & -g\phi \end{pmatrix}\begin{pmatrix} F \\ G \end{pmatrix}. \tag{3.62}$$

Since ϕ is real, the above equation implies that we can take F and G to be real. Observe that if $\psi = \begin{pmatrix} iF \\ G \end{pmatrix}$ is a solution with energy ω, then $\psi^\dagger = \begin{pmatrix} -iF \\ G \end{pmatrix}$ is a

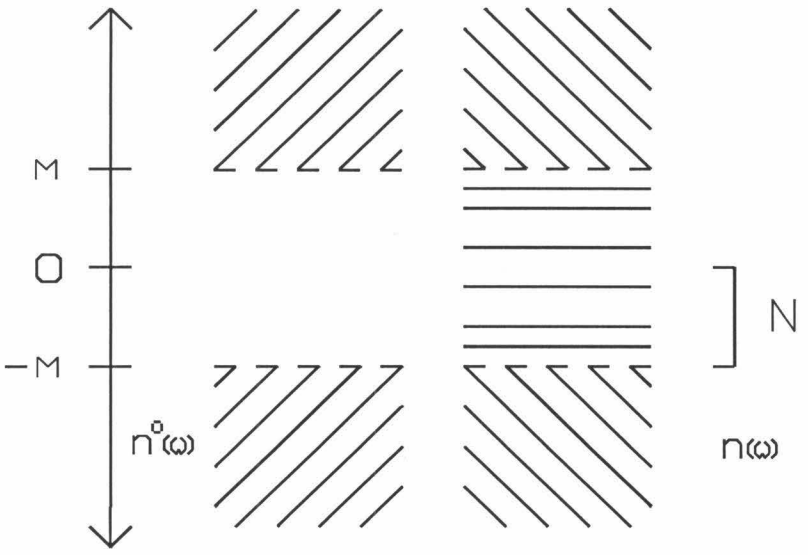

Figure 3.6 – Energy spectrum of the eigenstates of the Dirac equation coupled to a scalar field. The vertical axis plots the energy. The spectra are symmetric about $\omega = 0$. The first column is the vacuum spectra that consist of two continua stretching from $\pm M$ to $\pm\infty$ described by a density of states $n^0(\omega)$. The second column is the spectra in the presence of a background field that consists of N bound negative-energy states and a negative-energy continuum that is described by a density of states $n(\omega)$. If the scalar field is antisymmetric, then there also exists a state with $\omega = 0$.

solution with energy $-\omega$. Thus, the energy spectrum is symmetric about $\omega = 0$, as shown in Fig. 3.6.

The coupled single-order differential equation can be transformed into the two second-order equations,

$$\begin{aligned}(\nabla^2 - g^2\phi^2 + g\frac{\partial\phi}{\partial x})G &= -\omega^2 G \\ (\nabla^2 - g^2\phi^2 - g\frac{\partial\phi}{\partial x})F &= -\omega^2 F.\end{aligned} \tag{3.63}$$

If the scalar field is uniform, then the energy spectra is

$$\omega^0(k) = \pm\sqrt{k^2 + (g\phi)^2}, \tag{3.64}$$

meaning that the fermions behave as if they have mass $|g\phi|$. In the examples that follow, we will be interested in spatially varying solutions that reach some value $|g\phi_v|$ where ϕ_v is a vacuum value of the scalar field.

We first consider the fermion-loop corrections for an antisymmetric scalar field $\phi(x)$. This situation arises when fermions are coupled to the solitons discussed in the previous sections. We denote $|g\phi(\infty)| = M$, where M is the asymptotic mass of the fermion.

If ϕ is antisymmetric then $g^2\phi^2$ and $\partial\phi/\partial x$ are both symmetric, which means that the solutions of Eq. (3.63) can be classified by their parities. The density of states corresponding to these two equations can be calculated by the method of Section 3.1 to be

$$n_{F,G}(\omega) = n^0_{F,G}(\omega) + \frac{1}{\pi}\frac{d\delta_{F,G}(\omega)}{d\omega}, \tag{3.65}$$

where $\delta_{F,G}$ are the phase shifts associated with the Schrödinger equations (3.63) that are decomposed into odd parity and even parity phase shifts as

$$\delta_{F,G} = \frac{1}{2}(\delta^e_{F,G} + \delta^o_{F,G}). \tag{3.66}$$

These density of states for the boson equations now need to be transformed into the density of states of the Dirac equation in which each solution corresponds to a (F,G) pair. Equation (3.62) implies that an even parity F corresponds to an odd parity G and vice-versa. By switching the relative sign between F and G, we generate

both a positive and negative energy solution. The only exception to this rule is a state with $\omega = 0$. It turns out that such a solution always exists for an antisymmetric ϕ since the equation

$$\frac{\partial G}{\partial x} = -g\phi(x)G \tag{3.67}$$

is always solved by the normalizable function

$$G_0(x) = G_0 \exp[-\int_0^x g\phi(z)dz], \tag{3.68}$$

implying that

$$\psi_0(x) = \begin{pmatrix} 0 \\ G(x) \end{pmatrix} \tag{3.69}$$

is a solution of the Dirac equation with energy 0. The implications of this zero-energy state are discussed in [18]. This is an even parity G solution that has no antisymmetric F counterpart. As a result, if there are N bound non-zero negative energy states, then the Schrödinger equation for G has $N + 1$ bound solutions and the Schrödinger equation for F has N bound solutions, so

$$\begin{aligned} \delta_F(m) =& \pi N \\ \delta_G(m) =& \pi(N+1). \end{aligned} \tag{3.70}$$

We determine the density of states of the Dirac equation by solving it in a box of length $2L$ and impose periodic boundary conditions on the the spinor. As the even components of the spinor always satifsfy the periodicity requirement, the boundary condition is effectively a boundary condition on the odd component. The phase shifts of the odd components of the spinors are given by the phase shifts of the odd solutions to Eq. (3.63), which implies that the density of states of the Dirac equation is

$$n(\omega) = n^0(\omega) + \frac{1}{\pi}\frac{d\delta}{d\omega},$$

where

$$\delta(\omega) = {}^{o}\delta_F(|\omega|) + {}^{o}\delta_G(|\omega|). \tag{3.71}$$

Since the odd solutions are related to the even solutions by Eq. (3.62), we find by substituting in the asymptotic forms of the odd solutions that

$$\begin{aligned} {}^{e}\delta_F(\omega) &= {}^{o}\delta_G(\omega) + \arctan\left[\frac{M}{k}\right] \\ {}^{e}\delta_G(\omega) &= {}^{o}\delta_F(\omega) - \arctan\left[\frac{M}{k}\right], \end{aligned} \tag{3.72}$$

implying

$${}^{e}\delta_G(\omega) + {}^{e}\delta_F(\omega) = {}^{o}\delta_G(\omega) + {}^{o}\delta_F(\omega).$$

Hence, the total phase shift can be written

$$\delta(\omega) = \frac{1}{2}\Big(\delta_F(\omega) + \delta_G(\omega)\Big) \tag{3.73}$$

that implies, in particular,

$$\delta(0) = (N + \frac{1}{2})M. \tag{3.74}$$

This can be interpreted as saying that the $\omega = 0$ state is created half from the positive-energy continuum and half from the negative-energy continuum.

Using this density of states, we can calculate the fermion-loop using the same procedure as in Section (3.1). The fermion-loop energy is

$$E_{\text{fl}} = \lim_{\Lambda\to\infty} \sum_{-\Lambda<\omega_i<0} (\omega_i - \omega_i^0) + E_{ct}(\Lambda),$$

where the counterterm is calculated in Appendix A to be

$$E_{ct}(\Lambda) = \frac{1}{4\pi}\log\left(\frac{4\Lambda^2}{M^2}\right)(g^2\phi^2 - M^2). \tag{3.75}$$

From the arguments in Section (3.1) it follows that

$$\begin{aligned} E_{\rm fl} &= \sum_{-M<\omega_i<0} \omega_i + \frac{1}{\pi}\delta(0) + \lim_{\Lambda\to\infty}\left[\frac{1}{\pi}\int_{-M}^{-\Lambda}\delta(\omega)d\omega + E_{\rm ct}(\Lambda)\right] \\ &= \sum_{-M<\omega_i<0} (\omega_i + M) + \frac{1}{2}M + \lim_{\Lambda\to\infty}\left[\frac{1}{\pi}\int_{M}^{\Lambda}\delta(\omega)d\omega + E_{\rm ct}(\Lambda)\right]. \end{aligned} \tag{3.76}$$

Observe that the zero-energy state is responsible for a contribution of $0+0.5m$ to the energy as opposed to the negative-energy bound states that contribute $\omega_i + M$ to the energy. This is a reflection of the fact that the $\omega = 0$ state is formed half from the positive-energy sector and half from the negative-energy sector.

These results can be understood by realizing that the "vacuum" of this system consists of two degenerate fermion states. These states correspond to having the $\omega = 0$ state occupied ($|+\rangle$) and to having the $\omega = 0$ state unoccupied ($|-\rangle$). Since these two states differ by a single particle state that has zero energy, these states are degenerate in energy. Let B^+ and B^- denote the fermion numbers of each of these states. The occupied state has one more fermion than the unoccupied state, so

$$B^+ - B^- = 1. \tag{3.77}$$

On the other hand, the two states can be transformed into each other by changing all the holes into particles and particles into holes, implying

$$B^+ = -B^-. \tag{3.78}$$

Hence, $B^+ = 1/2$ and $B^- = -1/2$ so that this state contributes only $1/2$ to the baryon number that is consistent with the fact that it contributes only $0.5m$ to the energy.

We introduce the WKB approximation by using it to approximate the phase shifts of the Schrödinger-type Equations (3.63). The result is

$$\begin{aligned}\delta_{\mathrm{WKB}}(\omega) = \int_{-\infty}^{\infty} dx \, \frac{1}{2}\Big[\sqrt{\omega^2 - g^2\phi(x)^2 + g\frac{\partial\phi}{\partial x}} \\ + \sqrt{\omega^2 - g^2\phi(x)^2 - g\frac{\partial\phi}{\partial x}} - 2\sqrt{\omega^2 - M^2}\Big].\end{aligned} \tag{3.79}$$

This equation assumes implicitly that

$$g^2\phi(x)^2 \pm g\frac{\partial\phi}{\partial x} < M^2 \tag{3.80}$$

at all points x. If not, then the above approximation can be used only for energies ω that satisfy

$$\omega^2 > \max\Big(g^2\phi(x)^2 \pm g\frac{\partial\phi}{\partial x}\Big), \tag{3.81}$$

and other methods must be used for lower energies. The energy integral of the WKB phase shift can be performed analogously to the boson case. Using the convenient notation

$$\begin{aligned}M_+^2(x) =& g^2\phi(x)^2 + g\frac{\partial\phi}{\partial x} \\ M_-^2(x) =& g^2\phi(x)^2 - g\frac{\partial\phi}{\partial x}\end{aligned} \tag{3.82}$$

and the result of Equation (3.38), the energy integral is

$$\begin{aligned}\int_{\bar{\Lambda}}^{\Lambda} \delta^{\mathrm{WKB}}\, d\omega = \int_{-\infty}^{\infty} dx\, \frac{1}{4}\Big[&\Lambda\sqrt{\Lambda^2 - M_+^2(x)} + \Lambda\sqrt{\Lambda^2 - M_-^2(x)} - 2\Lambda\sqrt{\Lambda^2 - M^2} \\ &- M_+^2(x)\log\Big(\frac{\Lambda + \sqrt{\Lambda^2 - M_+^2(x)})}{\Lambda + \sqrt{\Lambda^2 - M^2}}\Big) \\ &- M_-^2(x)\log\Big(\frac{\Lambda + \sqrt{\Lambda^2 - M_-^2(x)})}{\Lambda + \sqrt{\Lambda^2 - M^2}}\Big) \\ &- (\text{lower limit of integration}) \\ &+ (2M^2 - M_+^2(x) - M_-^2(x))\log(\Lambda + \sqrt{\Lambda^2 - M^2})\Big] \\ = \int_{-\infty}^{\infty} dx\, \alpha_f(\phi, \bar{\Lambda}, \Lambda) &+ \frac{1}{2}(M^2 - g^2\phi(x)^2)\log\Big(\frac{\Lambda + \sqrt{\Lambda^2 - M^2}}{M}\Big),\end{aligned} \tag{3.83}$$

where $\alpha_f(\phi, \bar{\Lambda}, \Lambda) = \alpha_f(\phi, \bar{\Lambda})$ as $\Lambda \to \infty$ is the finite part of the integral. By inserting this expression into Eq. (3.76), we see that the logarithmic divergence is exactly cancelled by the counterterm leaving

$$E_{fl} = 0.5M + \sum_{-M<\omega_i<0} (\omega_i + M) + \frac{1}{\pi}\int_M^{\bar{\Lambda}} \delta(\omega) d\omega + \frac{1}{\pi}\lim_{\Lambda\to\infty}\int_{-\infty}^{\infty} dx\, \alpha_f\Big(\phi(x), \bar{\Lambda}\Big). \tag{3.84}$$

We emphasize that this formula is applicable only for antisymmetric scalar fields.

We now apply this formalism to the calculation of the fermion-loop corrections to the kink soliton. The Lagrangian is as given in Equation (3.58) with $\mathcal{L}_{\mathrm{boson}}$ being the Lagrangian for the kink soliton given by Equation (3.44). In terms of the parameters of this Lagrangian, the Dirac equation is

$$\Big[i\gamma^1\frac{\partial}{\partial x} + g\frac{m}{\sqrt{\lambda}}\tanh\Big(\frac{x}{\sqrt{2}m}\Big)\Big]\psi(x) = \gamma^0\omega\psi(x) \tag{3.85}$$

that implies

$$M = \frac{gm}{\sqrt{\lambda}}. \tag{3.86}$$

There are three parameters with dimension mass that combine to make up the fermion mass. It is most convenient to define the dimensionless parameter G,

$$G = \frac{g}{\sqrt{\lambda}}, \tag{3.87}$$

and to measure everything in terms of the meson mass m. In particular, the substitution $x \to mx$ factors m out of the Dirac equation implying that the fermion-loop correction at fixed G is proportional to m.

$G/\sqrt{2}$	$\bar{\Lambda}/m$	$E_{\rm WKB}/m$	$E_{\rm BF}/m$	$E_{\rm ND}/m$
1.0	1.0	0.2335	0.3531	0.2618
1.0	1.5	0.2260	0.2464	0.2351
1.0	2.0	0.2253	0.2357	0.2302
1.0	4.0	0.2251	0.2275	0.2263
1.0	8.0	0.2251	0.2257	0.2254
3.0	1.0	0.8716	1.7222	0.8960
3.0	2.0	0.8587	0.9128	0.8636
3.0	4.0	0.8586	0.8707	0.8598

Table 3.4 – Convergence of WKB approximations for fermion-loop corrections to the kink soliton. $E_{\rm WKB}$ is the fermion-loop energy calculated using the WKB correction with the given value of $\bar{\Lambda}$, $E_{\rm ND}$ is the same calculation ignoring the derivative terms in the WKB formula, and $E_{\rm BF}$ is the result of a brute-force calculation up to maximum energy $\bar{\Lambda}$.

$G/\sqrt{2}$	$E_{\rm exact}/{\rm m}$	$E_{\rm WKB}/m$	$E_{\rm LDA}/m$	$(M-\omega_{\rm bs})/m$
1.0	0.2251	0.2335	0.060	-
1.5	0.3474	0.3590	0.118	0.0607
2.0	0.4921	0.5046	0.210	0.1895
2.5	0.6621	0.6749	0.375	0.0357
				0.3536
3.0	0.8586	0.8716	0.473	0.1214
				0.5402

Table 3.5 – Fermion-loop corrections to the kink soliton for various coupling constants. Here $E_{\rm exact}$ is the exact fermion-loop energy, $E_{\rm WKB}$ is the WKB energy computed with $\bar{\Lambda}=0$, E_{LDA} is the energy computed with the local density approximation, and $m-\omega_{\rm bl}$ is the binding energy of the various bound states in units of m.

The results of performing WKB calculations for various values of $\bar{\Lambda}$ are shown in Table 3.4. The behavior is similar to the boson-loop corrections, with the WKB approximation converging very rapidly compared to the "brute-force" calculation, where the brute-force method is as described in the previous section and involves the explicit evaluation of Eq. (3.76). We also show the results of a WKB calculation in which the derivative terms in the expression for the WKB phase shift are ignored. This can be done since at large energies the WKB phase shift is

$$\delta_{\rm WKB}(\omega)=\int_{-\infty}^{\infty}dx\frac{1}{2}[M^2-g^2\phi(x)^2]\frac{1}{\omega}+\mathcal{O}(\frac{1}{\omega^3}), \tag{3.88}$$

which has no explicit dependence on $\partial\phi/\partial x$. The results of this type of calculation are also shown in Table 3.4, where this calculation is also seen to give an improvement over the brute-force technique, although it does not perform as well as the full WKB calculation.

Table 3.5 compares the exact fermion-loop energy, calculated using the WKB method with large $\bar{\Lambda}$(a value of 4m is necessary to get the displayed precision), with the values obtained using the WKB method with $\bar{\Lambda} = 0$ and the local density approximation. Some of these energies have also been calculated by [14] and our results agree. Note that the local density approximation to the fermion-loop energy for the kink soliton exists as opposed to the the situation for the boson-loop energy. The derivative corrections, however, cannot be used since they involve powers of the inverse effective mass and give a divergent contribution to the energy near $x = 0$. The local density approximation is seen to be a bad approximation for the fermion-loop energy, although it gets slightly better as the coupling constant increases. The WKB calculation that treats the bound states exactly and the continuum locally gives a much better approximation to the true energy, typically accurate to a few percent.

We now consider symmetric scalar fields. The formulas used for antisymmetric scalar fields do not work for symmetric scalar fields because F and G no longer have good parities. Fortunately, the linear combinations

$$\begin{aligned} U =& \frac{1}{\sqrt{2}}(F+G) \\ V =& \frac{1}{\sqrt{2}}(F-G) \end{aligned} \tag{3.89}$$

obey the equations

$$\begin{aligned} \frac{\partial U}{\partial x} =& g\phi V - \omega V \\ \frac{\partial V}{\partial x} =& g\phi U + \omega U \end{aligned} \tag{3.90}$$

that show that an even U corresponds to an odd V and vice-versa. Hence, we can use the results of the previous section by applying periodic boundary conditions to U and V, leading to the result that

$$\begin{aligned} \delta_s(\omega) =& \frac{1}{2}\Big(\delta_U^o(\omega) + \delta_V^0(\omega)\Big) \\ & \frac{1}{2}\Big(\delta_U(\omega) + \delta_V(\omega)\Big) \end{aligned} \tag{3.91}$$

is the phase shift that determines the density of states of the continuum. Here δ_U and δ_V are defined in the usual way to be

$$\begin{aligned}\delta_U =&\frac{1}{2}(\delta_U^e + \delta_U^o)\\ \delta_V =&\frac{1}{2}(\delta_V^e + \delta_V^o).\end{aligned} \tag{3.92}$$

Note that Equation (3.90) will not in general have a $\omega = 0$ state. Assuming that it does not implies

$$\delta(M) = N\pi \tag{3.93}$$

that implies the fermion-loop energy for a symmetric scalar field is

$$E_{\text{fl}} = \sum_{-m<\omega_i<0} (\omega_i + M) + + \lim_{\Lambda\to\infty} \left[\frac{1}{\pi}\int_m^\Lambda \delta_s(\omega)d\omega + E_{\text{ct}}(\Lambda)\right]. \tag{3.94}$$

In order to apply the WKB approximation, we need to find second-order equations that U and V obey. Equation (3.90) implies

$$\begin{aligned}\frac{\partial}{\partial x}\frac{1}{-\omega + g\phi}\frac{\partial U}{\partial x} =&g\phi U + \omega U\\ \frac{\partial}{\partial x}\frac{1}{\omega + g\phi}\frac{\partial V}{\partial x} =&g\phi V - \omega v.\end{aligned} \tag{3.95}$$

These equations can be put into the Schrödinger form by making the substitutions

$$\begin{aligned}u =&\sqrt{\omega - g\phi}U\\ v =&\sqrt{\omega + g\phi}V\end{aligned} \tag{3.96}$$

that imply

$$\begin{aligned}[-\nabla^2 + k_u^2(x)]u(x) =&0\\ [-\nabla^2 + k_v^2(x)]v(x) =&0\end{aligned} \tag{3.97}$$

where

$$\begin{aligned} k_u^2 =& \omega^2 - g^2\phi^2 - \frac{3}{4}\frac{(g\phi')^2}{(\omega - g\phi)^2} - \frac{1}{2}\frac{g\phi''}{(\omega - g\phi)} \\ k_v^2 =& \omega^2 - g^2\phi^2 - \frac{3}{4}\frac{(g\phi')^2}{(\omega + g\phi)^2} + \frac{1}{2}\frac{g\phi''}{(\omega + g\phi)}. \end{aligned} \tag{3.98}$$

The resulting WKB phase shift is

$$\delta_{\mathrm{WKB}}(\omega) = \frac{1}{2}\int_{-\infty}^{\infty} dx\, k_u^2(\omega, x) + k_v^2(\omega, x). \tag{3.99}$$

Observe that Equation (3.98) has a non-trivial energy dependence. In particular, the potential for u is large for ω near M so that frequently this WKB approximation cannot be used at low energies. At high energies it can be applied; in particular, it has the correct high-energy behavior

$$\delta_{\mathrm{WKB}}(\omega) = \frac{1}{\omega}\int_{-\infty}^{\infty} g^2\phi^2 + \mathcal{O}(\frac{1}{\omega^3}) \tag{3.100}$$

to cancel the counterterm.

Table 3.6 displays some results for the fermion-loop energy to the symmetric potential

$$\phi(x) = 1 - \frac{\phi_b}{1 + \exp(\frac{x^2 - R^2}{T^2})} \tag{3.101}$$

for which $M = 1$. The lowest values of $\bar{\Lambda}$ given in the table correspond to the smallest values for which the WKB approximation, as we have formulated it, can be used. Once it is valid to use it, we obtain results comparable to all our previous results. In particular, when there is one isolated bound state, the LDA becomes worse and the WKB becomes better.

ϕ_b	R	T	$\bar{\Lambda}$	$E_{\rm WKB}/m$	$1-\omega_{\rm bs}/M$	$E_{\rm LDA}$
0.2	1	0.5	1.48	0.0078	0.0483	0.0099
			2.00	0.0105		
			3.00	0.0110		
			6.00	0.0110		
0.4	1	0.5	1.61	0.0350	0.1408	0.0367
			2.00	0.0402		
			3.00	0.0418		
			6.00	0.0418		

Table 3.6 – Fermion-loop corrections for symmetric background fields. The first three columns are the parameters that describe the background field given by Eq. (3.101), $E_{\rm WKB}$ is the fermion-loop energy calculated using the WKB method for states with energy above $\bar{\Lambda}$, $\omega_{\rm bs}$ is the energy of the bound state , and $E_{\rm LDA}$ is the fermion-loop energy calculated via the local density approximation.

Now consider fermions with mass M coupled to a vector field. If only the time component of the vector field is non-zero, then the Dirac equation can be written as

$$[i\gamma^\mu\partial_\mu - M - V(x)\gamma^0]\psi(x,t) = 0. \tag{3.102}$$

Defining the upper and lower components via $\psi(x,t) = \begin{pmatrix} iF \\ G \end{pmatrix}\exp(-iEt)$ allows us to write the Dirac equation as

$$\begin{pmatrix} \frac{d}{dx} - M & -E + V(x) \\ -E + V(x) & -\frac{d}{dx} - M \end{pmatrix}\begin{pmatrix} F \\ G \end{pmatrix} = 0. \tag{3.103}$$

Observe that the energy spectrum is not symmetric about zero energy as in the case of the scalar field since particles and antiparticles feel an opposite field strength for vector fields.

First consider the vacuum energy in the presence of a uniform field V. The energy spectra is

$$E = V \pm \sqrt{p^2 + M^2} \tag{3.104}$$

where p is the momentum of the state. Both positive and negative energy states have been shifted up by the same amount of energy. A uniform vector field is simply equivalent to redefining the zero of energy. The bare vacuum shift is

$$\begin{aligned} \sum_{\omega_i^0<0} \omega_i - \omega_i^0 &= \sum_{\omega_i^0<0} V \\ &= V\langle 0|\psi^\dagger\psi|0\rangle. \end{aligned} \tag{3.105}$$

Since a uniform shift in the energy scale has no physical effect, it is clear we need a counterterm contribution $-V\langle\psi^\dagger\psi\rangle$. A simpler way to get rid of the effect of the uniform energy shift is to realize that the fermion-vacuum-energy shift can be formally written in three equivalent ways,

$$\begin{aligned} E_{\text{vacuum}} &= \sum_{\omega_i^0<0} \omega_i - \omega_i^0 \\ &= -\sum_{\omega_i^0>0} \omega_i - \omega_i^0 \\ &= \frac{1}{2}\Big[\sum_{\omega_i^0<0} \omega_i - \omega_i^0 - \sum_{\omega_i^0>0} \omega_i - \omega_i^0\Big]. \end{aligned} \tag{3.106}$$

The second equality follows by deforming the integration contour in the energy plane (see Figure 2.3) to circle the positive-energy poles instead of the negative-energy poles. The sign change is due to the difference in the orientation of the two contours. The third equality is the average of the first two. The third equality has the advantage that the effect of the uniform energy shift is automatically cancelled and is the appropriate formulation to use for a vector field [5] .

The conclusion is that $E_{\text{vacuum}} = 0$ for a uniform vector field. This means that the local density approximation for a spatially varying vector field is that there is no vacuum energy generated. We now show that the local expressions generated by the WKB approximation are capable of generating useful physics, where we assume that the spatially varying vector field vanishes at infinity. In terms of phase shifts, the vacuum energy can be written

$$E_{\text{vacuum}} = \frac{1}{2}\Big(\sum_{|\omega_i|<m} (\text{sgn}(\omega_i^0)\omega_i + M) + \frac{1}{\pi}\int_M^\infty d\omega \, [\delta(\omega) + \delta(-\omega)]\Big). \tag{3.107}$$

For simplicity, we now work out the WKB approximation for the case $m = 0$, although all that we say is equally applicable for the massive case. In addition, any needed counterterms need to be added in. In $1+1$ dimensions no counterterms are needed for the vector field. Equation (3.103) implies that both F and G obey the same second-order equation; that is,

$$\frac{d}{dx}\Big(\frac{1}{-\omega + V(x)}\frac{d}{dx}G\Big) + (-\omega + V(x))G = 0. \tag{3.108}$$

Making our standard substitution

$$G = \sqrt{\omega - V(x)}g, \tag{3.109}$$

we obtain the equation

$$g''(x) + k^2(\omega, x)g = 0, \tag{3.110}$$

where

$$k^2(\omega, x) = (\omega - V(x))^2 - \frac{1}{2}\frac{V''(x)}{\omega - V(x)} - \frac{3}{4}\left(\frac{V'(x)}{\omega - V(x)}\right)^2. \tag{3.111}$$

The WKB approximation for the phase shift follows as

$$\delta(\omega) + \delta(-\omega) = \int_{-\infty}^{\infty} dx\,[k(\omega, x) + k(-\omega, x)]. \tag{3.112}$$

Observe that k^2 involves derivatives of V as did the symmetric scalar field. This is vital for the WKB approximation to do a good job describing the perturbation of the vacuum by the vector field.

The primary difference between the vector and the scalar field is that the vector field couples to the vector density that is a conserved quantity, while the scalar field couples to the scalar density that is not a conserved quantity. Hence, in a uniform system it is possible for the vacuum to acquire a net scalar density. Hence, the LDA gives a non-vanishing result and good approximations that depend only on the magnitude of the scalar field can be found. Since the vector density is conserved, a uniform system must have zero fermion number density in the vacuum. In finte systems, however, local fermion number densities can be set up as long as they integrate to zero. This is the essential physics involved with vector fields, and the LDA and any other approximation that involves only the magnitude of the vector field cannot capture this physics. To see explicitly that the WKB does allow fluctuating fermion-density effects, consider the high energy behavior of the phase shifts,

$$\frac{1}{2}\Big(\delta(\omega) + \delta(-\omega)\Big) = -\frac{1}{8\pi}\int_{-\infty}^{\infty} dx\,\frac{1}{\omega^3}(V'(x))^2 + \mathcal{O}(\omega^{-4}). \tag{3.113}$$

This gives a contribution to the vacuum energy proportional to $[V'(x)]^2$. When the total energy is minimized, this will generate a contribution to the fermion density that is

$$\rho_{\text{vacuum}} \sim \frac{d}{dx}\frac{\partial E}{\partial V'(x)} \sim V''(x). \tag{3.114}$$

This induced density integrates to zero since it is a total derivative. Thus, the WKB method is capable of working well for vector fields.

3.4 Self-Consistent Fermion-Loop Calculations

Having calculated the fermion-loop energy, we now need to adjust the meson fields to minimize this energy. Physically, the changes in the meson fields are due to the polarization of the vacuum by the fields, which induces non-vanishing densities in the vacuum, which in turn act as sources for the meson fields.

At the one-loop level the energy of fermions coupled to a scalar field via the Lagrangian (3.58) is

$$E = \int dx \frac{1}{2}(\nabla\phi)^2 + V(\phi) + E_{\text{fl}}(\phi). \tag{3.115}$$

The scalar field is determined by

$$\frac{\delta E}{\delta \phi} = 0. \tag{3.116}$$

In Section (2.2) it was shown that this implies the equation

$$-\nabla^2\phi + V'(\phi) = g\rho_s = g(\rho_s^{\text{valence}} + \rho_s^{\text{vacuum}}) \tag{3.117}$$

where

$$\rho_s^{\text{valence}} = \sum_{0<\omega_i<\mu_f} \bar{\psi}_i\psi_i \tag{3.118}$$

and

$$\rho_s^{\text{vacuum}} = \lim_{\Lambda\to\infty} \sum_{-\Lambda<\omega_i^0<0} \bar{\psi}_i\psi_i + \frac{1}{g}\frac{\delta E_{\text{ct}}(\Lambda,\phi)}{\delta\phi(x)}. \tag{3.119}$$

In $1+1$ dimensions the value of the counterterm is given by Eq. (3.75), implying

$$\frac{1}{g}\frac{\delta E_{\text{ct}}(\Lambda,\phi)}{\delta\phi(x)} = \frac{1}{2\pi}\left(\frac{M\phi}{\phi_v}\right)\log\left(\frac{4\Lambda^2}{M^2}\right). \tag{3.120}$$

This can be readily interpreted by realizing that (see section 2.3)

$$\begin{aligned}\sum_{-\Lambda<\omega_i<0} \bar{\psi}^0\psi^0 &= -\int_{-\Lambda_p}^{\Lambda_p} \frac{dk}{2\pi}\frac{M}{\sqrt{k^2+M^2}} \\ &= -\frac{1}{2\pi}M\log\left(\frac{4\Lambda^2}{M^2}\right)+\mathcal{O}(\Lambda^{-1}),\end{aligned} \tag{3.121}$$

which implies that the vacuum scalar density can be written as

$$\rho_s^{\text{vacuum}} = \lim_{\Lambda\to\infty}\sum_{-\Lambda<\omega_i^0<0} \bar{\psi}_i\psi_i - \frac{\phi}{\phi_v}\bar{\psi}_i^0\psi_i^0. \tag{3.122}$$

As a check, we see that the scalar density vanishes in a vacuum as it should.

We now consider using the WKB method in a variational calculation, where we use exact solutions for energies below $\tilde{\Lambda}$ and the WKB method for higher energies. A direct application of the phase-shift energy formula is inconvenient since this would require a calculation of the variation of the exact phase shift with respect to local variations in the scalar field. Instead, we reformulate the WKB method in terms of exact wavefunctions at low energies and WKB phase shifts at high energies. Using

the results of Section (3.1), we can write

$$
\begin{aligned}
E_{\rm fl}(\phi(x)) = & \sum_{-\tilde{\Lambda}<\omega_i<0} \omega_i \\
& + \lim_{\Lambda\to\infty}\Big[- \int_{\tilde{\Lambda}}^{\bar{\Lambda}} \omega n(\omega) d\omega - \int_{M}^{\Lambda} \omega n^0(\omega) d\omega + E_{\rm ct}(\Lambda)\Big] \\
= & \sum_{-\tilde{\Lambda}<\omega_i<0} \omega_i + \int_{M}^{\tilde{\Lambda}} \omega n^0(\omega) d\omega \\
& + \lim_{\Lambda\to\infty}\Big[- \int_{\tilde{\Lambda}}^{\bar{\Lambda}} \omega n(\omega) d\omega - \int_{\tilde{\Lambda}}^{\Lambda} \omega n^0(\omega) d\omega + E_{\rm ct}(\Lambda)\Big] \\
= & \sum_{-\tilde{\Lambda}<\omega_i<0} \omega_i + \int_{M}^{\tilde{\Lambda}} \omega n^0(\omega) d\omega \\
& + \lim_{\Lambda\to\infty}\Big[\frac{1}{\pi}\tilde{\Lambda}\delta(\tilde{\Lambda}) + \frac{1}{\pi}\int_{\tilde{\Lambda}}^{\Lambda} \delta(\omega) d\omega + E_{\rm ct}(\Lambda)\Big] \\
= & \sum_{-\tilde{\Lambda}<\omega_i<0} \omega_i + \int_{M}^{\tilde{\Lambda}} \omega n^0(\omega) d\omega \\
& + \lim_{\Lambda\to\infty}\Big[\frac{1}{\pi}\tilde{\Lambda}\delta(\tilde{\Lambda}) + \frac{1}{\pi}\int_{-\infty}^{\infty} dx\, \alpha_f(\phi(x), \partial_x\phi, \tilde{\Lambda})\Big],
\end{aligned}
\tag{3.123}
$$

where α_f is defined in Eq. (3.83). If $\tilde{\Lambda} = M$, then we can evaluate $\tilde{\Lambda}\delta(\tilde{\Lambda})$ exactly in terms of the number of bound states. Otherwise, we approximate this, using the WKB approximation,

$$
\begin{aligned}
\frac{1}{\pi}\tilde{\Lambda}\delta_{\rm WKB}(\tilde{\Lambda}) = & \frac{\tilde{\Lambda}}{2\pi}\int_{-\infty}^{\infty} dx \Big[\sqrt{\tilde{\Lambda} - g^2\phi^2 + g\frac{\partial\phi}{\partial x}} \\
& + \sqrt{\tilde{\Lambda} - g^2\phi^2 - g\frac{\partial\phi}{\partial x}} - 2\sqrt{\tilde{\Lambda}^2 - M^2}\Big] \\
\equiv & \int_{-\infty}^{\infty} dx\, \beta(\tilde{\Lambda}, \phi(x)).
\end{aligned}
\tag{3.124}
$$

The scalar density induced in the vacuum is calculated by varying Eq. (3.123) with respect to $\phi(x)$, resulting in

$$\begin{aligned} g\rho_s(x) =& \frac{\delta E_{\rm fl}}{\delta\phi(x)} \\ =& g\sum_{-\tilde{\Lambda}<\omega_i<0} \bar{\psi}_i\psi_i + \frac{\partial}{\partial\phi}[\beta_f(\tilde{\Lambda})+\alpha_f(\tilde{\Lambda})] - \frac{d}{dx}\Big(\frac{\partial}{\partial(\partial_x\phi)}[\beta_f(\tilde{\Lambda})+\alpha_f(\tilde{\Lambda})]\Big), \end{aligned} \tag{3.125}$$

where we have used the fact that our WKB expressions depend explicitly on $\phi(x)$ and $d\phi(x)/dx$.

We now demonstrate this method by performing calculations for the kink soliton coupled to a single fermion field, as described in Section 3.3. Recall that the Hamiltonian for the kink-fermion system is

$$H = \int_{-\infty}^{\infty} dx\, \frac{1}{2}(\nabla\phi)^2 - \frac{1}{2}m^2\phi^2 + \frac{1}{4}\lambda\phi^4 + \psi_i^\dagger(i\gamma^0\gamma^1\frac{d}{dx} + g\gamma^0\phi)\psi_i. \tag{3.126}$$

Note that ϕ is dimensionless,ψ has dimension [mass]$^{1/2}$, m and g have dimension [mass], and λ had dimension [mass]^2. By performing the rescalings $x \to mx$, $\phi \to \sqrt{\lambda}\phi/m$, and $\psi \to \psi/\sqrt{m}$, the Hamiltonian can be written

$$\frac{H}{m} = \int_{-\infty}^{\infty} dx\, \frac{m^2}{\lambda}\Big[\frac{1}{2}(\nabla\phi)^2 - \frac{1}{2}\phi^2 + \frac{1}{4}\phi^4\Big] + \psi_i^\dagger(i\gamma^0\gamma^1\frac{d}{dx} + \frac{g}{\sqrt{\lambda}}\gamma^0\phi)\psi_i. \tag{3.127}$$

The system is characterized by two dimensionless variables. The first ,m^2/λ, controls the relative magnitude of the scalar-field energy and the fermion-loop energy, while the second, $G = g/\sqrt{\lambda}$, determines how strongly the fermions couple to the scalar field.

The variation of the fermion-loop energy with G was studied in the previous section. It was found that using the WKB approximation in the continuum provides

a good approximation of the fermion-loop energy. In this approximation, the fermion-loop energy is given specifically by Eq. (3.123) with $\tilde{\Lambda} = M$ and

$$\begin{aligned}\alpha_f(\phi(x)) =& \frac{1}{4}\sum_{i=(+,-)}\Big[\frac{1}{2}(M^2-(M^i)^2) - M\sqrt{M^2-(M^i)^2} \\ &+ (M^i)^2\log\Big(\frac{M+\sqrt{M^2-(M^i)^2}}{M}\Big)\Big],\end{aligned} \tag{3.128}$$

where

$$(M^{\pm})^2 = g^2\phi^2 \pm g\frac{\partial\phi}{\partial x}. \tag{3.129}$$

A typical example of a scalar density calcuated via Eq. (3.125) is shown in Fig. 3.7. In this case there is one bound state and at small distances it is the dominant contribution to the scalar density. At large distances the continuum is the dominant contribution. Observe that the induced scalar density in the vacuum persists well beyond the "radius" of the soliton.

We achieve self-consistency by solving Eq. (3.117), which for the kink soliton is

$$-\nabla^2\phi - \phi + \phi^3 = -\frac{G\lambda}{m^2}\rho_s(G,\phi), \tag{3.130}$$

subject to the boundary conditions $\phi(0) = 0$ and $\phi(\infty) = 1$. In order to solve this non-linear equation, we define $\eta(x)$ by

$$\phi(x) = \phi_k(x) + \eta(x), \tag{3.131}$$

where $\phi_k(x)$ is the classical kink soliton solution. In terms of η Eq. (3.130) becomes

$$-\nabla^2\eta(x) + (3\phi_k^2 - 1)\eta(x) = -\frac{G\lambda}{m^2}\rho_s(G,\phi) - [\eta(x)]^3 - 3\phi_k(x)[\eta(x)]^2. \tag{3.132}$$

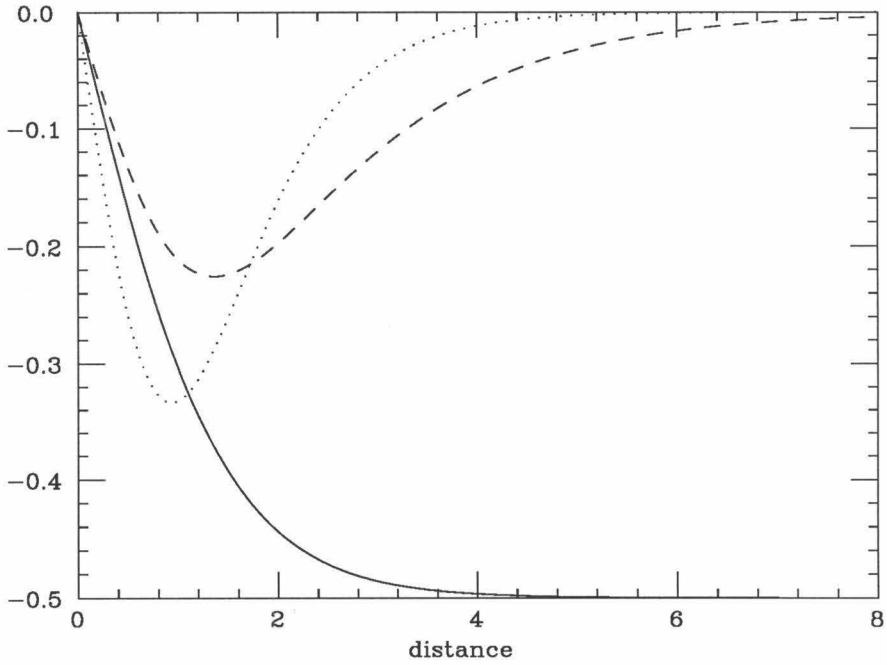

Figure 3.7 – Fermion scalar density induced in the vacuum by the kink soliton ($G = \sqrt{2}$). The dashed line is the scalar density due to the continuum states and the dotted line is the scalar density due to the bound state. For reference, the solid line shows $-0.5\phi_k(x)$.

This equation is of a form that can be conveniently solved by iteration. Numerical details are described in Appendix D.

Table 3.7 presents results for

$$\frac{m^2}{\lambda} = 4$$

and various values of G corresponding to a range in which the fermion-loop contributes up to $\sim 20\%$ of the mass of the soliton.

Since the fermion-loop energy is positive, the soliton minimizes its energy by decreasing the fermion-loop energy. The point of equilibrium is where the decrease in the

$G/\sqrt{2}$		$E_{\rm sol}/m$	$E_{\rm fl}/m$	E_b/m	$E_{\rm total}$
1.0	a	3.771	0.233	-	4.005
	b	3.772	0.232	-	4.004
1.5	a	3.771	0.359	0.061	4.130
	b	3.772	0.355	0.056	4.127
2.0	a	3.771	0.505	0.189	4.276
	b	3.783	0.479	0.185	4.262
2.5	a	3.771	0.675	0.354	4.446
	b	3.791	0.628	0.328	4.418

Table 3.7 – Effect of fermion vacuum on the kink soliton. $E_{\rm sol}$ is the classical energy of the soliton, $E_{\rm fl}$ is the fermion-loop energy, $E_{\rm b}$ is the binding energy of the most bound fermion level, and $E_{\rm total}$ is the total energy at the one-loop level. Row a gives the values of these quantities for the classical kink soliton and row b gives their values after the one-loop energy is minimized.

fermion-loop energy is balanced by the increase in the classical boson energy. The classical boson energy must increase since the unperturbed solution minimizes the classical energy. Table 3.7 displays the classical boson energy, the fermion-loop energy, and the total energy before and after mimimization. The effect of self-consistency increases with G. In order to decrease the fermion-loop energy, the soliton needs to contract. An effect of this is shown in Table 3.7, where the binding energies of the bound states are observed to increase. This is shown explicitly in Figure 3.8 where the slope of the soliton at the origin is plotted as a function of G. The slope increases

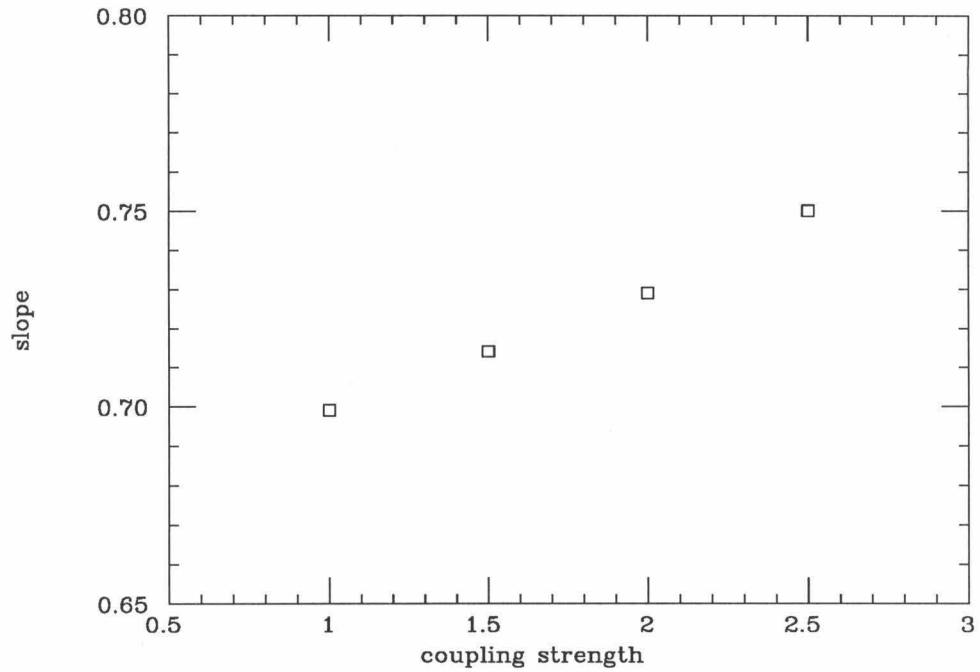

Figure 3.8 – Slope of the kink soliton at $x = 0$ as a function of the fermion coupling strength, $G/\sqrt{2}$. The soliton contracts as the coupling is increased.

with G. Physically, we can think of this as the vacuum exerting a negative "bag" pressure on the soliton.

We now study solitons with fermion number 1. These are generated by occupying the lowest-energy, positive energy state so that the fermion scalar density becomes

$$\rho_s(x) = \rho_s^{\text{vacuum}}(x) + \bar{\psi}_+(x)\psi_+(x), \tag{3.133}$$

where ψ_+ is the lowest-energy, positive-energy wavefunction. Table 3.8 displays results for fermion number 1 both including and excluding the vacuum.

First consider the situation in which the vacuum is ignored. The valence fermions need to become more bound in order to minimize the soliton's energy, an effect that

$G/\sqrt{2}$		$E_{\rm sol}/m$	$E_{\rm fl}/m$	E_b/m	$E^{(1)}_{\rm total}/m$	$E^{(2)}_{\rm total}/m$
1.5	a	3.771	0.359	0.061	4.771	5.130
	b	3.781	0.364	0.080	4.762	-
	c	3.778	0.359	0.076	-	5.122
2.0	a	3.771	0.505	0.189	4.996	5.500
	b	3.795	0.512	0.236	4.973	-
	c	3.805	0.482	0.232	-	5.469
2.5	a	3.771	0.675	0.354	5.185	5.860
	b	3.812	0.718	0.434	5.146	-
	c	3.811	0.643	0.399	-	5.823

Table 3.8 – Effect of valence fermions on the kink soliton. $E_{\rm sol}$ is the classical energy of the soliton, $E_{\rm fl}$ is the fermion-loop energy, $E_{\rm b}$ is the binding energy of the most bound fermion level, $E^{(1)}_{\rm total}$ is the sum of the valence and classical energies, and $E^{(2)}_{\rm total}$ is the full one-loop energy. Row a gives the values of these quantities for the classical kink soliton, row b gives their values after minimizing the energy, including only the valence fermions, and row c gives their values after the full one-loop energy is minimized.

is seen clearly in Table 3.8. Hence, valence fermions act to expand the soliton. This can be thought of as a positive outward pressure due to the Heisenberg uncertainty principle. This expansion is correlated with an increase in the fermion vacuum energy.

When the vacuum is turned on, there is a conflict between the desire to lower the valence energy and the desire to lower the vacuum energy. The presence of the vacuum causes the binding energy and fermion vacuum energy to be significantly reduced. As the coupling constant becomes larger, the vacuum begins to dominate over the valence particles.

In the conclusion of this section, we have presented some sample calculations that show how the local WKB method can be effectively used to study the self-consistent effect of the vacuum on a soliton.

Chapter 4
The WKB Method in 3+1 Dimensions

In this chapter, we extend the WKB method to spherically symmetric systems in three spatial dimensions. This is done by using the WKB approximation in each partial wave channel.

4.1 Boson-Loops in Three Spatial Dimensions

The formalism for the boson-loop energy is the same in three dimensions as in one. The eigenfrequencies for the boson modes in three spatial dimensions are determined by

$$[-\nabla^2 + M^2(r) - \omega_n^2]\eta_n = 0, \tag{4.1}$$

where $M^2(r) = V''(\phi)$, and we assume that ϕ is spherically symmetric. In this case, we can factor out the angular dependence of η by writing

$$\eta_n = \frac{1}{r} u_{nl}(r) Y_{lm}(\theta, \phi), \tag{4.2}$$

where the radial wavefunction u obeys

$$\Big[-\frac{d^2}{dr^2} + \frac{l(l+1)}{r^2} + M^2(r) - \omega_{nl}^2 \Big] u_{nl}(r) = 0, \tag{4.3}$$

and the Y_{lm} are the spherical harmonics corresponding to a state of total angular momentum l and z component m. Observe that the radial wavefunction satisfies the

boundary condition $u_n(0) = 0$. If $M^2(r) = M^2$, then the solutions of the above equation are simply spherical bessel functions [19],

$$u^0_{kl} = \sqrt{2} k_n r j_l(k_n r), \tag{4.4}$$

that have the asymptotic behavior

$$u^0_n(r) \to \sqrt{2} \sin(k_n r - \frac{1}{2} l\pi)\,, \; r \to \infty, \tag{4.5}$$

where $k_n^2 = \omega_n^2 - M^2$. These are normalized so that

$$\int_0^\infty dr\, u_{k'l}(k'r) u_{kl}(kr) = \pi \delta(k' - k). \tag{4.6}$$

For reference, the spherical Bessel functions are given analytically by

$$j_l(z) = (-1)^l z^l \Big(\frac{1}{z}\frac{d}{dz}\Big)^l \frac{\sin(z)}{z}. \tag{4.7}$$

If $M^2(r)$ is spatially varying with $M^2(r) \to M^2$ as $r \to \infty$, then the asymptotic behavior will be

$$u_n(r) \to \sin(kr - \frac{1}{2} l\pi + \delta_l(k)), r \to \infty. \tag{4.8}$$

This defines the phase shift in each angular momentum channel. Putting the system in a box of radius L and imposing the boundary condition

$$u_{nl}(L) = 0 \tag{4.9}$$

implies that

$$k_n L - \frac{1}{2} l\pi + \delta_l(k_n) = n\pi. \tag{4.10}$$

Following the arguments of Chapter 3, this implies

$$n_l(\omega) - n_l^0(\omega) = \frac{1}{\pi}\frac{d\delta_l(\omega)}{d\omega}, \tag{4.11}$$

where $(2l+1)n_l(\omega)$ is the density of states with angular momentum l.

Using this relation and following the methods of Chapter 3 we find that the boson-loop energy can be written as

$$\begin{aligned} E_{\rm bl} =& \frac{1}{2}\sum_{\omega_{nl}^2<M^2}(2l+1)(\omega_{nl}-M) \\ &+ \lim_{\Lambda\to\infty}\Big[-\frac{1}{2\pi}\sum_l(2l+1)\int_M^\Lambda \delta_l(\omega)d\omega + E_{\rm ct}(\Lambda)\Big]. \end{aligned} \tag{4.12}$$

It is convenient to define the boson-loop energy in each angular momentum channel as

$$E_{\rm bl} = \sum_l (2l+1)E_{\rm bl}^l \tag{4.13}$$

and to divide the counterterm energy between each angular momentum channel as

$$E_{\rm ct}(\Lambda) = \sum_l (2l+1)E_{\rm ct}^l(\Lambda), \tag{4.14}$$

which allows us to write

$$E_{\rm bl}^l = \frac{1}{2}\sum_{\omega_n^2<M^2}(\omega_{nl}-M) + \lim_{\Lambda\to\infty}\Big[-\frac{1}{2\pi}\int_M^\Lambda \delta_l(\omega)d\omega + E_{\rm ct}^l(\Lambda)\Big]. \tag{4.15}$$

A straightforward application of the WKB approximation to Equation (4.3) yields the expression [20]

$$\delta_l^{\rm WKB}(\omega) = \int_{a(\omega)}^\infty dr\sqrt{\omega^2 - M^2(r) - \frac{l(l+1)}{r^2}} - \int_{a_0(\omega)}^\infty dr\sqrt{\omega^2 - M^2 - \frac{l(l+1)}{r^2}}, \tag{4.16}$$

where a and a_0 are the classical turning points given by

$$\omega^2 - M^2(a) - \frac{l(l+1)}{a^2} = 0 \tag{4.17}$$

and

$$\omega^2 - M^2 - \frac{l(l+1)}{a_0^2} = 0. \tag{4.18}$$

The one-loop energy is calculated from the energy integral of the phase shift that can be written as

$$\begin{aligned}\int_M^\Lambda \delta_l^{\mathrm{WKB}}(\omega)\, d\omega = \int_0^\infty dr \Big[\int_{\omega_b(r)}^\Lambda d\omega \sqrt{\omega^2 - M^2(r) - \frac{l(l+1)}{r^2}} \\ - \int_{\omega_b^0(r)}^\Lambda \sqrt{\omega^2 - M^2 - \frac{l(l+1)}{r^2}} \Big],\end{aligned} \tag{4.19}$$

where

$$\omega_b(r) = \sqrt{M^2(r) + \frac{l(l+1)}{r^2}} \tag{4.20}$$

and

$$\omega_b^0(r) = \sqrt{M^2 + \frac{l(l+1)}{r^2}}. \tag{4.21}$$

Observe that the high-energy behavior of the phase shift is independent of angular momentum,

$$\delta_l^{\mathrm{WKB}}(\omega) = \int_0^\infty dr\, \frac{1}{2}\Big(M^2 - M^2(r)\Big)\frac{1}{\omega} + \mathcal{O}(\frac{1}{\omega^3}), \tag{4.22}$$

implying that the energy in each angular momentum channel diverges logarithmically,

$$E_{bl} = -\frac{1}{4\pi}\sum_l (2l+1)\log\Big(\frac{\Lambda}{M}\Big)\int_0^\infty dr\, \Big(M^2 - M^2(r)\Big) + \mathcal{O}(\Lambda^0). \tag{4.23}$$

Although the energy in each partial wave channel diverges only logarithmically, the total energy diverges at a larger rate because of the angular momentum summation. Because of this, finite contributions to the energy in each partial wave channel can lead to divergent contributions to the total energy. In order to cancel these divergences, we perform a partial wave decomposition of the counterterms.

In $3+1$ dimensions, the divergent one-loop graphs are the graphs with one and two external vertices (see Appendix A) leading to quadratic and logarithmic divergences, respectively. The general form of the contribution of one of these diagrams to the total energy is

$$\int_{-\infty}^{\infty} \frac{d\omega}{2\pi} \int \frac{d^3p}{(2\pi)^3} f(\omega^2 - p^2 - M^2) \int d^3x\, h(x) = \int_{-\infty}^{\infty} d\omega\, \mathrm{Tr}'(fh), \tag{4.24}$$

where f is some power of the propagator, h is some polynomial in ϕ and its derivatives, and Tr' denotes a trace over spatial variables. The partial wave decomposition is achieved by performing the trace with respect to the eigenstates of Eq. (3.1) with $M^2(r) = M^2$ that we denote $|nlm\rangle$,

$$\begin{aligned} \mathrm{Tr}'(hf) &= \sum_{nlm} \sum_{n'l'm'} \langle nlm|f(\omega^2 + \nabla^2 - M^2)|n'l'm'\rangle\langle n'l'm'|h(r)|nlm\rangle \\ &= \sum_{nlm} f(\omega^2 - \omega_{nl}^2)\langle nlm|h(r)|nlm\rangle \\ &= \sum_{l} (2l+1) \int_0^{\infty} \frac{dk}{\pi} \Big[f(\omega^2 - k^2 - M^2) \int_0^{\infty} dr\, |u_{kl}^0(r)|^2 h(r) \Big]. \end{aligned} \tag{4.25}$$

From Appendix A, the counterterms are

$$E_{\mathrm{ct}} = -\frac{i}{2} \int_{-\infty}^{\infty} \frac{d\omega}{2\pi} \mathrm{Tr}' \Big(\Delta_0[M^2(x) - M^2] + \frac{1}{2}\Delta_0^2[M^2(x) - M^2]^2 \Big), \tag{4.26}$$

where

$$\Delta^0 = \frac{1}{\omega^2 + \nabla^2 - M^2 + i\epsilon}. \tag{4.27}$$

Applying our trace formula, we find

$$-\frac{i}{2}\int_{-\infty}^{\infty}\frac{d\omega}{2\pi}\,\mathrm{Tr}'\Big(\Delta_0[M^2(x)-M^2]\Big) = -\frac{i}{2}\sum_l(2l+1)\int_{-\infty}^{\infty}\frac{d\omega}{2\pi}\int_0^{\Lambda_p}\frac{dk}{\pi}$$
$$\Big[\frac{1}{\omega^2-\omega_k^2+i\epsilon}\int_0^{\infty}dr|u_{kl}(r)|^2(M^2(r)-M^2)\Big]$$

$$=\frac{-1}{4\pi}\sum_l(2l+1)\int_0^{\Lambda_p}dk$$
$$\Big[\frac{1}{\omega_k}\int_0^{\infty}dr|u_{kl}(r)|^2(M^2(r)-M^2)\Big] \tag{4.28}$$

and

$$-\frac{i}{4}\int_{-\infty}^{\infty}\frac{d\omega}{2\pi}\,\mathrm{Tr}'\Big(\Delta_0^2[M^2(x)-M^2]^2\Big) = -\frac{i}{2}\sum_l(2l+1)\int_{-\infty}^{\infty}\frac{d\omega}{2\pi}\int_0^{\Lambda_p}\frac{dk}{\pi}$$
$$\Big[\frac{1}{(\omega^2-\omega_k^2+i\epsilon)^2}\int_0^{\infty}dr|u_{kl}^0(r)|^2(M^2(r)-M^2)^2\Big] \tag{4.29}$$

$$=\frac{1}{16\pi}\sum_l(2l+1)\int_0^{\Lambda_p}dk$$
$$\Big[\frac{1}{(\omega_k)^3}\int_O^{\infty}dr|u_{kl}^0(r)|^2(M^2(r)-M^2)^2\Big].$$

Observe that the first expression that diverges quadratically with Λ diverges only logarithmically in each partial wave channel and the second expression that diverges logarithmically is finite in each partial wave channel. Combining these, we obtain our final result

$$E_{\mathrm{ct}}^l = \int_0^{\Lambda_p}dk\,\Big[-\frac{1}{4\pi}\frac{1}{\sqrt{k^2+M^2}}\int_0^{\infty}dr\,|u_{kl}^0(r)|^2(M^2(r)-M^2)\Big]$$
$$+\frac{1}{16\pi}\frac{1}{(k^2+M^2)^{3/2}}\int_0^{\infty}dr|u_{kl}^0(r)|^2(M^2(r)-M^2)^2. \tag{4.30}$$

By using the identity $\sum_l(2l+1)|j_l(x)|^2 = 1$, it is straightforward to verify that $\sum_l(2l+1)E_{\mathrm{ct}}^l$ gives the correct value for the full counterterm, verifying the correctness of Eq. 4.30.

Using the asymptotic formula, Eq. (4.8), we can express the divergent part of the counterterm as

$$-\frac{1}{4}\int_0^{\Lambda_p} dk\,\frac{1}{k}\int_0^{\infty} dr 2\sin^2(kr-\frac{l\pi}{2})(M^2(r)-M^2). \tag{4.31}$$

For large k the sine oscillates rapidly compared to variations in $M^2(x)$, and hence the square of the sine can be replaced by $1/2$, yielding

$$E^l_{\rm ct}(\Lambda) = -\frac{1}{4\pi}\log\left(\frac{\Lambda}{M}\right)\int_0^{\infty}(M^2(r)-M^2)+\mathcal{O}(\Lambda^0). \tag{4.32}$$

This exactly cancels the infinite contribution calculated using the WKB method as it must.

At this point it is interesting to discuss an alternative method of approximating the phase shifts. Since the phase shifts are related to the scattering cross sections, various scattering approximations can be used to generate approximations for the phase shift. For instance, in the Born approximation [21] the phase shift is

$$\delta_l^{\rm Born} = -k\int_0^{\infty} r^2 dr\left(M^2(r)-M^2\right)|j_l(kr)|^2. \tag{4.33}$$

Inserting this into Equation (4.15), we find that this contributes an amount

$$\begin{aligned} E_{\rm bl}^{\rm Born} =& \frac{1}{2\pi}\sum_l(2l+1)\Big[\int_0^{\infty}\frac{dk}{\sqrt{k^2+M^2}}k^2 \\ & \int_0^{\infty} dr\, r^2\left(M^2(r)-M^2\right)|j_l(kr)|^2\Big] \end{aligned} \tag{4.34}$$

to the boson-loop energy. Observe that this is exactly the divergent part of the counterterm in the $l^{\rm th}$ partial wave. Hence, the Born approximation is useless for calculating the finite part of the loop energy that we are interested in. It does,

however, give us a nice understanding of the leading divergence in the boson-loop energy as being given by the Born approximation.

We now return to the explicit calculation of the boson-loop energy. In order to evaluate the boson-loop energy explicitly we need to perform the energy integrals. The energy integral of the phase shifts can be easily performed analytically, whereas the energy integrals in the counterterms can not. Nonetheless, since we have isolated the infinite part of the counterterm integral, this part can be transferred over to the phase-shift integral and absorbed analytically. The remaining counterterm integrals are finite and easily integrated numerically. Specifically, we add Eq. (4.32) to the phase-shift integral and simultaneously subtract Eq. (4.32) from the counterterm integral, implying

$$\begin{aligned} E^l_{\rm bl} =& \frac{1}{2} \sum_{\omega^2_{nl}<M^2} (\omega_{nl} - M) - \frac{1}{2\pi} \int_M^{\bar\Lambda} \delta(\omega) d\omega \\ & - \frac{1}{2\pi} \int_0^\infty dr \Big(\alpha_l(\bar\Lambda, r) + \gamma_l(r)[M^2(r) - M^2] + \lambda_l(r)[M^2(r) - M^2]^2 \Big). \end{aligned} \tag{4.35}$$

Here, $\alpha(r)$ is the contribution generated by the phase shift,

$$\begin{aligned} \alpha(r) = \lim_{\Lambda\to\infty} \Big[& \int_{\Lambda_b(r)}^{\Lambda} d\omega \sqrt{\omega^2 - M_l^2(r)} \\ & - \int_{\Lambda_b^0(r)}^{\Lambda} d\omega \sqrt{\omega^2 - M_l^2} \\ & + \frac{1}{2} \int_M^{\Lambda} \frac{d\omega}{\sqrt{\omega^2 - M^2}} \Big(M^2(r) - M^2 \Big) \Big], \end{aligned} \tag{4.36}$$

where we have introduced the simplified notation

$$\begin{aligned} M_l(r)^2 =& M^2(r) + \frac{l(l+1)}{r^2} \\ M_l^0(r)^2 =& M^2 + \frac{l(l+1)}{r^2} \end{aligned} \tag{4.37}$$

and defined

$$\begin{aligned}\Lambda_b(r) &= \max\Big(\bar{\Lambda}, \omega_b(r)\Big) \\ \Lambda_b^0(r) &= \max\Big(\bar{\Lambda}, \omega_b^0(r)\Big).\end{aligned} \tag{4.38}$$

Performing the energy integral and taking the limit gives

$$\begin{aligned}2\alpha_l(r) =& M_l^0(r)^2 - M_l(r)^2 - \Lambda_b(r)\sqrt{\Lambda_b(r)^2 - M_l(r)^2} \\ &+ \Lambda_b^0(r)\sqrt{\Lambda_b^0(r)^2 - M_l^0(r)^2} \\ &+ M_l(r)^2 \log\Big(\frac{\Lambda_b(r) + \sqrt{\Lambda_b(r)^2 - M_l(r)^2}}{M}\Big) \\ &- M_l^0(r)^2 \log\Big(\frac{\Lambda_b(r) + \sqrt{\Lambda_b(r)^2 - M_l^0(r)^2}}{M}\Big).\end{aligned}$$

Finally, the contributions of the two counterterms $\gamma_l(r)$ and $\lambda_l(r)$ are given by

$$\begin{aligned}\gamma_l(r) =& \frac{1}{2}\int_0^\infty \frac{dk}{\sqrt{k^2+M^2}}(|u_{kl}^0(r)|^2 - \frac{1}{2}) \\ =& \int_0^\infty \frac{dk}{\sqrt{k^2+M^2}}((kr)^2|j_l^0(kr)|^2 - 1) \\ =& \int_0^\infty \frac{du}{\sqrt{u^2+(Mr)^2}}(u^2|j_l^0(u)|^2 - 1)\end{aligned} \tag{4.39}$$

and

$$\begin{aligned}\lambda_l(r) =& -\frac{1}{8}\int_0^\infty \frac{dk}{(k^2+M^2)^{3/2}}|u_{kl}^0(r)|^2 \\ =& -\frac{1}{4}\int_0^\infty \frac{dk}{(k^2+M^2)^{3/2}}(kr)^2|j_l(kr)|^2 \\ =& -\frac{1}{4}\int_0^\infty \frac{r^2du}{(u^2+(Mr)^2)^{3/2}}u^2|j_l(u)|^2.\end{aligned} \tag{4.40}$$

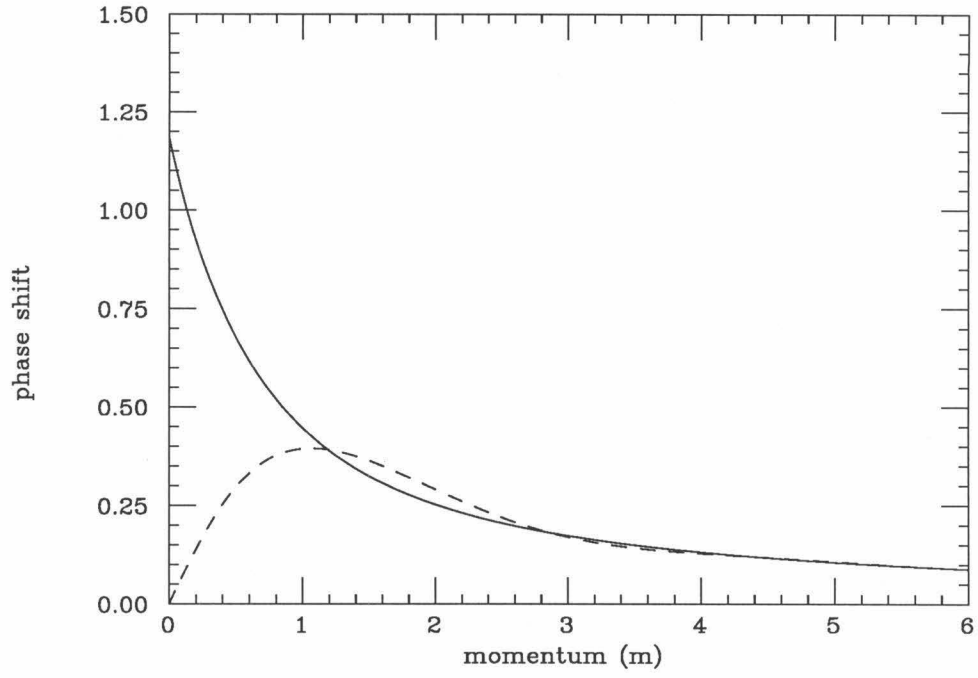

Figure 4.1 – S-wave phase shift vs. momentum for $\phi_b = 0.2$, $R = 1$, and $T = 0.5$. The solid line is the WKB approximation and the dashed line is the exact result. The WKB approximation is bad at low momentum.

We calculate $\gamma(r)$ and $\lambda(r)$ numerically and store them in a table. Observe that they are independent of the background field, so they need to be calculated only once.

We now study the boson-loop energy corrections to the potential

$$M^2(r) = 3\phi^2 - 1, \tag{4.41}$$

where

$$\phi(r) = 1 - \frac{\phi_b}{1 + \exp(\frac{r^2 - R^2}{T^2})}. \tag{4.42}$$

First consider the behavior of the phase shifts in the various partial wave channels. Fig. 4.1 shows the WKB and actual phase shifts as a function of momentum for

$\phi_b = 0.2$, $R = 1$, and $T = 0.5$. The method of calculation of the actual phase shifts is discussed in Appendix D.

For these values of the parameters, the potential supports no bound states. Hence, the exact phase shift is zero at zero. In contrast, the WKB phase shift is ~ 1.2. As a result of this, the WKB approximation fails badly at low momentum and becomes a good approximation only for momenta ~ 4. This behavior is worse than was seen in one dimension. This can be understood by realizing that the central potential selects out only the odd solutions of Equation (4.3), while the one-dimensional systems involve both the even and odd solutions of (4.3). In general, the even and odd phase shifts are different. The WKB solution, on the other hand, does not distinguish between even and odd solutions. Therefore, it provides a better approximation in the one dimensional case when the even and odd solutions are averaged. This can be seen explicitly in Fig. 4.1 where the potential supports one bound odd state and the WKB phase shift is roughly halfway between the phase shift of the odd and even states.

The s-wave phase shifts become progressively better as the potential supports more and more bound states, mainly because the number of bound even and odd parity states differs by one at most. Figure 4.2 shows the same strength potential as Figure 4.1 but with an order of magnitude greater spatial extent. This potential now supports 4 bound s-wave states. In this case the WKB approximation is an excellent approximation to the total phase shift at all momenta.

The WKB approximation also does better as the angular momentum increases. Figure 4.3 shows the phase shifts for the $l = 2, 4$, and 6 partial waves for the parameter values $\phi_b = 0.2$, $R = 1$, and $T = 0.5$. Observe that the WKB approximation works

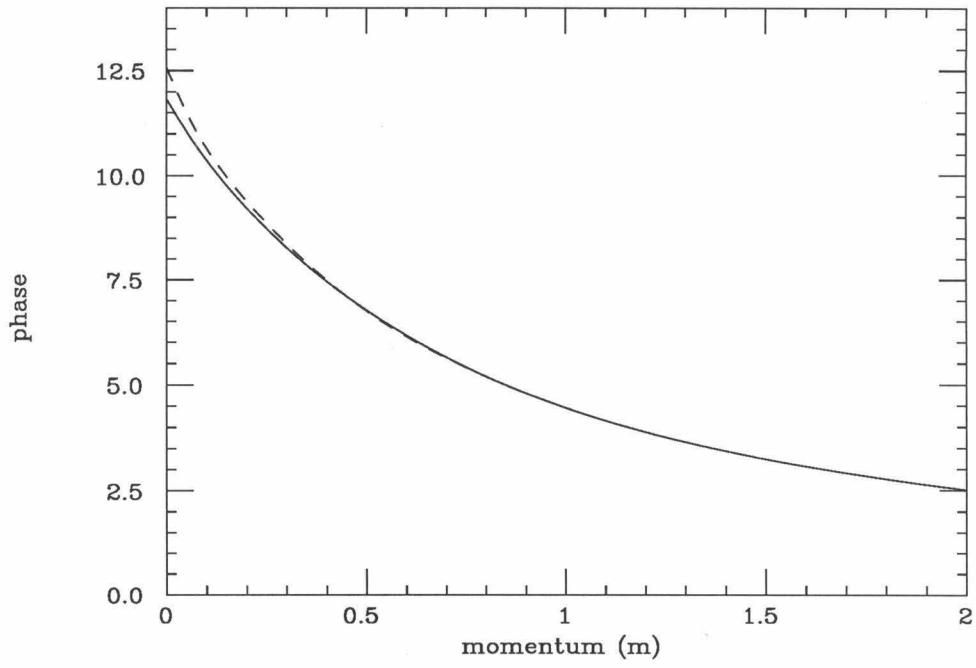

Figure 4.2 – S-wave phase shift vs. momentum for $\phi_b = 0.2$, $R = 10$, and $T = 5$. The solid line is the WKB approximation and the dashed line is the exact result. Here the WKB approximation works well at all momenta.

much better here than for the $l = 0$ wave. Also note that as the angular momentum increases, the magnitude of the phase shift decreases as expected.

As the angular momentum increases, the perturbation of the vacuum occurs at larger energies since it takes an energy of order ω_R,

$$\omega_R^2 = M^2 + \frac{l(l+1)}{R^2}, \tag{4.43}$$

for a particle to have enough energy to be able to overcome the centrifugal barrier classically and see the effects of the potential. For energies near the classical threshold, the local wavelengths are long in the vicinity of the potential, and the WKB approximation is likely to be inaccurate. This is illustrated by the increase of the

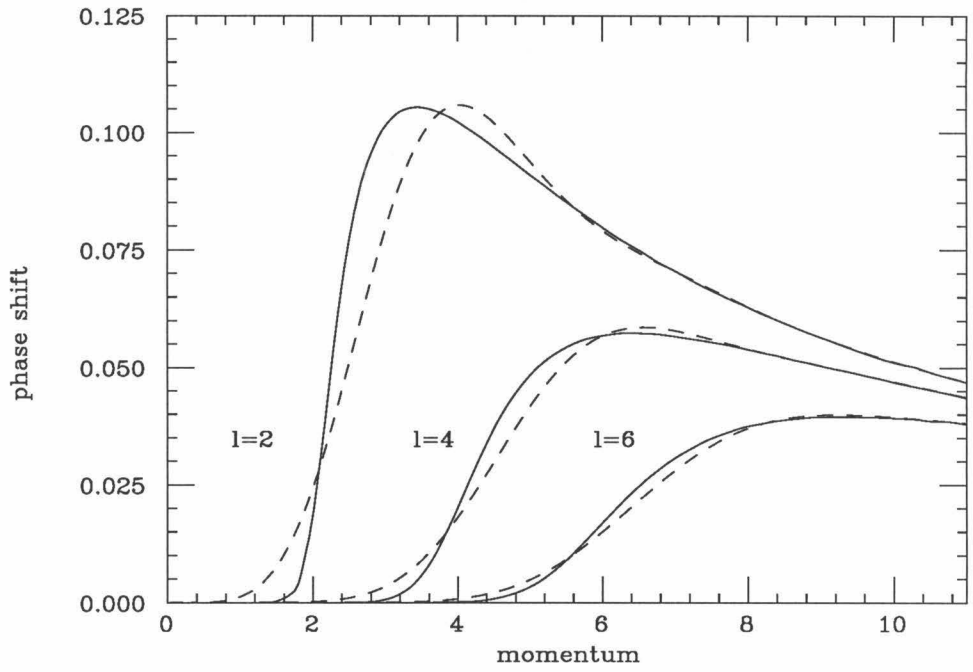

Figure 4.3 – Phase shifts at various angular momenta (l) vs. momentum for $\phi_b = 0.2$, $R = 1$, and $T = 0.5$. The solid line is the WKB approximation and the dashed line is the exact result. The peak of the phase shift increases and the magnitude decreases with increasing angular momentum.

peak of the phase shift with energy as shown in Fig. 4.3. The WKB approximation is not so good for energies near the peak but works very well above the peak.

In Table 4.1, we show the calculations using the WKB approximation for energies above Λ and exact calculations below Λ for $l = 0$ states. The convergence is as one would expect from observing the phase shifts. Note that even in the worse case, $l = 0$ with no bound states, the WKB method still does fairly well.

Table 4.2 shows the convergence of the WKB approximation to the phase-shift integral for various non-zero partial waves. In order to get an accurate answer, we need a cutoff that increases with increasing angular momentum. Most of the phase

ϕ_b	R	T	Λ	E
0.2	1.0	0.5	1.1	0.0417
			1.5	0.0446
			2.0	0.0407
			3.0	0.0412
			4.0	0.0411
			6.0	0.0411
0.2	10.0	5.0	1.1	0.3070
			1.5	0.3073
			2.0	0.3073

Table 4.1 – Convergence of the WKB approximation for $l = 0$ partial waves using the potential of Equation (4.32). The boson-loop energy is calculated exactly for energies below Λ and with the WKB approximation for higher energies. The displayed energy, E, does not contain the contributions from bound states or the finite parts of the counterterms.

shift below the cutoff is so small, however, that one needs only to perform exact calculations in a finite region below the cutoff. This is shown nicely by the $l = 4$ results, where a cutoff of 2.0 gives the same result as a cutoff of 1.0. Only exact solutions above 2.0 play a role. As a result of this, the computational burden does not increase significantly as we go to higher partial waves. Also observe that using the WKB approximation for the full continuum (cutoff of 1) becomes an increasingly good approximation at higher angular momentum as shown in Figure 4.4.

Having calculated the energy in each partial wave, we calculate the total energy by summing up the vacuum energy in each partial wave. It might be hoped that the WKB approximation becomes sufficiently accurate at large angular momentum that an accurate expression could be developed to explicitly sum up the large angular

l	Λ	E
1	1.01	0.0919
	2.0	0.0925
	3.0	0.0975
	4.0	0.0977
	6.0	0.0977
2	1.0	0.1322
	2.0	0.1320
	4.0	0.1343
	6.0	0.1343
4	1.0	0.1803
	2.0	0.1803
	4.0	0.1812
	6.0	0.1810
	8.0	0.1810
6	1.0	0.2110
	4.0	0.2107
	6.0	0.2114
	8.0	0.2113
	10.0	0.2114

Table 4.2 – Convergence of the WKB approximation for partial waves of angular momentum l using the potential of Equation (4.32). The results are all for the parameters $\phi_b = 0.2, R = 1$, and $T = 0.5$. The boson-loop energy is calculated exactly for energies below Λ and with the WKB approximation for higher energies. The displayed energy, E, does not contain the contributions from bound states or the finite parts of the counterterms.

momentum. Unfortunately, various asymptotic approximations for the WKB phase

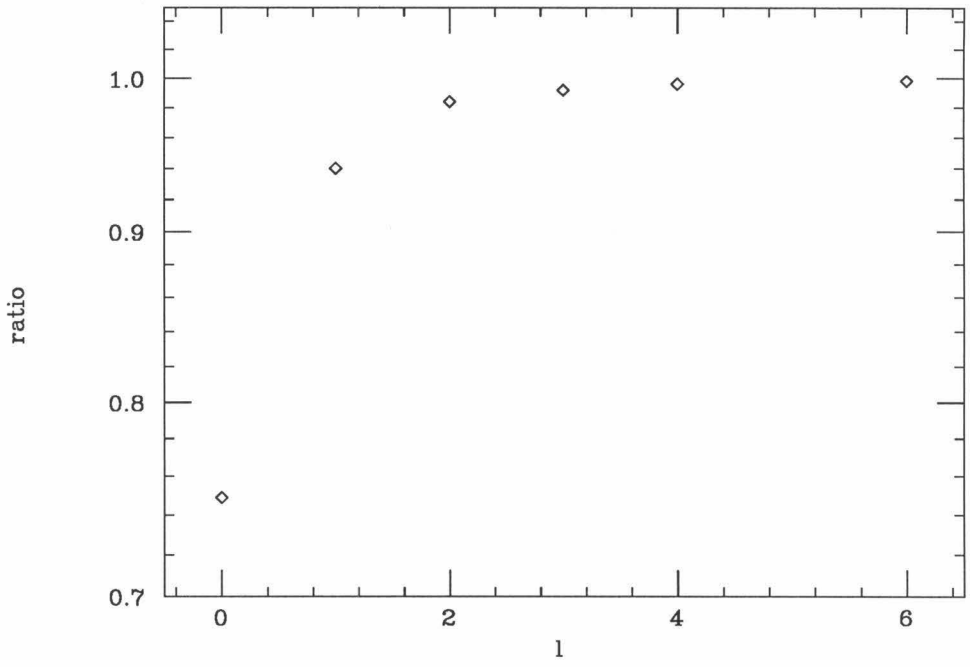

Figure 4.4 – Ratio of the boson-loop energy calculated by using the WKB approximation at all energies to the exact result for various angular momentum channels. The potential parameters are those of Table 4.2.

shift only cancel parts of the counterterm and do not help in calculating the finite part. The best we can do is to calculate explicitly the energy in each partial wave channel and keep summing until we get convergence. This aspect of the calculation is equivalent to what is done in brute-force calculations [13].

In summary, we have used the WKB approximation, which becomes increasingly accurate at large angular momentum, for the high energy states in each partial wave channel to calculate efficiently the vacuum deformation in that partial wave channel.

4.2 Fermion-Loops in Three Spatial Dimensions

Consider spin $\frac{1}{2}$ Dirac fermions coupled to a spherically symmetric scalar field in 3 spatial dimensions. The Dirac equation is

$$(i\gamma \cdot \nabla + g\phi)\psi_i = \gamma^0 \omega_i \psi_i. \tag{4.44}$$

Eigenstates of this Hamiltonian have good total angular momentum j that is a combination of the orbital and spin angular momentum of the fermions [9]. The angular part of the wavefunction is factored out by writing

$$\psi_{n\kappa m}(x) = \frac{1}{r}\begin{pmatrix} iG_{n\kappa}(r)\phi_{\kappa m} \\ -F_{n\kappa}(r)\phi_{-\kappa m}, \end{pmatrix} \tag{4.45}$$

where κ is a non-zero integer that is related to the angular momentum by

$$j = |\kappa| - \frac{1}{2} \tag{4.46}$$

and the angular functions ϕ are

$$\phi_{\kappa m} = \sum_{m_l m_s} \langle l m_l \tfrac{1}{2} m_s | l \tfrac{1}{2} j m \rangle Y_{lm}(\theta, \phi)\chi_{m_s} \tag{4.47}$$

with

$$l = \begin{cases} \kappa & ; \quad \kappa > 0 \\ -(\kappa + 1) & ; \quad \kappa < 0 \end{cases}. \tag{4.48}$$

Observe that the orbital angular momentum of the upper and lower components differ by one and that each state has a degeneracy of $2j + 1 = 2|\kappa|$. Note that both F and

G must vanish at the origin. In terms of F and G the vector and scalar densities are given by

$$\begin{aligned}\int d^3x\, \psi^\dagger_{n\kappa m}\psi_{n\kappa m} &= \int_0^\infty dr\, (|G_{n\kappa}(r)|^2 + |F_{n\kappa}(r)|^2) \\ \int d^3x\, \bar{\psi}_{n\kappa m}\psi_{n\kappa m} &= \int_0^\infty dr\, (|G_{n\kappa}(r)|^2 - |F_{n\kappa}(r)|^2)\end{aligned} \tag{4.49}$$

and the Dirac equation is

$$\begin{aligned}\frac{d}{dr}G_{n\kappa}(r) + \frac{\kappa}{r}G_{n\kappa}(r) - (\omega_n - g\phi(r))F_{n\kappa}(r) &= 0 \\ \frac{d}{dr}F_{n\kappa}(r) - \frac{\kappa}{r}F_{n\kappa}(r) + (\omega_n + g\phi(r))G_{n\kappa}(r) &= 0.\end{aligned} \tag{4.50}$$

The spectrum is symmetric about zero. In particular, if $\psi_{n\kappa m}(x)$ describes a state with energy ω_n and angular momentum κ, then

$$\psi_{-n-\kappa m}(x) = \frac{1}{r}\begin{pmatrix} iF_{n\kappa}(r)\phi_{-\kappa m} \\ -G_{n\kappa}(r)\phi_{\kappa m}\end{pmatrix} \tag{4.51}$$

describes a state with energy $-\omega$ and angular momentum κ.

The specific solutions for $g\phi(r) = M$, which we will denote $w_{\omega\kappa}(r)$, are given by

$$\kappa > 0$$

$$\begin{aligned}G(\omega,\kappa,r) &= \sqrt{\frac{\omega - M}{2\omega}}u^0_\kappa(kr) \\ F(\omega,\kappa,r) &= \sqrt{\frac{k^2}{2\omega(\omega - M)}}u^0_{\kappa-1}(kr)\end{aligned} \tag{4.52}$$

$$\kappa < 0$$

$$\begin{aligned}G(\omega,\kappa,r) &= -\sqrt{\frac{k^2}{2\omega(\omega + M)}}u^0_{-\kappa-1}(kr) \\ F(\omega,\kappa,r) &= \sqrt{\frac{\omega + M}{2\omega}}u^0_{-\kappa}(kr),\end{aligned}$$

where $u^0_\kappa(kr)$ is defined in Equation (4.4). A useful relation is

$$\sum_{\omega=\pm\epsilon} |G(\omega,\kappa,r)|^2 + |F(\omega,\kappa,r)|^2 = |u^0_{|\kappa|}(kr)|^2 + |u^0_{|\kappa|-1}(kr)|^2, \tag{4.53}$$

where $k = \sqrt{\epsilon^2 - M^2}$. Asymptotically,

$$G(r) \propto \sin(kr - \frac{l\pi}{2}) \ , \ r \to \infty \tag{4.54}$$

and

$$F(r) \propto \cos(kr - \frac{l\pi}{2}) \ , \ r \to \infty. \tag{4.55}$$

For systems with varying $M(r) = g\phi(r)$, the asymptotic behavior will be

$$G(r) \propto \sin(kr - \frac{l\pi}{2} + \delta_\kappa(k)) \ , \ r \to \infty \tag{4.56}$$

and

$$F(r) \propto \cos(kr - \frac{l\pi}{2} + \delta_\kappa(k)) \ , \ r \to \infty. \tag{4.57}$$

This defines the phase shifts for the Dirac equation in three spatial dimensions. A straightforward application of the phase-shift formalism for the fermion loop implies

$$\begin{aligned} E_{\rm fl} &= \sum_\kappa 2|\kappa| \lim_{\Lambda\to\infty} \sum_{-\Lambda<\omega_{\kappa n}<0} \omega_n - \omega^0_n + E_{\rm ct}(\Lambda) \\ &= \sum_\kappa 2|\kappa| \Big(\sum_{-M<\omega_{\kappa n}<0} (\omega_{\kappa n} + M) \\ &\quad + \lim_{\Lambda\to\infty} \int_M^\Lambda \delta(\omega) d\omega + E^\kappa_{\rm ct}(\Lambda) \Big). \end{aligned} \tag{4.58}$$

The WKB approximations for the phase shift are generated from the second-order equations that F and G obey separately,

$$\begin{aligned}\left[\frac{d}{dr}-\frac{\kappa}{r}\right]\left[\frac{1}{\omega-M(r)}\left(\frac{dG}{dr}+\frac{\kappa}{r}G\right)\right]+(\omega+M(r))G=&0\\ \left[\frac{d}{dr}+\frac{\kappa}{r}\right]\left[\frac{-1}{\omega+M(r)}\left(\frac{dF}{dr}-\frac{\kappa}{r}F\right)\right]-(\omega-M(r))F=&0.\end{aligned} \tag{4.59}$$

By making the substitutions

$$\begin{aligned}G=&\sqrt{\omega-M(r)}g\\ F=&\sqrt{\omega+M(r)}f,\end{aligned} \tag{4.60}$$

the second-order equations become

$$\begin{aligned}\frac{d^2g}{dr^2}+k_g^2(\omega,\kappa,r)=&0\\ \frac{d^2f}{dr^2}+k_f^2(\omega,\kappa,r)=&0,\end{aligned} \tag{4.61}$$

where

$$\begin{aligned}k_g^2(\omega,\kappa,r)=&\omega^2-\frac{\kappa(\kappa+1)}{r^2}-g^2\phi^2\\ &-\frac{3}{4}\frac{(M'(r))^2}{(\omega-M(r))^2}+\frac{\kappa}{r}\frac{M'(r)}{\omega-M(r)}-\frac{1}{2}\frac{M''(r)}{\omega-M(r)}\\ k_f^2(\omega,\kappa,r)=&\omega^2-\frac{\kappa(\kappa-1)}{r^2}-g^2\phi^2\\ &-\frac{3}{4}\frac{(M'(r))^2}{(\omega+M(r))^2}+\frac{\kappa}{r}\frac{M'(r)}{\omega+M(r)}+\frac{1}{2}\frac{M''(r)}{\omega+M(r)}.\end{aligned} \tag{4.62}$$

The WKB phase shifts are then determined by simply integrating these wave numbers. In particular,

$$\int_{\bar{\Lambda}}^{\Lambda}\delta(\omega)d\omega=\int_0^{\infty}dr\left[\frac{1}{2}\int_{\bar{\Lambda}_g}^{\Lambda}d\omega\,k_g(\omega,\kappa,r)+\frac{1}{2}\int_{\bar{\Lambda}_f}^{\Lambda}d\omega\,k_f(\omega,\kappa,r)-\int_{\bar{\Lambda}}^{\Lambda}d\omega\sqrt{\omega^2-M^2}\right]. \tag{4.63}$$

Here

$$\begin{aligned} \bar{\Lambda}_g &= \max(\Lambda_g, \bar{\Lambda}) \\ \bar{\Lambda}_f &= \max(\Lambda_f, \bar{\Lambda}), \end{aligned} \tag{4.64}$$

where

$$\begin{aligned} k_g(\Lambda_g, \kappa, r) &= 0 \\ k_f(\Lambda_f, \kappa, r) &= 0. \end{aligned} \tag{4.65}$$

This expression exhibits the usual logarithmic divergence, which implies

$$E^{\kappa}_{\mathrm{WKB}}(\Lambda) = \frac{1}{2\pi} \int_0^{\infty} dr\, (g^2\phi^2 - M^2) \log\left(\frac{\Lambda}{M}\right) + \mathcal{O}(\Lambda^0). \tag{4.66}$$

The counterterms needed for a scalar field in $3+1$ dimensions are given in Appendix A. The partial wave decomposition is performed as in the previous section, where we now use the eigenstates of the Dirac equation (4.44) to perform the trace. For a scalar field, we can take advantage of the symmetry of the energy spectra and use the results from the previous section directly [13]. Letting $h = i\gamma^0\gamma\cdot\nabla + \gamma^0 g\phi(r)$, we have

$$h^2\psi_{n\kappa}(r) = \omega^2_{n\kappa}\psi_{n\kappa}(r), \tag{4.67}$$

where

$$h^2 = -\nabla^2 + M^2 + V(r) \tag{4.68}$$

with

$$V(r) = g^2\phi^2 - M^2 + ig\gamma\cdot\nabla. \tag{4.69}$$

Observe that h^2 is of the form of the boson operators studied in the previous section. Each eigenvalue of this equation is doubly degenerate because of the symmetry of the

Dirac equation spectrum. This implies that the boson-loop energy calculated from h^2 will be minus the fermion-loop energy calculated from h,

$$\begin{aligned} E_{\rm fl} &= \sum_{\omega_{\kappa n},0} \omega_{\kappa n} - \omega^0_{\kappa n} \\ &= -\frac{1}{2}\sum_{\kappa n} |\omega_{\kappa n}| - |\omega^0_{\kappa n}| = -E_{\rm bl}. \end{aligned} \tag{4.70}$$

Thus,

$$E_{\rm ct} = \sum_{\kappa} 2|\kappa| E^{\kappa}_{\rm ct},$$

where

$$\begin{aligned} E^{\kappa}_{\rm ct} = -\int_0^{\Lambda_p} dk \Big[&-\frac{1}{4\pi}\frac{1}{\sqrt{k^2+M^2}} \int_0^{\infty} dr \left(|u^0_{|\kappa|}(kr)|^2 + |u^0_{|\kappa|-1}(kr)|^2 \right) \\ &\times \left(g^2\phi^2(r) - M^2 \right) \\ &+ \frac{1}{16\pi}\frac{1}{(k^2+M^2)^{3/2}} \int_0^{\infty} dr \left(|u^0_{|\kappa|}(kr)|^2 + |u^0_{|\kappa|-1}(kr)|^2 \right) \\ &\times \left((g^2\phi^2 - M^2)^2 + g^2 \nabla\phi\cdot\nabla\phi \right) \Big]. \end{aligned} \tag{4.71}$$

In order to get this result we have used Equation (4.53) to sum the magnitudes of the positive and negative energy solutions at a given momentum and the fact that the trace of a single gamma matrix is zero.

We can isolate the high-energy behavior of the counterterm as in the previous section, yielding

$$E^{\kappa}_{\rm ct}(\Lambda) = \frac{1}{2\pi}\log\left(\frac{\Lambda}{M}\right) \int_0^{\infty} dr\, (g^2\phi^2 - M^2), \tag{4.72}$$

which cancels the divergent part of the WKB approximation. Finally, note that in any actual calculation we would need to add finite pieces to the counterterms in order to specify the desired renormalization prescription.

This completes our discussion of the formalism necessary to use the WKB approximation for three-dimensional, fermion-loop calculations. The behavior of the approximation with respect to various partial waves is as in the previous section, so additional results are not presented here.

Chapter 5
Relativistic Hartree Calculations of Finite Nuclei

In this chapter, we examine the polarization of the strong interaction vacuum by the nuclear mean field. In the first section we review relativistic models of the nuclei that suggest that the nuclear mean field is made up of two large components that approximately cancel for hadrons but are very large for antihadrons. If this concept of the mean field is correct, then strong vacuum polarization effects will occur. We calculate these effects in the next two sections, using a hadronic field theory. In the fourth section experimental probes of such strong vacuum perturbations are discussed. The fifth section examines to see whether we expect these hadronic theories to give a reasonable description of the strong interaction vacuum, and in the last section we examine alternative "vacuum effects" in the nucleus, which have been proposed.

5.1 Relativistic Nuclear Models

A nucleus with atomic number A is a bound state of $3A$ quarks. Within the nucleus, these quarks are clustered into nucleons that interact weakly compared to their mass scale. Traditionally, the nucleus is modeled as non-relativistic nucleons interating via potentials, a picture that is sufficient for understanding many aspects of nuclear structure. Within these models, one finds that the nucleons move in a potential well approximately 50 MeV deep.

Modern nuclear physics is increasingly concerned with studying the response of nuclei to a variety of external probes with energies exceeding 1 GeV, a regime in which the traditional nuclear models begin to lose their usefulness. One approach

is to try to extend the successful non-relativistic hadronic models into this regime. Such an extension requires, at minimum, the introduction of relativistic kinematics for the nucleons and retardation in the nucleon-nucleon interaction. In addition, one would like to include the effects of non-nucleonic degrees of freedom such as mesons and nucleon resonances that play a large role at these energies.

The first clue that such an approach might be possible came in analyzing the elastic scattering of protons and other hadrons off nuclei at energies in the regime of 500 MeV. Typically, one analyzes elastic scattering data by assuming that the incident particle obeys a single particle Schrödinger equation moving in a (non-local) potential known as the optical potential. It is found that the elastic scattering data can be reproduced quite easily if one replaces the Schrödinger equation by a Dirac equation [22],

$$[-i\alpha \cdot \nabla - \beta[M - U_s(x)] - U_v^0(x)]\psi(\mathbf{x}) = \epsilon\psi(\mathbf{x}). \tag{5.1}$$

For scattering of an isospin-symmetric, spin-zero target, one expects the relativistic optical potential to be dominated by a scalar and time component of a vector piece. In order to reproduce the data, one needs to have an attractive scalar field with strength of order 400 MeV and a repulsive vector field with strength of order 350 MeV. To see the significance of these strong fields, consider the non-relativistic limit of (5.1) generated by the Foldy-Wouthuysen transformation [23],

$$\left[-\frac{1}{2}\nabla\frac{1}{M - U_s(x)}\nabla + U_v^0(r) - U_s(r) + \frac{1}{2M^2 r}\frac{d}{dr}(U_s + U_v^0)\mathbf{L}\cdot\mathbf{S}\right]\Psi = (\epsilon - M)\Psi. \tag{5.2}$$

The scalar and vector potentials cancel to give the standard 50 MeV nuclear mean field but add to generate the strong spin-orbit force observed in nuclei. This natural

ability of the Dirac formalism to generate a small mean field but strong spin-orbit field is its primary success. Using these mean fields, one can also successfully construct bound state wavefunctions that agree with experimental separation energies and nuclear densities. Thus, phenomenologically, the motion of nucleons in the nuclear mean field can be treated with the Dirac equation [9].

Furthermore, the nucleon-nucleon interaction can be effectively parameterized in terms of the exchange of mesons, taking into account the finite size of the particles involved with vertex form factors [24]. In the isosinglet channel the short range repulsion is attributed to the exchange of the isosinglect vector ω meson, while the intermediate range attraction is due to correlated exchange of two pions that can be effectively modeled by a single scalar meson, the σ. Physically, the σ appears as a broad two pion s-wave resonance centered at around 550 MeV.

The Walecka model [9] is an attempt to combine the phenomenological successes of Dirac phenomenology and meson exchange into a relativistic nuclear model that supports a well-defined computational scheme. The hope is to be able to reproduce the successful phenomenology and compute corrections to it. The only well-defined relativistic models with predictive power that exist are renormalizable quantum field theories, an example being QCD, which is the underlying theory of the strong interaction. Unfortunately, QCD is currently computationally intractable for low and medium energy nuclear physics applications. Instead, the Walecka model is formulated in terms of the correct long-distance degrees of freedom of the strong interaction. For such a theory to be correct, it can not be sensitive to short-distance physics where it is known to be incorrect. The renormalizability of the theory implies that it will not be sensitive to short-range behavior, but it is a computational question as to whether this scale is big enough to make the theory believable. In particular, we hope that

the solutions are dominated by valence particle effects so that we can generate a relativistic theory of nuclear structure. One major problem with trying to construct a renormalizable hadronic theory is that relevant degrees of freedom such as the delta resonance (a spin 3/2 fermion) and the pion (a pseudoscalar meson) are difficult to include in a physically acceptable way.

In its simplest formulation, one includes only the isosinglet ω and σ mesons, giving the Lagrangian density,

$$\begin{aligned}\mathcal{L} =&\bar{\psi}[i\gamma^{\mu}(\partial_{\mu} + ig_{\lambda v}\omega_{\mu}) - M + g_s\phi]\psi \\ &+ \frac{1}{2}(\partial_{\mu}\phi\partial^{\mu}\phi - m_s^2\phi^2) - \frac{1}{4}G_{\mu\nu}G^{\mu\nu} + \frac{1}{2}m_{\omega}^2\omega_{\mu}\omega^{\mu}.\end{aligned} \tag{5.3}$$

Here $G^{\mu\nu} = \partial^{\mu}\omega^{\nu} - \partial^{\nu}\omega^{\mu}$ is the kinetic energy of the ω meson, M is the mass of the nucleon (ignoring the small neutron-proton mass difference), ψ is an isodoublet of 4 component Dirac spinors that represents the nucleon, g_s is the ϕ meson-nucleon coupling and g_{ω} is the ω meson-nucleon coupling. This model describes nucleons interacting through the exchange of a single scalar and vector meson. The scalar meson generates the intermediate range attraction in the nucleon-nucleon force and the vector meson generates the short range repulsion. These mesons have no self-interaction or mutual interactions. Consistent with renormalizability, one could also add cubic and quartic scalar self-interation terms to the lagrangian; however, these produce three and four body forces which are not believed to be large in nuclei. Also note that the neutral vector meson has no problems with renormalizability since it couples to a conserved baryon current.

It is also important to add in the isospin breaking effect of the photon (A^{μ}) as it contributes several MeV per nucleon of energy to a typical nucleus. This comes into the Lagrangian in the same way as the ω meson, except that it couples only to the proton with coupling constant e and is massless. Since the scalar field couples

to the nucleons in the same way as the nucleon mass, it is conventional to define the effective nucleon mass (that is spatially varying for finite systems) to be

$$M^*(\mathbf{x}) = M - g_s\phi(\mathbf{x}). \tag{5.4}$$

The first calculations with this model [23] were performed in the mean-field approximation (MFT) in which the meson fields are assumed to be classical and the valence fermions are treated in the Hartree approximation, as discussed in Chapter 2. For spin 0 nuclei, the spatial components of the vector fields do not contribute. In this approximation, the energy of the resulting nuclear system is

$$E = E_{\text{valence}} + E_{\text{meson}}. \tag{5.5}$$

E_{valence} is the energy of the valence nucleons and is given by the sum of the single-particle energies of the occupied nucleon states,

$$E_{\text{valence}} = \sum_{0<\epsilon_i<\epsilon_f} \epsilon_i, \tag{5.6}$$

where the ϵ_i are determined as eigenvalues of the Dirac equation

$$\left[-i\alpha\cdot\nabla - \beta M^* - g_\omega\omega^0 - \frac{e}{2}(1+\tau_3)A^0\right]\psi_i(\mathbf{x}) = \epsilon_i\psi_i(\mathbf{x}). \tag{5.7}$$

The nucleon isospin quantum number is denoted τ_3 and equals 1 for protons and -1 for neutrons. E_{meson} is the energy stored in the meson fields,

$$E_{\text{meson}} = \int d^3\mathbf{x}\frac{1}{2}[(\nabla\phi)^2 + m_s^2\phi^2] - \frac{1}{2}[(\nabla\omega^0)^2 + m_\omega^2(\omega^0)^2 + (\nabla A^0)^2]. \tag{5.8}$$

Requiring that the nuclear ground state minimize E implies that the meson fields obey

$$\begin{aligned}(\nabla^2 - m_s^2)\phi &= -\, g_s \rho_s^{\text{valence}} \\ (\nabla^2 - m_\omega^2)\omega^0 &= -\, g_\omega \rho_b^{\text{valence}} \\ (\nabla^2)A^0 &= -\, e\rho_p^{\text{valence}},\end{aligned} \tag{5.9}$$

where ρ_s, ρ_b, and ρ_p are the scalar, baryon, and proton densities induced by the valence nucleons,

$$\begin{aligned}\rho_s^{\text{valence}} &= \sum_{0<\epsilon_i<\epsilon_f} \psi_i^\dagger \gamma^0 \psi_i \\ \rho_b^{\text{valence}} &= \sum_{0<\epsilon_i<\epsilon_f} \psi_i^\dagger \psi_i \\ \rho_p^{\text{valence}} &= \sum_{0<\epsilon_i<\epsilon_f} \frac{1}{2}(1+\tau_3^i)\psi_i^\dagger \psi_i.\end{aligned} \tag{5.10}$$

For given values of the parameters, it is straightforward to solve the preceding equations for nuclear matter and closed shell finite nuclei [23]. As the omega meson mass is known to be 783 MeV, this model has three unknown parameters: the two meson-nucleon coupling constants and the scalar meson mass. Two of these (g_ω/m_ω and g_s/m_s) are determined by demanding that symmetric nuclear matter saturates at the right density and binding energy ($k_f = 1.3\,\text{fm}^{-1}, E/A - M = 15.75\,\text{MeV}$). The third (the individual magnitudes of the scalar meson parameters) is chosen to give the correct RMS charge radius of ^{40}Ca. When this is done, it is found that one gets good values for nuclear densities and separation energies throughout the periodic table. When these nuclear densities are combined with hadron-nucleon scattering amplitudes, the success of the Dirac phenomenology is reproduced. A problem is that these nuclei are underbound by an order of 25 percent, an effect that is attributed to a poor representation of the surface energy. This problem with the mean-field theory can be remedied by adding in cubic and quartic scalar terms to the

Lagrangian. Here, parameter sets can be found that get the total energy correct and also reproduce the structure of deformed nuclei to a level of accuracy equivalent to that of non-relativistic mean field calculations [25] .

5.2 One-Loop Calculations in the Walecka Model

The mean field that the valence nucleons move in also disturbs the vacuum. This perturbation contributes additional energy to the nucleus, as well as non-vanishing vector and scalar densities. In non-relativistic models the strength of the mean field is 50 MeV, which is much smaller than M, so one would expect such vacuum effects to be small. On the other hand, in relativistic models the nuclear potential felt by nucleons is composed of large scalar and vector pieces that approximately cancel. Under charge conjugation, the vector field changes sign, while the scalar field doesn't. Hence, holes in the negative energy sea feel a potential equal to the sum of the scalar and vector fields that is 1000 MeV deep (see Fig. 5.1), of order of the nucleon mass. As a consequence of this, strong vacuum polarization effects are likely in these relativistic models.

The mean-field calculations described in the previous section ignore the negative-energy solutions of the Dirac equation (5.7). By treating the Lagrangian (5.3) at the one-loop level as discussed in Chapter two, the phenomenologically successful mean-field theory is recovered along with an additional contribution that is due to the perturbation of the vacuum by the mean field. At the one-loop level, the energy of the system is given by

$$E = E_{\text{valence}} + E_{\text{meson}} + E_{\text{sea}}, \tag{5.11}$$

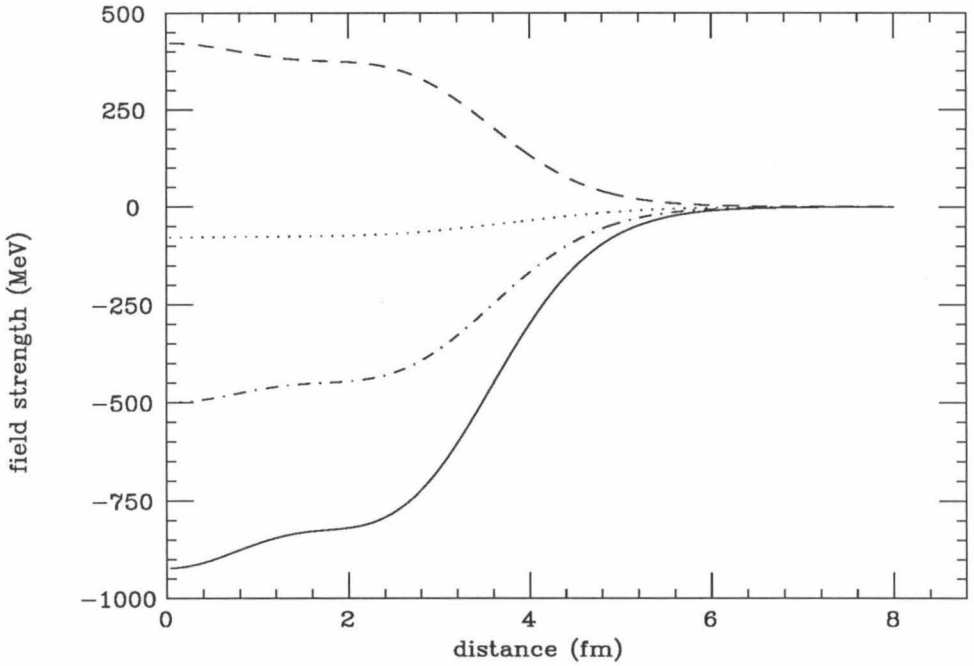

Figure 5.1 – In the Walecka model, nucleons and antinucleons feel vastly different mean fields. The solid line represents the mean field felt by antineutrons, while the dotted line represents the mean field felt by neutrons. The dashed and dashed-dotted lines represent the individual contributions of the omega and sigma meson fields. For the proton, the vector contribution is increased slightly because of the Coulomb interaction.

where $E_{\rm valence}$ is given by Eq. (5.6) and $E_{\rm meson}$ is given by Eq. (5.8). $E_{\rm sea}$ is the perturbation of the Dirac sea (see Section 2.2),

$$E_{\rm sea} = \sum_{\epsilon_i<0} (\epsilon_i - \epsilon_i^0) + E_{\rm ct}, \tag{5.12}$$

where ϵ_i^0 are the single particle energies of nucleons in the unperturbed Dirac sea, ϵ_i are eigenvalues of the Dirac equation (5.7) and $E_{\rm ct}$ are the counterterms to be discussed later. Because of the large potential that the negative-energy states feel, the number of states contributing to the sum in Eq. (5.12) is enormous. A simple

estimate of the number of bound negative-energy states can be obtained using the fermi gas model. For a scalar field $V_s = 450\,\mathrm{MeV}$ and a vector field $V_v = 375\,\mathrm{MeV}$, the fermi momentum of the bound negative-energy states is $k_f^- = 6.2\,\mathrm{fm}^{-1}$, implying that the number of bound negative energy states in a nucleus of radius R_0 is

$$4\int_0^{R_0}\int_0^{k_f^-}\frac{d^3k\,d^3x}{(2\pi)^3},$$

which equals 3500 for ^{40}Ca.

The effect of the Dirac sea in nuclear matter (the effective potential) was calculated by Chin and Walecka [26]. Horowitz and Serot then applied this result to finite nuclei using the local density approximation (LDA) [15]. This was motivated by the thought that the large number of negative energy bound states would make such an approximation accurate. Subsequently, Perry found that the large field gradients near the surface (in which the mean field goes from the order of the nucleon mass to zero) play a role comparable to the effect of the magnitude of the field, implying that there are important corrections to the LDA. In particular, the field gradients induce local nucleon density in the vacuum, an effect that does not occur in the LDA. Perry showed that these effects can be calculated using the derivative expansion of the effective action (see Sec. 2.4 and Appendix C)), which is apparently convergent for finite nuclei [27]. In this section, we perform self-consistent calculations of finite nuclei using the derivative expansion.

The one-loop effective action is

$$S_{\mathrm{eff}} = -i\mathrm{tr}\ln\left[i\gamma^\mu\partial_\mu - M^* - g_\omega\gamma^\mu\omega_\mu - e(\frac{1}{2}+\tau_3)\gamma^\mu A_\mu\right] + \mathcal{L}_{\mathrm{ct}} + \mathcal{L}_{\mathrm{meson}}. \qquad (5.13)$$

The counterterms are discussed thoroughly in Appendix A. In this section, the renormalization is performed at zero external momentum, meaning that the parameters

that appear in the Lagrangian correspond to the physical masses and couplings at zero external momentum. This is a particularly advantageous thing to do for the Walecka model since its proposed regime of validity is for large-distance phenomena. By renormalizing at zero momentum we define our parameters in terms of the longest distance scales possible. The derivative expansion of this effective action is (see [27] and Appendix B)

$$\begin{aligned} S_{\text{eff}} = & - V_{\text{eff}}(\phi) - \frac{1}{4\pi^2} g_s^2 \log\left(\frac{M^*}{M}\right) \partial_\mu \phi \partial^\mu \phi \\ & + \frac{1}{12\pi^2} g_v^2 \log\left(\frac{M^*}{M}\right) G_{\mu\nu} G^{\mu\nu} + \mathcal{O}(\frac{1}{M^{*2}}) \\ & + \mathcal{L}_{\text{meson}}, \end{aligned} \tag{5.14}$$

where V_{eff} is the effective potential,

$$V_{\text{eff}}(\phi) = -\frac{1}{8\pi^2}[2M^{*4}\ln(\frac{M^*}{M}) + 2g_s M^3\phi - 7g_s^2 M^2\phi^2 + \frac{26}{3}g_s^3 M\phi^3 - \frac{25}{6}g_s^4\phi^4], \tag{5.15}$$

which corresponds to the exact result in nuclear matter.

For finite nuclei, this derivative expansion converges rapidly. The relevant dimensionless expansion parameters (see Section 2.4) are derivatives of the field strength divided by powers of the effective mass. For example, in a typical nuclei (Fig 5.1), $g_s \nabla\phi \sim 150\text{MeV/fm}$ and $M^* \sim 500MeV$, implying

$$\frac{g_s \nabla\phi(x)}{M^*(x)^2} \sim \frac{1}{6}. \tag{5.16}$$

Higher-order terms involve at least two powers of this small parameter, and explicit calculations of their contribution to the vacuum energy reveal them to be less than a percent [27]. Hence, to a very good approximation, the energy shift of the Dirac sea is given by

$$E_{\text{sea}} = \int d^3\mathbf{x}\, V_{\text{eff}}(\phi) - \frac{g_s^2}{4\pi^2}\ln(\frac{M^*}{M})(\nabla\phi)^2 + \frac{g_\omega^2}{6\pi^2}\ln(\frac{M^*}{M})(\nabla\omega^0)^2. \tag{5.17}$$

The meson fields (and hence the nucleon wavefunctions) are determined by minimizing the total energy, yielding the equations

$$(\nabla^2 - m_s^2)\phi = -g_s(\rho_s^{\rm val} + \rho_s^{\rm sea})$$

$$(\nabla^2 - m_\omega^2)\omega^0 = -g_\omega(\rho_b^{\rm val} + \rho_b^{\rm sea}), \tag{5.18}$$

where ρ_s and ρ_b are the scalar and baryon densities induced by the valence and sea nucleons. The valence densities are defined in Section (5.1) and

$$\rho_s^{\rm sea} = -\frac{1}{g_s}V'_{\rm eff}(\phi) - \frac{g_s}{2\pi^2}\nabla\cdot\ln(\frac{M^*}{M})\nabla\phi - \frac{g_s^2}{4\pi^2 M^*}(\nabla\phi)^2 + \frac{g_\omega^2}{6\pi^2 M^*}(\nabla\omega^0)^2$$

$$\rho_b^{\rm sea} = -\frac{g_\omega}{3\pi^2}\nabla\cdot\ln(\frac{M^*}{M})\nabla\omega^0. \tag{5.19}$$

Note that $\rho_b^{\rm sea}$ is a total derivative and thus contributes no net baryon density to the nucleus as it must, since baryon number is a conserved quantity and therefore cannot be spontaneously generated in the vacuum. Scalar density, on the other hand, is not a conserved quantity, and net scalar density can be generated in the vacuum.

In nuclear matter, the induced densities in the vacuum are simply

$$\begin{aligned}\rho_s^{\rm sea} &= -\frac{1}{g_s}V'_{\rm eff}(\phi)\\ \rho_b^{\rm sea} &= 0.\end{aligned} \tag{5.20}$$

The meson Equations (5.18 – 19) are easily solved and the energy minimized at each baryon density as discussed in Chapter 2.3. The resulting equation of state depends on the parameters g_s/m_s and g_ω/m_ω. These parameters are fixed by demanding that nuclear matter saturates at the correct density and binding energy. The properties

of nuclear matter in the RHA approximation will be discussed in much more detail in Sections 5.3 and 5.5.

For finite systems, the coupled differential Equations (5.7,5.18-19) for the mesons and nucleons are solved in the standard iterative fashion [23]. Our numerical methods are discussed in Appendix D. The n^{th} iteration of the meson fields is determined by solving the appropriate Klein-Gordon equation where the source terms are generated from the preceding iterations meson fields and nucleon wavefunctions. To maintain a stable algorithm (the presence of derivatives in the source term tends to make this algorithm unstable), we find that we then need to average these meson fields with those of the previous iteration. The n^{th} iteration of the nucleon fields is determined by solving the Dirac equation using the n^{th} iteration of the meson fields. We start the iteration procedure by using Woods-Saxon potentials for the meson fields. This allows us to obtain convergence to five significant figures in the total energy in $20-30$ iterations.

We now present results of calculations of ^{16}O and ^{40}Ca. Our primary interest in these calculations is to determine the self-consistent effect of the derivative terms in Eq. (10) on the structure of these nuclei.

We first need to determine the values of the two meson coupling constants and masses. As mentioned earlier, fitting to the binding energy and saturation density of nuclear matter (in which the vacuum derivative terms do not contribute) fixes the ratios of g_ω/m_ω and g_s/m_s to the values in [15]. The omega meson mass parameter is taken to be the physical mass of the omega meson, 783 MeV. The results we will discuss do not, however, depend significantly on the value chosen for this parameter. This leaves one free parameter. This parameter is conventionally adusted to fit the

	g_s^2	g_ω^2	m_s (MeV)	m_ω (MeV)
MFT	109.6	190.4	520	783
LDA	54.3	102.8	458	783
DE	78.3	102.8	550	783

Table 5.1 – Parameters used for various mean-field calculations. In the MFT calculations the vacuum is ignored, in the LDA calculations the vacuum is treated in the local density approximation, and in the DE calculations the vacuum is treated using the derivative expansion.

rms charge radius of ^{40}Ca. The charge density is computed by folding in the total proton density with the charge density of an individual proton ($\rho^p_{\rm chg}$)

$$\rho^p_{\rm chg}(\mathbf{x}) = \frac{\mu^3}{8\pi}\exp(-\mu|\mathbf{x}|), \tag{5.21}$$

where $\mu = (0.71)^{1/2}$GeV(corresponding to an rms charge radius of 0.74 fm), yielding

$$\rho_{\rm chg}(\mathbf{x}) = \int d^3\mathbf{x}'\,\rho^p_{\rm chg}(\mathbf{x}-\mathbf{x}')\rho_p(\mathbf{x}'). \tag{5.22}$$

This results in $m_s = 550$ MeV. If we ignore the derivative terms in (5.14) but use only the effective potential (LDA) then we find $m_s = 458$ MeV [15], and if we ignore the vacuum all together we find $m_s = 520$ MeV [23]. The parameters of the various models are listed in Table 5.1. Notice the large magnitude of the coupling constants that is characteristic of nuclear models based on meson exchange. This implies that such models can be studied only using methods, such as the RHA, that are non-perturbative in the coupling constants. In particular, calculations that add in corrections perturbatively to the RHA are likely not to be valid. Specific examples of this are shown in [28] where the two loop approximation in nuclear matter is shown to fail miserably. Whether the RHA itself is a decent approximation to the underlying field theory is anyone's guess at the present moment.

The changes in the values of the parameters in Table 5.1 with respect to the various approximations can be understood as follows. The Dirac sea perturbation generates a positive energy contribution to the nucleus. When trying to minimize the total energy, the nucleus will shrink relative to a nucleus that ignores the vacuum. Since we wish to keep the RMS radius fixed, we must adjust the parameters to expand the radius of the valence nucleons. This is accomplished by decreasing the scalar meson mass (a decrease in the scalar meson mass of 5 MeV increases the radius by about 0.01 fm) and is why the scalar meson mass is small in the LDA calculation. When the full Dirac sea contribution is included, we get not only a positive vacuum energy that tends to decrease the size of the valence nucleons, but also an induced baryon density in the sea that increases the total charge radius of the nucleus. In order to compensate for the latter effect, we need to shrink the valence nucleons by increasing the scalar meson mass. The net result is that the scalar meson mass is not that much different from the MFT result.

In Figure 5.2 we show the charge densities of ^{40}Ca and ^{16}O both with and without the presence of the derivative terms. The difference between the two curves is at most a few percent. We see that the shell model fluctuations in the interior of the nucleus have been slightly reduced and that the total interior density has been lowered by about a percent. This is compensated by a slight broadening of the surface. This is somewhat remarkable since the derivative terms contribute only where the density is changing and thus one might expect the density to change more drastically. Raising the scalar mass, which decreases the range but increases the strength of the scalar force, is able to diminish the effect of the derivative terms on the density.

The presence of the derivative terms changes the role the valence nucleons play in determining the total nucleon density. When no derivative terms are present, the

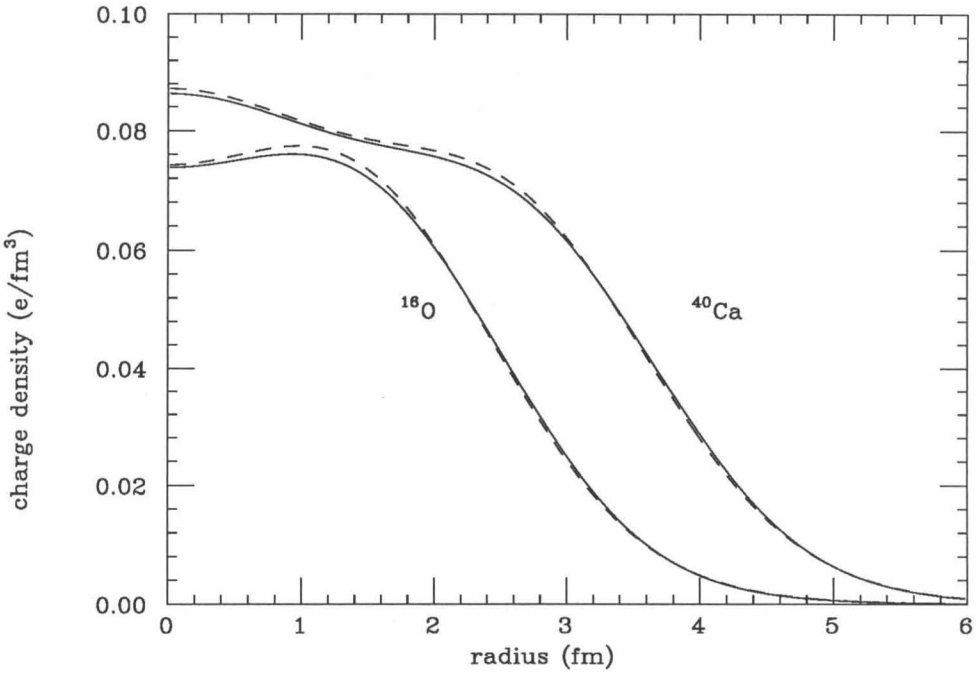

Figure 5.2 – Charge density for ^{16}O and ^{40}Ca. The dashed lines correspond to only including the effective potential and the solid lines to including the full derivative expansion in the calculation of the vacuum energy.

baryon density is determined solely by the valence nucleons. When the derivative terms are added, vacuum polarization also contributes to the baryon density. In Figure 5.3 we graph the fraction of the baryon density that is due to vacuum polarization. This ranges up to five percent of the nucleon density. These large fluctuations occur in both the interior and surface of these light nuclei. The interior fluctuations are due to the interior shell model fluctuations and will diminish in heavier nuclei, while the surface fluctuations will persist in all nuclei. Note that the surface fluctuations are positive for distances larger than the half-density radius and negative for smaller distances.

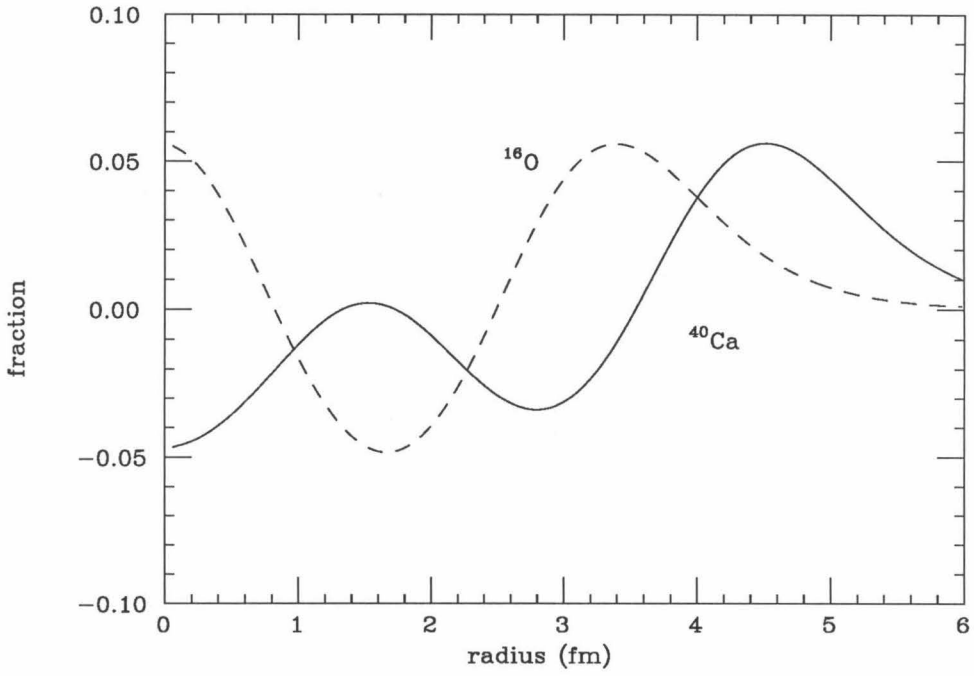

Figure 5.3 – Fraction of nucleon density that is due to vacuum polarization.

The sign of the fluctuations agrees with what we expect physically. If we think of the vacuum as consisting of fluctuating nucleon- antinucleon pairs, then since antinucleons feel a much stronger attraction than nucleons, we expect that the vacuum will polarize with antinucleons nearer the nucleus. Hence, the induced baryon density will be negative near the center of the nucleus and positive outside, agreeing with what we have calculated.

To accommodate the baryon density fluctuations induced in the vacuum and still keep the total size and density of the nucleus roughly the same, the valence nucleons must rearrange themselves. In particular, since the Dirac sea contributes a positive nucleon density at large distances, the valence nucleons must contract. The change in meson fields necessary to accommodate this rearrangement turns out to be very

small. For example, in figure 5.4, we plot the effective mass for ^{40}Ca; the inclusion of the derivative terms has a very small effect on the effective mass relative to the LDA results. Observe that the LDA results are significantly different from the MFT results because of the large scalar density that is induced in the vacuum and the resulting change in parameters that is necessary to accommodate this.

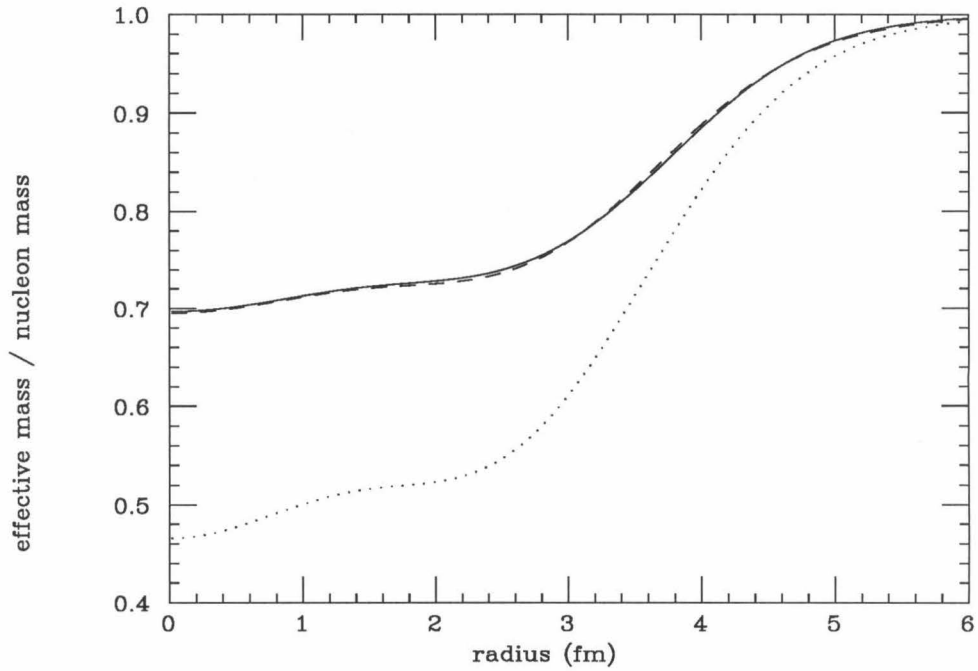

Figure 5.4 – Effective mass (in units of the nucleon mass) vs. distance for ^{40}Ca. The dotted line corresponds to the MFT results, the dashed line to the LDA results, and the solid line to the DE results.

The rearrangement of the valence nucleons does have a noticeable effect on the binding energies of the nuclei. In Table 5.2 we list results for ^{16}O and ^{40}Ca (DE) and compare them with results when only the effective potential is used (LDA). The comparison between the effective potential results and the no-vacuum results has been

carried out in [23]. Although the vacuum terms directly contribute positive energy to the nucleus, the total effect of their inclusion is to increase the binding. The effect is greatest in oxygen (0.8 MeV) and less in calcium (0.5 MeV). The shifts in binding energy are too small to resolve the descrepancy with the experimental values. Note that if one includes only the effective potential, which leads to large changes in the strengths of the potentials relative to the MFT, then the binding energies are unchanged compared with the MFT [15]. In both of these calculations, the nucleon density is determined only by the valence nuclei. This leads us to conclude that the shift in binding energy is due to the baryon density fluctuations in the vacuum induced by the derivative terms, which forces the valence nucleons to rearrange themselves. This will be further demonstrated in Section 5.6 when we examine the effect of medium modifications of the nucleon form factor.

Most of this shift in binding energy is reflected in a shift in the single particle energies of the nucleons, shown in Table 5.3. Observe that the shifts are greatest for the higher angular momentum states that are more sensitive to the surface region of the nucleus. The increase in binding energy can be understood as an effect of the shrinking of the rms radius of the valence nucleons (see Table 5.2) that is due to the presence of positive baryon number fluctuations on the surface, which allows the valence nucleons to feel a slightly stronger potential.

In summary, we have used the derivative expansion of the effective action to analyze the effect of the Dirac sea on nuclear structure at the mean-field level. We find significant baryon-number fluctuations induced in the vacuum. In response, the valence nucleons rearrange themselves so that the total size of the nucleus is unchanged, increasing the binding energy of the nucleus. This implies that properly including additonal effects beyond the Hartree level that also generate nucleon-density

^{16}O		
	LDA	DE
charge rad. (fm)	2.77	2.75
nucleon rad. (fm)	2.63	2.59
bind. en. (MeV/A)	4.76	5.47
eff. pot. (MeV/A)	1.70	1.64
deriv. (MeV/A)	(1.25)	1.26

^{40}Ca		
	LDA	DE
charge rad. (fm)	3.48	3.48
nucleon rad. (fm)	3.36	3.34
bind. en. (MeV/A)	6.25	6.73
eff. pot. (MeV/A)	2.42	2.35
deriv. (MeV/A)	(0.98)	0.98

Table 5.2 – Various results for ^{16}O and ^{40}Ca treating the vacuum with the derivative expansion (DE) and the local density approximation (LDA). Specifically tabulated are the rms charge radius, the rms nucleon radius, the total binding energy per nucleon, the contribution of the effective potential to the total energy per nucleon (eff. pot.), and the contribution of the derivative terms in Eq. (5) to the total energy per nucleon (deriv.).

fluctuations with respect to the Hartree density could also provide additional binding energy and presumably increase the agreement of the model with experiment. An example of this is correlations among the valence nucleons. These effectively generate a fractional occupancy of the single-particle Hartree states. Since the less bound states have a greater spatial extent than the tightly bound states, the effect of correlations is to generate an induced nucleon density that is negative inside and positive outside

^{16}O	DE	LDA	^{40}Ca	DE	LDA
$1s_{1/2}$	30.4	29.8	$1s_{1/2}$	36.5	36.3
$1p_{3/2}$	14.2	13.5	$1p_{3/2}$	24.8	24.4
$1p_{1/2}$	11.2	10.5	$1p_{1/2}$	22.9	22.4
			$1d_{5/2}$	12.1	11.7
			$1d_{3/2}$	8.9	8.4
			$2s_{1/2}$	7.0	6.9

Table 5.3 – Effect of derivative terms on single-particle energies.

the nucleus, just as the Dirac sea does. Also note that the energy of the correlations relative to the Hartree state will be positive. Hence, we would expect that the self-consistent effect of correlations would be to further increase the binding energy in the Walecka model.

5.3 Effect of Strange Baryons

The standard Walecka model consists of protons and neutrons interacting via mesons, and so it is only the deformation of the proton and neutron vacuum that is taken into account in these calculations. The real world consists of many other baryonic degrees of freedom besides protons and neutrons. Any baryons that couple to the ϕ and ω fields will contribute to the vacuum polarization even if they are not present as valence particles in the nucleus. In this section we estimate the role that such additional vacuum polarization effects will play. One interesting effect is that these baryons carry quantum numbers (such as strangeness) that are not found in the valence part of the nucleus, and hence shifts in their vacuum could be easier to see experimentally (see Section 5.4).

The Walecka model is meant to describe strongly interacting baryons. As such, one possibility is to assume that all strong interaction baryon resonances should come out from the interaction and not be put in by hand. In particular, they should not be present in the Dirac sea. However, particles that are related to each other only by the weak interaction should be considered as fundamental degrees of freedom in the model. This implies that the baryon octect (listed in Table 5.4) as well as the Ω^- should be considered as fundamental degrees of freedom.

λ	M_λ	e_λ	s_λ	g_λ
p	939	1	0	1
n	939	0	0	1
Λ	1116	0	-1	2/3
Σ^+	1189	1	-1	2/3
Σ^0	1193	0	-1	2/3
Σ^-	1197	-1	-1	2/3
Ξ^0	1315	0	-2	1/3
Ξ^-	1321	-1	-2	1/3

Table 5.4 – Values of parameters used for the baryon octet. M is the mass of the particles in MeV, e is the charge in units of the proton charge, s is the strangeness, and g is the strength with which the particles couple to the scalar and vector mesons in units of the nucleon coupling and λ denotes the various baryons.

In a normal nucleus, the dominant strong interaction mesons fields are the isoscalar-scalar field ϕ and the isoscalar-vector field ω^0. The Lagrangian density

for the Walecka model extended to include the baryon octet is

$$\begin{aligned}\mathcal{L} = &\sum_{\lambda} \bar{\psi}^{\lambda}[i\gamma^{\mu}(\partial_{\mu} + ig_{\lambda v}\omega_{\mu}) - M_{\lambda} + g_{\lambda s}\phi]\psi^{\lambda} \\ &+ \frac{1}{2}(\partial_{\mu}\phi\partial^{\mu}\phi - m_s^2\phi^2) - \frac{1}{4}G_{\mu\nu}G^{\mu\nu} + \frac{1}{2}m_v^2\omega_{\mu}\omega^{\mu}.\end{aligned} \tag{5.23}$$

Here λ refers to the type of baryon with M_{λ} being its mass, $g_{\lambda s}$ its coupling to the ϕ meson and $g_{\lambda v}$ its coupling to the ω meson. The baryons included in these calculations and some of their properties are shown in Table 5.4.

It is known from studying the energy levels of hypernuclei that strange baryons couple more weakly to the nuclear mean field than nucleons. A rough estimate of these couplings can be provided by a simple quark model argument [29]. The ϕ and ω mesons are made up of only u and d quarks. In the quark model, one assumes that these mesons interact directly with the quarks in the baryon and that the ϕ and ω mesons interact only with the u and d quarks. This implies, for instance, that the Λ that has one s quark interacts with 2/3 the strength of a proton and that the Ω^- with three s quarks is non-interacting and hence not considered in the rest of this paper. We can therefore write

$$\begin{aligned} g_{\lambda s} &= g_{\lambda} g_s \\ g_{\lambda v} &= g_{\lambda} g_v. \end{aligned} \tag{5.24}$$

The values of g_{λ} for the various baryons are listed in Table 5.4.

One can test these couplings for the case of Λ hypernuclei by comparing the resulting single-particle energy levels with experimental ones. If one insists that $g_{\Lambda s}/g_{\Lambda v} = g_{ns}/g_{nv}$, then one finds that $g_{\Lambda} = 1/3$ [30], a factor of two smaller than predicted from quark models. However, slightly relaxing the constraint that these two ratios be exactly equal allows the single-particle energies to be fit for a wide range of coupling constants, implying that the observed single-particle energies of

hypernuclei do not really constrain these couplings. In particular, one can assume that both the scalar and vector couplings are within 10% of 2/3 and get a decent description of the energy levels [31]. The reason for this strong sensitivity on slight changes in the coupling constants is that the valence baryon levels depend on the small difference of the individually large vector and scalar fields. The antibaryons, on the other hand, depend on the sum of the vector and scalar fields and so will be fairly insensitive to slight relative variations in the coupling constants. Therefore, it is safe to ignore this small variation in the scaling of the vector and scalar couplings when calculating the Dirac sea shift. Hence, we use the coupling constants generated from quark model considerations as a reasonable first approximation for the Λ and the rest of the baryons. However, it is important to bear in mind that there is no significant experimental constraint on the magnitude of these couplings. We will comment later on how possible variations in the magnitude of the couplings would affect our results.

We now describe relativistic Hartree calculations of nuclear matter and finite nuclei, using (5.24). The calculations are similar to those of the preceding section. A baryon of type λ and energy ϵ_i^λ is described by a wavefunction $\psi_i(\mathbf{x})$ determined from

$$(-i\alpha\cdot\nabla-\beta M_\lambda^*-g_{\lambda v}\omega^0)\psi_i^\lambda(\mathbf{x})=\epsilon_i^\lambda\psi_i^\lambda(\mathbf{x}), \tag{5.25}$$

where the system has been assumed to be spherically symmetric and $M_\lambda^*=M_\lambda-g_{\lambda s}\phi$ is the spatially varying effective mass of the baryon. The energy of a system occupied by valence baryons with fermi energies ϵ_f^λ is conveniently divided into three parts,

$$E=E_{\text{valence}}+E_{\text{meson}}+E_{\text{sea}}. \tag{5.26}$$

$E_{\rm valence}$ is the energy of the valence nuclei,

$$E_{\rm valence} = \sum_{\lambda} \sum_{\epsilon_f^\lambda > \epsilon_i^\lambda > 0} \epsilon_i^\lambda. \tag{5.27}$$

In normal nuclei, $\epsilon_f^\lambda = 0$ except for protons and neutrons. $E_{\rm meson}$ is the energy of the meson fields given by Eq. (5.8), and $E_{\rm sea}$ is the energy that is due to the perturbation of the Dirac sea,

$$E_{\rm sea} = \sum_{\lambda} \sum_{\epsilon_i^\lambda < 0} (\epsilon_i^\lambda - \epsilon_i^{\lambda 0}) + E_{\rm ct}, \tag{5.28}$$

where $\epsilon_i^{\lambda 0} = -\sqrt{\mathbf{p}_i^2 + M_\lambda^2}$ is the energy of the unperturbed vacuum and $E_{\rm ct}$ is the energy that is due to the counterterms needed to make this sum finite. These counterterms are chosen so that there are no cubic and quartic scalar meson terms in the energy density.

As in the previous section, we evaluate the sea energy using the derivative expansion,

$$E_{\rm sea}^\lambda = \int d^3\mathbf{x}\, V_{\rm eff}^\lambda(\phi) - \frac{g_{\lambda s}^2}{4\pi^2} \ln(\frac{M_\lambda^*}{M_\lambda})(\nabla\phi)^2 + \frac{g_{\lambda v}^2}{6\pi^2} \ln(\frac{M_\lambda^*}{M_\lambda})(\nabla\omega^0)^2 + O(\frac{1}{M_\lambda^*})^2, \tag{5.29}$$

where $V_{\rm eff}^\lambda$ is the effective potential,

$$V_{\rm eff}^\lambda(g_{\lambda s}\phi) = -\frac{1}{8\pi^2}[2M_\lambda^{*4} \ln(\frac{M_\lambda^*}{M_\lambda}) + 2g_{\lambda s}M_\lambda^3\phi - 7g_{\lambda s}^2 M_\lambda^2\phi^2 + \frac{26}{3}g_{\lambda s}^3 M_\lambda \phi^3 - \frac{25}{6}g_{\lambda s}^4\phi^4], \tag{5.30}$$

which corresponds to the exact result in nuclear matter.

Minimizing the total energy gives the familiar equations,

$$(\nabla^2 - m_s^2)\phi = -\sum_{\lambda} g_{\lambda s}(\rho_{\lambda s}^{\rm val} + \rho_{\lambda s}^{\rm sea}) = -g_s(\rho_s^{\rm val} + \rho_s^{\rm sea}) \tag{5.31}$$

$$(\nabla^2 - m_\omega^2)\omega^0 = -\sum_\lambda g_{\lambda s}(\rho_{\lambda b}^{\rm val} + \rho_{\lambda b}^{\rm sea}) = -g_\omega(\rho_b^{\rm val} + \rho_b^{\rm sea}), \tag{5.32}$$

where $\rho_{\lambda s}$ and $\rho_{\lambda b}$ are the scalar and baryon densities induced by the valence and sea baryons. The valence densities are given via Equation (5.10) and the sea densities are determined from the meson fields as

$$\rho_{\lambda s}^{\rm sea} = -\frac{1}{g_{\lambda s}} V'_{\rm eff}(\phi) - \frac{g_{\lambda s}}{2\pi^2}\nabla\cdot\ln(\frac{M_\lambda^*}{M_\lambda})\nabla\phi - \frac{g_{\lambda s}^2}{4\pi^2 M_\lambda^*}(\nabla\phi)^2 + \frac{g_{\lambda v}^2}{6\pi^2 M_\lambda^*}(\nabla\omega^0)^2$$

$$\rho_{\lambda b}^{\rm sea} = -\frac{g_{\lambda v}}{3\pi^2}\nabla\cdot\ln(\frac{M_\lambda^*}{M_\lambda})\nabla\omega^0. \tag{5.33}$$

It is often convenient to refer the induced densities to the equivalent nucleon density that would give rise to the same source term. These nucleon equivalent densities, defined in Eqs. (5.33-5.34) are denoted as $\rho_s^{\rm val}$,$\rho_s^{\rm sea}$, and $\rho_v^{\rm sea}$.

We begin by calculating the properties of isospin-symmetric nuclear matter. Since there is no dependence on position, the gradient terms in the energy functional do not contribute. In particular, the baryon density is due only to the valence nucleons. Thus, the energy density ϵ of nuclear matter with fermi momentum k_f is

$$\epsilon = 4\int_0^{k_f}\frac{d^3\mathbf{k}}{(2\pi)^3}\sqrt{\mathbf{k}^2 + M^{*2}} + \sum_\lambda V_{\rm eff}^\lambda(M^*) + \frac{m_s^2}{2g_s^2}(M - M^*)^2 + \frac{g_v^2}{2m_v^2}\rho_{\rm b}^2, \tag{5.34}$$

where $\rho_b = \frac{2}{3\pi^2}k_f^3$ is the nucleon density and $M^* = M_p - g_{ps}\phi$ is the nucleon effective mass. Note that since $g_{\lambda s}\phi = g_\lambda(M - M^*)$, Eq. (5.30) implies that $V_{\rm eff}^\lambda$ is simply a function of M^*. Because of this, the energy depends only on two parameters ($C_s = Mg_s/m_s$ and $C_v = Mg_v/m_v$) as when no strange particles are included. These parameters are chosen to give nuclear matter saturation at $k_f = 1.3\,{\rm fm}^{-1}$ with a binding energy of 15.75 MeV/A. Their values, denoted as RHAS, are displayed in

	MFT [23]	RHA [15]	RHAS
C_s^2	357.5	228.2	222.0
C_v^2	273.9	147.8	141.7
K_v^{-1}	545	452	446
M^*/M	0.54	0.73	0.74
$E_{\rm vac}/A$	0	5.14	5.28
$E_{\rm svac}/A$	0	0	0.91
$(\bar{p}p + \bar{n}n)_{\rm val}$	.138	.142	.142
$(\bar{p}p + \bar{n}n)_{\rm vac}$	(-.136)	-.015	-.013
$\bar{s}s$	0	0	-.00417

Table 5.5 – Properties of Nuclear Matter. C_s^2 and C_v^2 are adjusted to give a saturation binding energy of 15.75 MeV/A at $k_f = 1.3\,\mathrm{fm}^{-1}$. K_v^{-1} is the resulting compressibility, M^*/M is the nucleon effective mass at saturation, $E_{\rm vac}/A$ is the energy shift of the total vacuum per valence nucleon, $E_{\rm svac}/A$ is the energy shift of the vacuum per nucleon that is due to strange particles, $(\bar{p}p + \bar{n}n)_{\rm val}$ is the scalar density of the valence nucleons, $(\bar{p}p+\bar{n}n)_{\rm vac}$ is the scalar density of the vacuum nucleons, and $\bar{s}s$ is the sum of the scalar densities of all the strange baryons.

Table 5.5 , along with their values when the vacuum is ignored (MFT) and when only the nucleon vacuum is included (RHA).

The inclusion of the strange vacuum has a small effect compared to the effect of the nucleon vacuum. The strange particles increase the energy and scalar density of the vacuum only by about 20%, even though there are three times as many strange particles as nucleons. The effect is small because the effective potential, Eq. (5.31), is of lowest order $(g_{\lambda s}\phi)^5$, and the strange particles are all coupled more weakly than the nucleons. The resulting changes in the adjustable parameters, the compressibility,

effective mass at saturation density, and and vacuum energy per nucleon, which are only a few percent, are even smaller. The reason for this is that a small change in the parameters is enough to adjust the nucleon vacuum so that it can largely cancel out the effects of the strange vacuum. For instance, the nucleon vacuum energy per nucleon decreases by .8 MeV in response to the 0.9 MeV contribution of the strange vacuum. In finite nuclei, however, the derivative terms in the energy density contribute. These terms are of order g^3, suggesting that the strange vacuum will play a greater role.

We calculate finite nuclei by solving the equations of motion for spherically symmetric meson fields, as discussed in the previous section. In addition to the strong interaction ω and σ fields, we also include the Coulomb field coupled to all the charged particles. As is conventional, the mass of the vector meson is taken to be the mass of the omega in free space, $m_v = 783\,\mathrm{MeV}$, while the mass of the scalar meson is picked to give the correct charge radius of ^{40}Ca. Some results are shown in Table 5.6 for ^{16}O and ^{40}Ca.

One needs to increase m_s by 25 MeV from its value with only the nucleon vacuum included. This change occurs because the vector and scalar densities induced in the strange vacuum act as a source of strong interaction mesons and thus modify the valence nuclei. The charge radius of the nucleus itself is determined exclusively by the valence and sea nucleons as the strange vacuum is found to generate a small contribution. After refitting the parameters, the binding energy, charge distribution, and radius of the valence nucleons are all essentially unchanged.

Figure 5.5 shows the effective nucleon density generated by the strange vacuum as well as the nucleon density in the nucleon vacuum for ^{40}Ca. The total effect of the strange vacuum on the vector meson field is roughly half that of the nucleon vacuum.

	MFT	RHA	RHAS
m_s	520	550	575
		^{40}Ca	
RMS	3.48	3.48	3.48
VNR	3.36	3.34	3.34
E/A	6.31	6.71	6.65
$E_{\rm vac}/A$	0	3.33	3.80
$E_{\rm svac}/A$	0	0	0.83
		^{16}O	
RMS	2.75	2.75	2.76
VNR	2.61	2.59	2.595
E/A	4.89	5.47	5.46
$E_{\rm vac}/A$	0	2.90	3.23
$E_{\rm svac}/A$	0	0	0.81

Table 5.6 – Properties of ^{40}Ca and ^{16}O. RMS denotes the root mean square charge radius of the nucleus in fm. and m_s is adjusted to give the correct value of ^{40}Ca. VNR is the rms radius of the valence nucleons in fm. , E/A is the binding energy per nucleon of the nucleus in MeV, and the remaining quantities are defined in Table 5.5.

However, because the density fluctuations in the strange vacuum do not contribute

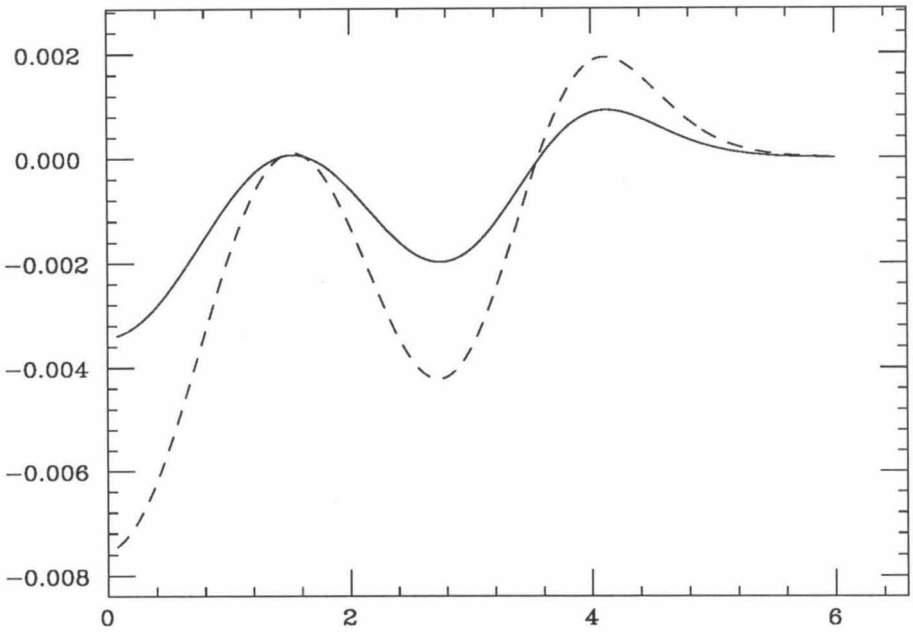

Figure 5.5 – Induced densities in the vacuum for ^{40}Ca. The dashed line is the nucleon density induced in the vacuum and the solid line is the equivalent nucleon density of strange particles induced in the vacuum.

significantly to the charge density, it does not cause the increase in binding energy and shrinkage of the valence nucleon rms radius as is the case with the nucleon vacuum. Figure 5.6 shows the ratio of the strangeness density induced in the vacuum to the total nucleon density for both ^{40}Ca and ^{16}O. It is a significant fraction of the total nucleon density, reaching 4% at its peak densities. These fluctuations will occur in any region of a nucleus where there is varying nucleon density, so this magnitude of strangeness density is predicted to be seen on the surfaces of all nuclei and the interior of light nuclei.

Note that the inclusion of strange particles had no effect on the global nuclear properties, once the scalar mass was retuned. In particular, the fluctuations in the

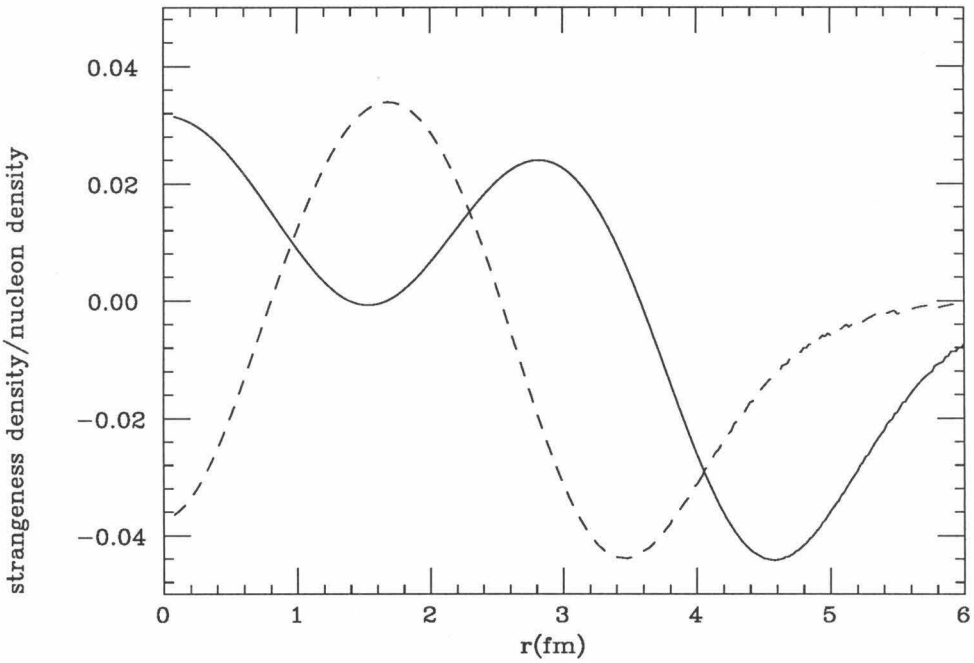

Figure 5.6 – Ratio of strangeness density to nucleon density in ^{40}Ca (solid line) and ^{16}O (dashed line).

nucleon Dirac sea were unaffected. Hence, we might expect that if more particles were inserted into the Dirac sea (such as Δ's), the strangeness fluctuations would also stay about the same. Hence, even if the initial guess about which particles should be included in the Walecka model as "fundamental" is wrong, one would still expect to see these fluctuations. One thing that would affect these fluctuations is the coupling constant of the strange particles to the vector and scalar mesons. According to Eq. (5.33), the densities are roughly proportional to g_λ^2, so they would be reduced by a factor of 4 if the correct value of g_λ turned out to be half as large as we have assumed.

In summary, we have discussed the possibility that the strong fields predicted in relativistic nuclear models could lead to significant polarization of a strange-baryon

component of the vacuum. It is found that although such polarization leads to induced strangeness densities of several percent, it has no significant effect on nuclear structure.

5.4 Experimental Consequences

The vacuum polarization effects discussed in the previous two sections owe their existence to the premise that antihadrons feel a significantly stronger mean field than do hadrons. In this section, I discuss possible experimental tests to check this conjecture and also possible direct experimental signatures of polarization.

The most direct way to try to measure these potentials would be to study the interaction of an antihadron with a nucleus. The easist thing to do would be to scatter antihadrons off the nuclei. Unfortunately, antihadrons annihilate rapidly in a nuclear environment, obscuring any effects that are due to the mean field. A more promising attempt is to observe hadronic pair production in the nuclear environment where the existence of the strong potential lowers the production threshold. The strong potential felt by antinucleons results in a large number of highly bound negative-energy states (binding energies as great as 500 MeV), so that by creating an anti-hadron in one of these states requires only $2M - \epsilon_b$ of energy. Again, this argument is clouded by the fact that the antihadrons annihilate very rapidly, meaning that the hole wavefunction is a very poor representation of the actual antihadron wavefunction. Nonetheless, it is interesting to see whether we can detect these states if infact they exist.

Electroproduction of such pairs is shown in figure 5.8. This process, which is impossible in free space, can occur because the antihadron of fixed energy ,E, is created as a hole in one of the bound negative energy orbitals that has a large momentum spread $u(p)$, while the hadron is created with a fixed momentum p_h (we ignore the small distortion of the final state nucleon wavefunction since it sees a much

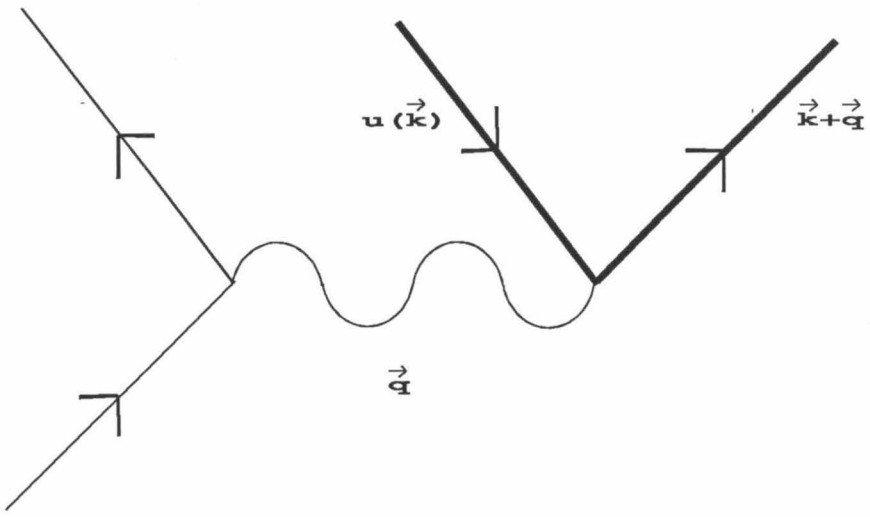

Figure 5.7 – Nucleon pair creation in the presence of a nucleus. A bound anti-nucleon is created with wavefunction u(k) and a free nucleon is created with a three momentum q+k. This process is possible because of the high momentum components of the antinucleon wavefunction.

smaller potential than the anti-nucleon). This process requires the presence of the high momenta components of the wavefunction, with lower momentum required for larger values of p_h. These momenta are constrained by

$$Q^2 = (E + \sqrt{p_h^2 + M^2})^2 - (\mathbf{p} - \mathbf{p}_h)^2 \leq 0, \tag{5.35}$$

where Q^2 is the square of the four-momentum transfer of the spacelike virtual photon. The constraint that the photon be spacelike implies that at threshold ($p_h = 0$),

$$p \geq (E + M) \sim 1500\,\mathrm{MeV}$$

and that for high energy hadron production ($p_h >> M$),

$$p \geq E \sim 500\,\mathrm{MeV}.$$

Unfortunately, the negative energy wavefunctions are suppressed at these high momenta. For example, Figure 5.8 shows the momentum density of the most tightly bound antiproton s state. At threshold, the density is suppressed by $\sim 10^{-6}$ relative to its value at zero momentum, decreasing to 10^{-3} as one goes far above threshold. These cross sections are also suppressed by the nucleon vertex form factor $F(Q^2)$, implying that the most efficient way to observe this is via photoproduction ($Q^2 = 0$).

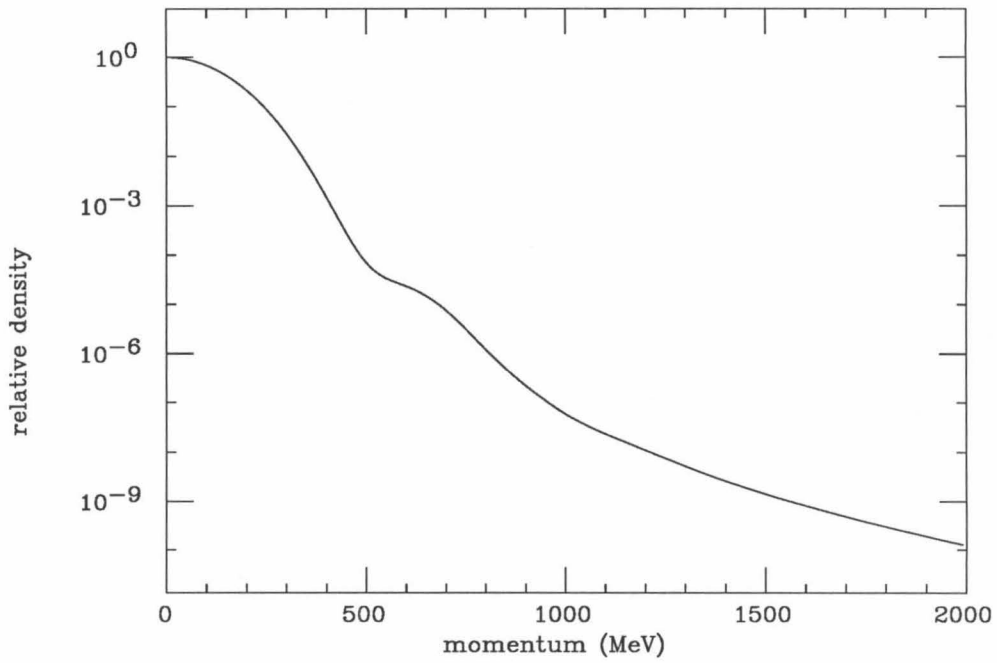

Figure 5.8 – Momentum distribution of the 1s negative-energy state in ^{40}Ca. The curve is normalized to the value at zero momentum.

The cross section for photoproduction of proton-antiproton pairs, assuming that the antiproton wavefunction is described by a Walecka model hole, has been calculated by Jin and Only [32]. They find that because of the large number of bound negative-energy states, the cross-section rises rapidly above the threshold, attaining a value of 5 μb at 300 MeV above threshold for ^{16}O. This is to be compared with the total photon cross section that is around 100 μb, suggesting that such pair-production events could be detectable. Unfortunately, the signature for such events is a slow-moving nucleon and several pions generated by the decay of the created antinucleon. These events can also be generated without using an antihadron just by photoproduction of pions off nucleons. Since the lifetime of the antinucleon is so short, pair production becomes just another channel for producing this final state, making the identification of such a process very unlikely.

Alternatively, we can look for the pair production of strange particles. Here, although the cross section is reduced because the negative-energy states are not as tightly bound, the signature of observing a slowly emitted strange particle would not be as contaminated by background. In conclusion, photoproduction experiments could provide useful constraints on whether or not antibaryons feel such a strong mean field, but only if the "standard" nuclear physics mechanisms that contribute to the background can be well understood. We also note that pickup reactions have also been suggested as a means of probing the Dirac sea [33]. Unfortunately, such processes involve complex reaction dynamics that have yet to be studied.

I now discuss possible ways of detecting the induced scalar and vector polarization charge densities. Since nucleons are already present in the nucleus, to try to isolate certain components of the nucleon density as being due to the Dirac sea would be impossible. However, polarization of the strange vacuum induces scalar and vector

densities that carry a quantum number that is not normally considered to be in the nucleus. This suggests that it might be possible to isolate effects that are due to these densities.

Recall that these densities are defined as being source terms in meson equations; thus they are the relevant quantities that an external meson probe would couple to. One possible probe of this is the K^+ meson. The K^+ meson interacts fairly weakly with nucleons at low energies ($\sigma = 10\,\mathrm{mb}$), heuristically because there are no quarks in the nucleons (uud and udd) for one of the K^+ quarks ($u\bar{s}$) to annihilate with. When interacting with strange particles or antinucleons, however, such annihilation is possible and the K^+ can interact much more strongly. These cross sections should be roughly equal to the $K^- - n$ cross section of 40 mb. By making the assumption that the K^+ interacts with the baryon density fluctuations in the strange vacuum and the negative baryon density fluctuations in the nucleon vacuum with this cross-section then we can make an estimate of the effect of the vacuum on the the $K^+ -$ nucleus cross section.

Figure 5.9 shows the ratio between the local interaction strengths $\sigma\rho$ vs. distance for ^{40}Ca and ^{16}O for the two cases with the cross section calculated as described in the previous paragraph and as calculated just using the $K^+ -$ nucleon cross section. The interaction with the nucleus is increased by up to 20%, giving an average increase of around 10% in regions where the nucleon density is varying. The total cross-section at small energies is given by integrating the local interaction strength. The enhancement of the total cross section is found to be 13% for ^{16}O and 10% for ^{40}Ca. An increase of this order in the $K^+ -^{12} C$ cross section compared to six times the $K^+ - d$ cross section has been observed [34]. Since this nucleus is small, our vacuum fluctuation enhancements would occur throughout the nucleus, giving a total enhancement in

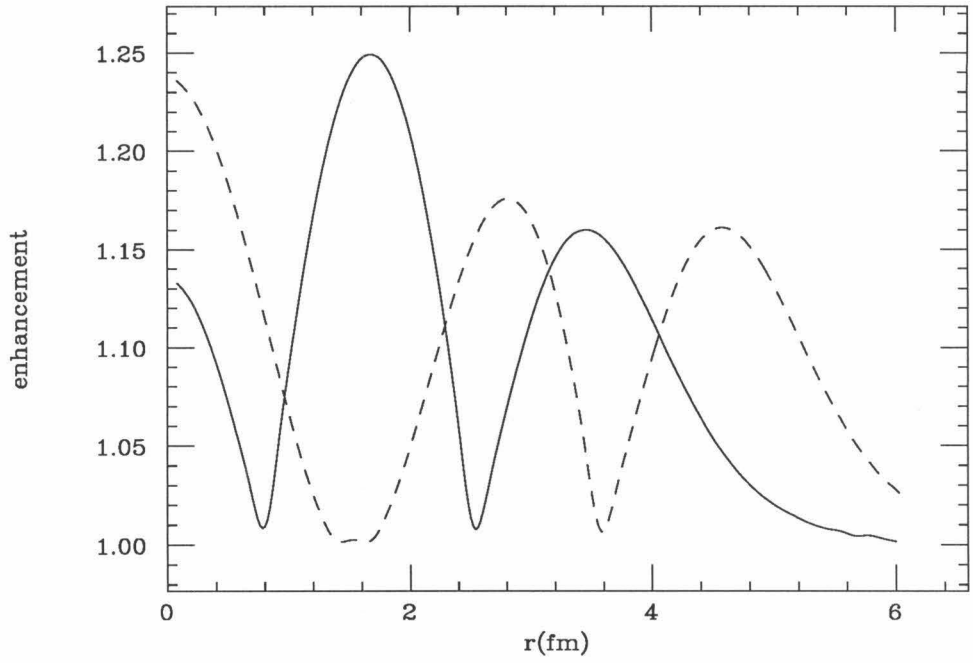

Figure 5.9 – Effect of vacuum polarization on the K^+ – nucleus interaction. The plot shows the ratio of interaction strength of K^+ with various nuclei with the vacuum included to that with the vacuum excluded as a function of distance. The solid line is ^{16}O and the dashed line is ^{40}Ca.

agreement with the measurements. In large nuclei, the only variations in nucleon density occur near the surface, so the cross-section enhancement would occur only on the surface, giving a smaller total enhancement to the cross section. For instance, the enhancement for ^{208}Pb is estimated to be 6.5%. Other possible explanations are that this enhancement is due to a swelling of nucleons in the nucleus [35] or a decrease in the mass of the vector mesons [36]. Both of these effects will be discussed in Section 5.6. It should be pointed out, however, that such a 10% enhancement is within the uncertainties of how well we can understand such reactions within the conventional nuclear picture [37]. Observe that our effect is a surface effect and hence diminishes as one goes to larger nuclei.

In conclusion, we have examined various possible experimental probes of the vacuum phenomena that are motivated by the Walecka model and found no "smoking gun." All known signatures are embedded in a background that is also poorly understood. The best prospects are associated with strange particles, where vacuum polarization can generate about a 10% effect on Kaon scattering.

5.5 Effect of Cutoffs

We have examined the idea that there are strong mean fields in the nucleus, and that these strong mean fields generate significant vacuum polarization. In order to calulate these effects, we have used the Walecka model that asserts that we can model these effects in terms of a renormalizable theory of hadrons. In this section, the validity of a hadronic description of the vacuum is studied. This is done by examining the sensitivity of the vacuum-energy shift to a momentum cutoff in the loop integrals, which is equivalent to a cutoff in the depth of the Dirac sea. A related calculation has been performed by Cohen [38].

For simplicity, we perform the calculations in nuclear matter at a fixed density that is related to the fermi momentum as

$$\rho_b = 4 \int_0^{k_f} \frac{d^3k}{(2\pi)^3} = \frac{2}{3\pi^2} k_f^3 \tag{5.36}$$

and include only nucleons in the Dirac sea. As usual, the energy density per unit volume can be decomposed into three pieces:

$$\varepsilon = \varepsilon_{\text{meson}} + \varepsilon_{\text{valence}} + \varepsilon_{\text{vacuum}}, \tag{5.37}$$

where

$$\varepsilon_{\text{meson}} = \frac{1}{2}\left(\frac{g_\omega}{m_\omega}\right)\rho_b^2 + \frac{1}{2}\left(\frac{m_s}{g_s}\right)^2 (M - M^*)^2, \tag{5.38}$$

$$\varepsilon_{\text{valence}} = \frac{4}{(2\pi)^3}\int_0^{k_f} d^3k\,(k^2+M^{*2})^{1/2} \tag{5.39}$$

and

$$\varepsilon_{\text{vacuum}} = \frac{4}{(2\pi)^3}\int_0^{\Lambda} d^3k\,\left[(k^2+M^2)^{1/2}-(k^2+M^{*2})^{1/2}\right]$$

$$-\alpha\phi-\frac{1}{2}\beta\phi^2-\frac{1}{6}\gamma\phi^3-\frac{1}{24}\lambda\phi^4. \tag{5.40}$$

The latter is the energy density of the vacuum with the sum cutoff at Λ and the four counterterms subtracted. In a uniform system, there are four divergent one-loop diagrams corresponding to one to four external scalar meson lines. The four counterterms are generated to cancel these diagrams at zero external momentum. Specifically,

$$\alpha = g_s\frac{8i}{(2\pi)^4}M\int d^4q\frac{1}{q^2-M^2+i\epsilon} \tag{5.41}$$

and the others can be calculated by differentiating this,

$$\begin{aligned}\beta &= -g_s\frac{d\alpha}{dM}\\ \gamma &= -g_s\frac{d\beta}{dM}\\ \lambda &= -g_s\frac{d\gamma}{dM}.\end{aligned} \tag{5.42}$$

As discussed in Chapter two, implementing the cutoff Λ is equivalent to performing the Feynman integrals exactly over energy and then up to Λ in momentum, resulting in

$$\alpha = \frac{2g_s}{\pi^2}\left[\frac{M\Lambda}{2}\sqrt{\Lambda^2+M^2}-\frac{M^3}{2}\log\frac{\Lambda+\sqrt{\Lambda^2+M^2}}{M}\right]. \tag{5.43}$$

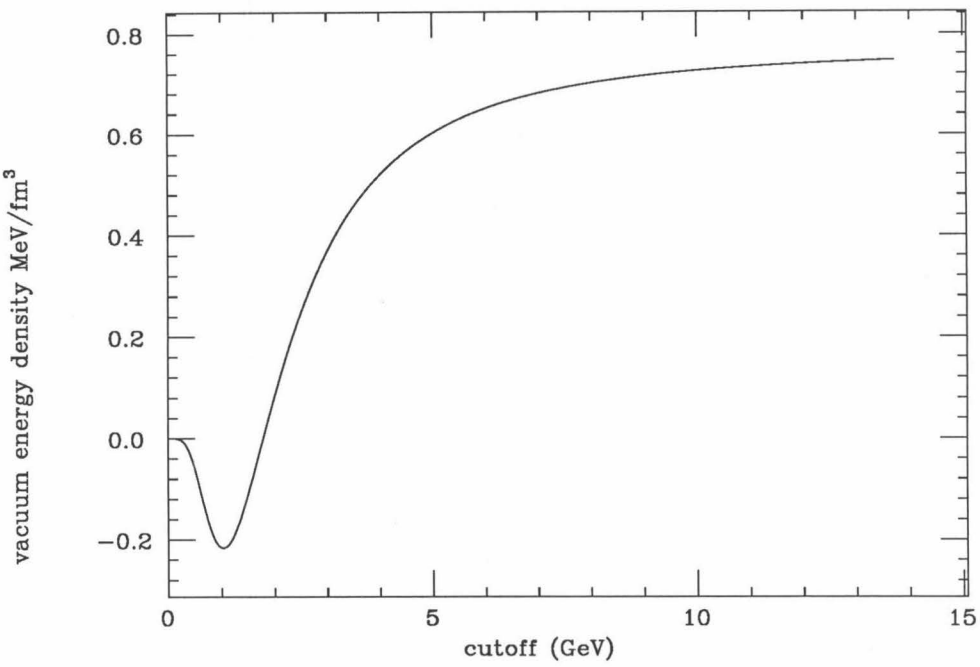

Figure 5.10 – Vacuum energy density in nuclear matter as a function of cutoff for $M^*/M = 0.73$ for the RHA parameter values given in Table 5.5. For cutoffs around 1 GeV, the energy is negative.

By calculating the counterterms in this way we enforce the same renormalization conditions at finite Λ that we enforced in the calculation without a cutoff, namely, that the vacuum does not contribute any terms of order ϕ^4 or less to the effective potential.

Figure 5.11 shows the energy density as a function of cutoff at saturation density with an effective mass of $M^* = 0.73\,M$ and the RHA meson parameters. Observe that the energy does not increase monotonically towards its infinite cutoff value, but initially decreases, reaching a minimum at a cutoff of ~ 1 GeV before rising up to its limiting value at ~ 10 GeV. This strong dependence on cutoffs around the 1 GeV range is not a good sign. In order to examine the effect of this cutoff dependence

properly, we calculate the nuclear matter equation of state and examine the way in which it varies with cutoff.

For a given cutoff and baryon density, the effective mass is determined by minimizing the energy density,

$$\frac{\partial \varepsilon}{\partial M^*}\Big|_{\rho_b} = 0, \tag{5.44}$$

yielding the equation

$$-\left(\frac{m_s}{g_s}\right)^2 (M - M^*) + \frac{4}{(2\pi)^3}\int_0^{k_f} d^3k \, \frac{M^*}{\sqrt{k^2 + M^{*2}}} + \frac{\partial \epsilon_{\text{vacuum}}}{\partial M^*} = 0. \tag{5.45}$$

Solving this equation gives the effective mass as a function of fermi momentum, cutoff, and the scalar-meson parameters,

$$M^* = M^*(k_f, \Lambda, \frac{m_s}{g_s}), \tag{5.46}$$

which eliminates the explicit M^* dependence from the energy density,

$$\varepsilon^0 = \varepsilon^0(k_f, \Lambda, \frac{m_s}{g_s}, \frac{m_\omega}{g_\omega}). \tag{5.47}$$

The values of the meson-mass parameters are fixed by demanding that the equation of state saturate at the correct density with the correct binding energy,

$$\begin{aligned} \frac{\varepsilon^0}{\rho_b}\Big|_{k_f = 1.3\,\text{fm}^{-1}} &= (M - 15.75)\,\text{MeV} \\ \frac{\partial \varepsilon^0/\rho_b}{\partial k_f}\Big|_{k_f = 1.3\,\text{fm}^{-1}} &= 0. \end{aligned} \tag{5.48}$$

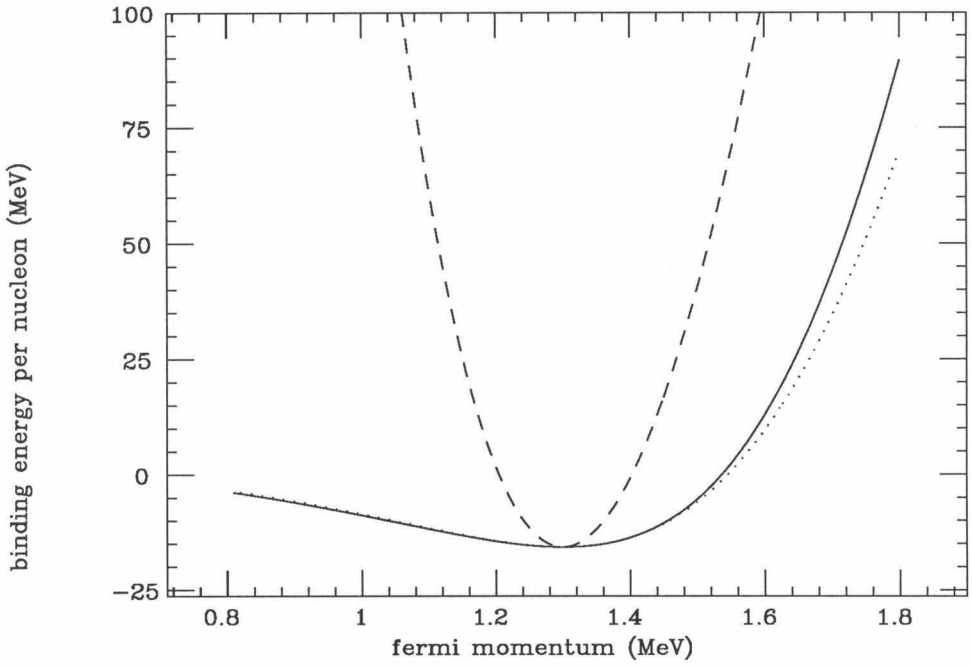

Figure 5.11 – Equation of state of nuclear matter for various cutoffs. The solid line corresponds to a cutoff of 0, the dashed line to a cutoff of 0.8 GeV, and the dotted line to a cutoff of 2.0 GeV.

Figure 5.11 shows the equation of state for several different cutoffs and Table 5.7 tabulates the meson parameters, effective mass at saturation, and incompressibility,

$$K_v^{-1} = k_f^2 \frac{\partial^2(\varepsilon^0/\rho_b)}{\partial k_f^2}\Big|_{k_f=k_f^0} \tag{5.49}$$

for various different cutoffs.

For each cutoff it is possible to adjust the parameters so that nuclear matter saturation is reproduced. For cutoffs ~ 1 GeV the equation of state is very sensitive to the cutoff and far too stiff. In this regime the meson fields are very strong, resulting in a negative effective mass for the nucleons. Also observe that two sets of solutions are determined. One set is continuously connected to the MFT result ($\Lambda = 0$) and

Λ	M^*/M	K_v^{-1}	C_v^2	C_s^2
0	.54	545	274	357
0.11	.54	544	274	357
0.21	.54	542	277	360
0.31	.50	535	300	383
0.35	.43	501	346	433
0.32	-.07	4170	507	609
0.35	-.22	3042	457	538
0.40	-.36	3273	381	393
0.50	-.40	3850	360	274
0.60	-.37	4407	379	222
1.0	-.15	6259	489	230
1.2	-.02	6761	515	309
1.5	.25	4394	446	455
1.7	.49	969	305	382
2.0	.62	564	222	303
4.0	.71	469	161	241
8.0	.73	456	151	231
50.0	.73	451	147	228

Table 5.7 – Properties of nuclear matter as a function of cutoff. The first column gives the cutoff, the second column the effective mass at saturation density, the third column the incompressibility, and the fourth and fifth columns the parameter values required to obtain the fit to nuclear matter saturation.

exists out to $\Lambda = .35\,\mathrm{MeV}$, while the second set is continuously connected to the RHA result ($\Lambda = \infty$) and exists down to $\Lambda = .32\,\mathrm{MeV}$. Hence, not only does the

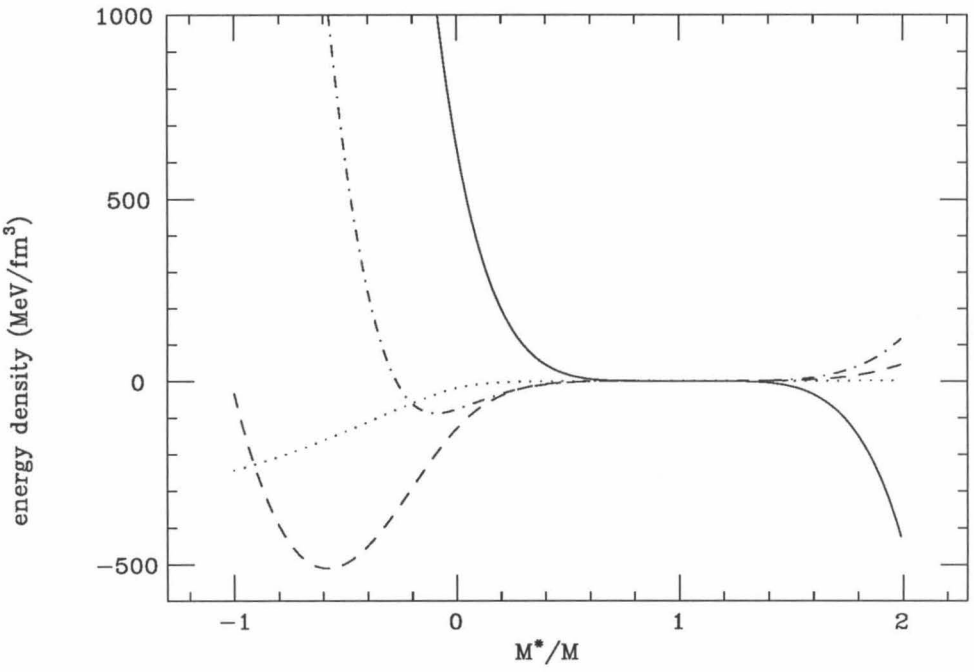

Figure 5.12 – Vacuum contribution to effective potential in the Walecka model for various cutoffs. The dotted line corresponds to $\Lambda = 0.3$ MeV, the dashed line to $\Lambda = 0.7$ MeV, the dot-dashed line to $\Lambda = 1.3$ MeV, and the solid line to the exact result. The potential is evaluated using the RHA parameter set.

energy density not vary monotonically with the cutoff, the MFT and RHA saturation solutions do not even continuously evolve into each other.

This behavior can be understood from the effect of the cutoff on the behavior of $\varepsilon(M^*)$ and $\varepsilon_{\text{vacuum}}(M^*)$. Fig. 5.12 shows $\varepsilon_{\text{vacuum}}(M^*)$ for the RHA meson parameters. For $\Lambda = 0$, $\varepsilon_{\text{vacuum}} = 0$. As the cutoff is increased, a local minimum at negative effective mass is generated that moves towards M as the cutoff is increased. In addition, there is an inflection point at $M^* = M$ the existence of which is forced by the renormalization conditions.

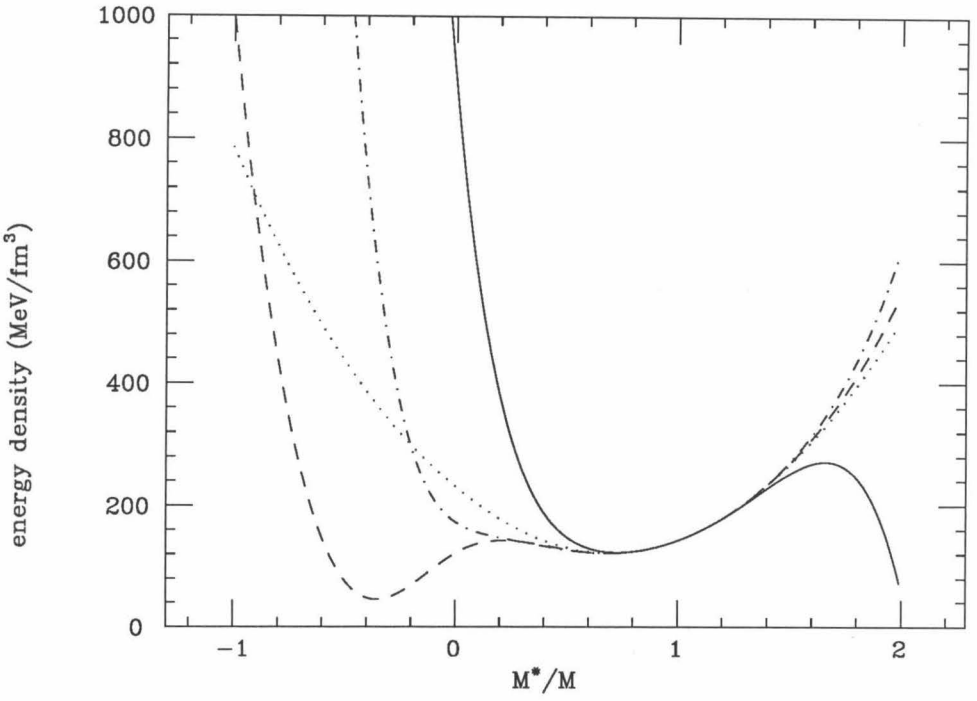

Figure 5.13 – The effective potential at saturation density for various cutoffs. The dotted line corresponds to $\Lambda = 0.3\,\mathrm{MeV}$, the dashed line to $\Lambda = 0.7\,\mathrm{MeV}$, the dot-dashed line to $\Lambda = 1.3\,\mathrm{MeV}$, and the solid line to the exact result. The potential is evaluated using the RHA parameter set.

Figure 5.13 shows the total energy, ε, for a fermi momentum equal to the saturation value. The system wants to minimize this energy. The local minimum induced in the vacuum energy by the cutoff is strong enough that it also generates a local minimum in the total energy. When the total energy is calculated for small cutoffs, this local minimum is far enough removed from M that it plays no role in in determining the minimum of the total energy; the minimum is simply influenced by the behavior around the inflection point. As the cutoff is increased, the local minimum becomes dominant and determines the minimum in the total energy. This is the origin of the two separate solutions tabulated in Table 5.7.

For cutoffs around .35 MeV local minimums in the total energy that is due to both the local minimum in the vacuum energy and the inflection point can be found, yielding two sets of parameters that fit the nuclear matter saturation conditions. These curves are displayed in Figure 5.14.

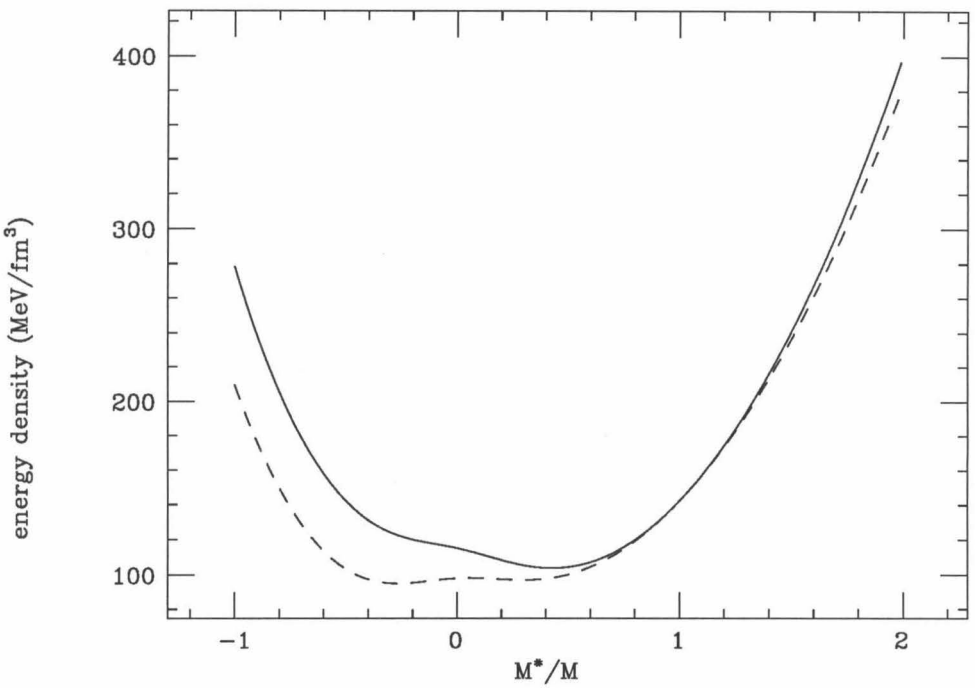

Figure 5.14 – Effective potentials for a cutoff of .35 MeV at saturation density. Two sets of parameters are found such that nuclear-matter saturation is obtained. The dotted line curve is the solution with negative effective mass and evolves continuously to the solution with infinite cutoff, while the solid line curve is the solution with positive effective mass and evolves continuously to the solution with no vacuum energy ($\Lambda = 0$).

The original motivation behind the use of a renormalizable field theory of hadrons was that it would hopefully be insensitive to short-distance physics where it is known to be wrong. This calculation is shows that this insensitivity occurs at the 10 GeV level. Hadronic substructure presumably becomes important at 1 GeV, so this is bad.

However, note that the one-loop calculation involves zero-momentum transfer at the vertex where it is known that a GeV cutoff is appropriate. One cannot say for sure what kind of cutoff, if any, is appropriate for the loop momentum, although various arguments suggest that for composite objects, such a cutoff will exist [39]. In any case, the fact that the Walecka model is displaying sensitivity up to this high energy is not a good sign.

5.6 Vacuum Effects Beyond the Hartree Approximation

Suppose the Dirac sea corrections to the Walecka model are in fact a poor representation of the role played by the vacuum. In this section several different possible vacuum effects that have been suggested are incorporated into the basic Walecka mean-field model in order to ascertain their self-consistent effect on the nuclear model.

The first idea we look at is the possible swelling of nucleons inside the nucleus. This is motivated by the idea that the vacuum that generates the bag pressure is modified in nuclear matter, resulting in a change of the size of the nucleon. Such an effect has been seen in model soliton type calculations [8] .

This effect is built into the Walecka model by assuming that the charge radius of the nucleon is increased by some fraction λ so that

$$\rho^p_{\rm chg}(\mathbf{x}) = \frac{\mu^3}{8\pi}\exp(-\mu|\mathbf{x}|), \tag{5.50}$$

where $\mu = \frac{1}{\lambda}(0.71)^{1/2}$GeV. Such a change in the form factor plays no role in nuclear matter; however, it alters the calculated charge RMS radius of finite nuclei, so the scalar meson mass needs to be readjusted in order to compensate for this. Note that this calculation ignores density dependence of the swelling. Figure 5.15 shows the

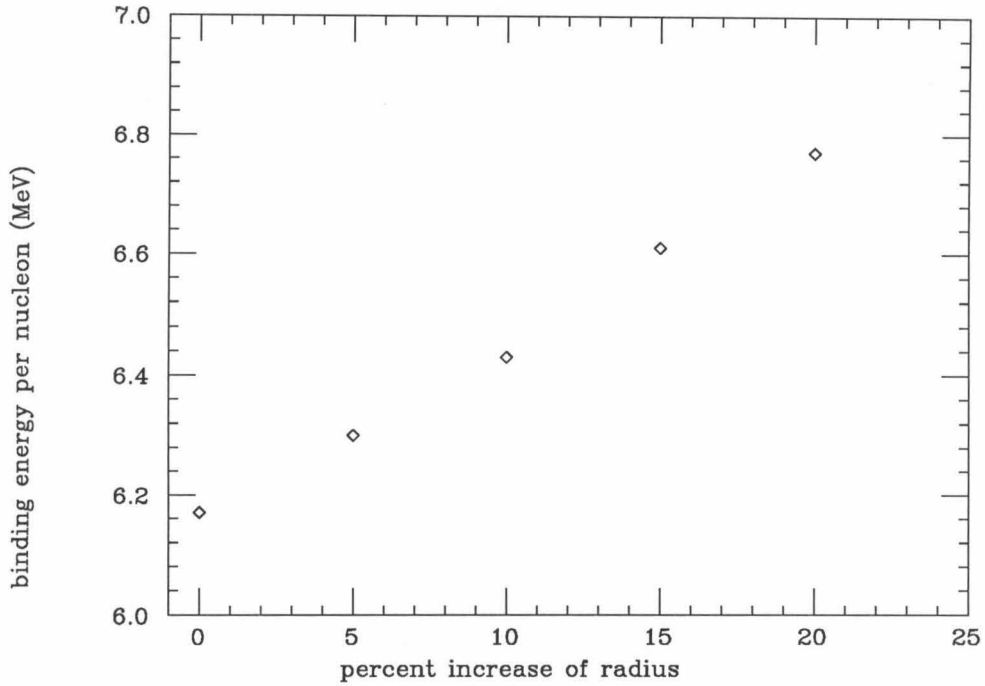

Figure 5.15 – Binding energy per nucleon in ^{40}Ca as a function of percent increase in the proton RMS charge radius.

resulting binding energy per nucleon for ^{40}Ca as a function of the percent increase in the nucleon radius.

The increased RMS radius of the proton forces the valence nucleons to contract in order to get the correct radius for ^{40}Ca, an effect that is analogous to the one seen in vacuum polarization. For the same reason, we get an increased binding energy, although once again with not nearly enough magnitude to give agreement with experiment. A twenty percent increase in the radius gives the same increase in the binding energy as was seen in the one-loop calculations. We can further pursue the analogy by defining an effective nucleon density induced by the swelling as

$$\rho_{\text{eff}}(x) = \rho_{\text{swollen}}(x) - \rho_{\text{normal}}(x), \tag{5.51}$$

where ρ_{swollen} is the nucleon density in the nucleus calculated assuming swelling and ρ_{normal} is the corresponding density in the same nucleus calculated assuming no swelling. This effective density is plotted in Figure 5.16.

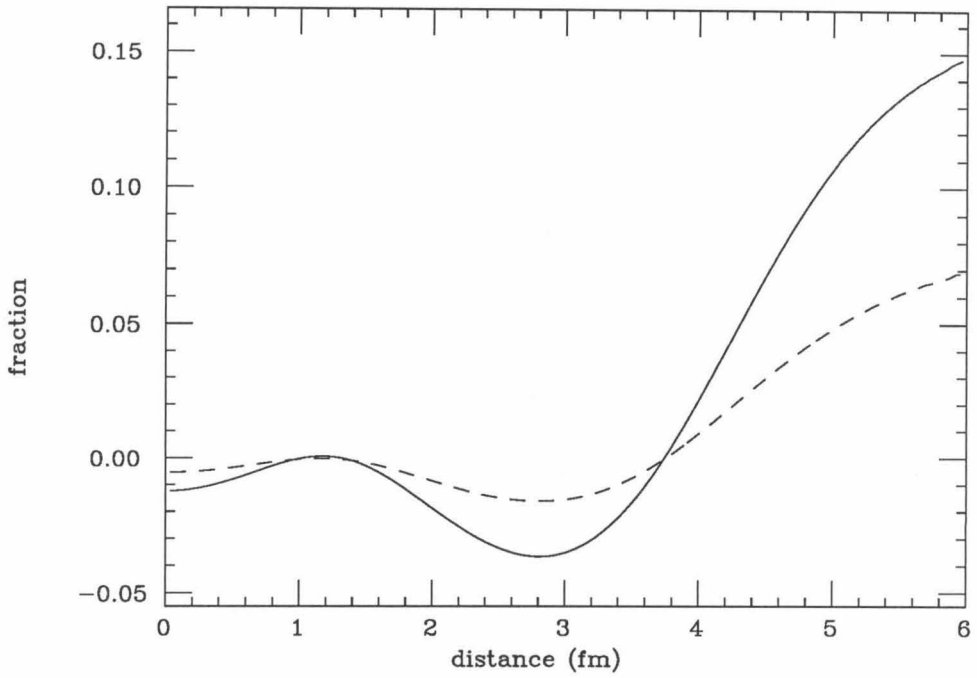

Figure 5.16 – Effective nucleon density induced by increasing the nucleon-charge form factor in medium by 10% (dashed line) and 20% (solid line) for ^{40}Ca. The density is expressed as the fraction of the total nucleon density that it represents.

This graph shows similar fluctuations as seen in the nucleon density induced by vacuum polarization. As was the case with the binding energy, it takes an increase of the nucleon radius of 20% to get the same sized fluctuations as were obtained from the one-loop calculations. This supports the earlier assertion that it was the inducement of baryon density fluctuations that generated the increased binding energy. The large persistent fractional fluctuation seen at large distances is due to our assumption that

the nucleons are swollen everywhere, even when they are far away from the nucleus. That vacuum polarization and nucleon swelling have similar effects also carries over into the dynamics. It is also interesting to note that both effects play similar roles in the response of a nucleus to electron scattering where they tend to suppress the longitudinal response [40].

An alternative vacuum effect is based on the belief that at about ten times nuclear matter density, the strong interaction undergoes a deconfining phase transition that restores chiral symmetry. The spontaneous breaking of chiral symmetry at low densities generates the large constituent quark mass that is responsible for the large masses of the hadrons. As chiral symmetry restoration is approached, the constituent quark mass should decrease, resulting in lighter hadrons. Various simplified models of chiral symmetry-breaking show that masses tend to decrease monotonically towards zero as one increases the fermion density, resulting in the prediction that masses should be 10-20 percent lighter in nuclear matter than in the vacuum [36]. Subsequently, Griegel and Cohen [41]analyzed several schematic models of nuclear matter that incorporated chiral symmetry-breaking and found that the variation of the meson masses was not necessarily monotonic, although the variation of the nucleon mass was monotonic; in fact, the meson masses frequently increased to larger than their vacuum values at nuclear matter density before eventually decreasing to zero at the chiral restoration density.

In any case, the Walecka model knows nothing about chiral symmetry; nonetheless, it does have the desired decrease of the nucleon mass with density that is due to the nucleon coupling to the scalar field, but the corresponding change in meson masses is non-existent. We now incorporate such variations of the meson mass into the Walecka mean-field theory in order to see what effect this has.

For simplicity, we assume that all meson masses scale identically and that this scaling is linear with the nucleon density,

$$m_{s,\omega}(\rho_b) = \left(1 - \lambda\frac{\rho_b}{\rho_0}\right) m^0_{s,\omega}. \tag{5.52}$$

For finite systems, the spatial variation of ρ_b results in a spatially varying mass. This mass modifies the kinetic energy of the mesons to

$$E_{\text{meson}} = \int d^3\mathbf{x}\frac{1}{2}[(\nabla\phi)^2 + m_s^2(\rho_b)\phi^2] - \frac{1}{2}[(\nabla\omega^0)^2 + m_\omega^2(\rho_b)\omega^{0\,2}]. \tag{5.53}$$

If we assume that the valence nucleons are determined by the meson mean fields as usual and then minimize the total energy with respect to the meson fields, we obtain the meson equations of motion,

$$[\nabla^2 - (m_s^0)^2]\phi = -g_s\rho_s^{\text{valence}} + m_s^2[\rho_b(x)]\phi - (m_s^0)^2\phi$$

$$[\nabla^2 - (m_\omega^0)^2]\omega^0 = -g_\omega\rho_b^{\text{valence}} + m_\omega^2[\rho_b(x)]\omega^0 - (m_\omega^0)^2\omega^0. \tag{5.54}$$

For a given λ the parameters are determined in the usual way. Demanding that nuclear matter saturate properly fixes the ratios $m_s(\rho_0)/g_s$ and $m_\omega(\rho_0)/g_\omega$ to the values given in Table 5.5. The mass of the omega meson is constrained to be 783 MeV in free space, so

$$m_\omega(\rho_0) = (1 - \lambda)m_\omega(0), \tag{5.55}$$

λ	$m_s(0)$	$m_s(\rho_0)$	$m_\omega(\rho_0)$	ECA	ϵCA	EO
-0.3	492	640	1018	9.30	50.2	-
-0.2	494	593	940	8.21	48.8	7.15
-0.1	505	555	861	7.19	47.6	5.97
0.0	520	520	783	6.17	46.3	4.77
0.1	544	490	705	5.28	45.3	-
0.2	576	461	626	4.52	44.7	-

Table 5.8 – Effect of density-dependent meson masses on nuclear structure. The first column displays the value of λ. The next three columns show the scalar meson mass in vacuum, the scalar meson mass at nuclear matter density, and the vector meson mass at nuclear matter density. The fifth column (ECA) displays the binding energy per nucleon in ^{40}Ca and the sixth column (ϵCA) is the single particle energy of its $1s$ proton. Finally, the seventh column (EO) shows the binding energy per nucleon in ^{16}O where it was calculated. All quantities in MeV.

thereby determining g_ω. The scalar meson mass is adjusted to give the correct charge radius of ^{40}Ca. Results are shown in Table 5.8.

Observe that increasing the meson masses at nuclear matter density increases the binding, and a twenty percent increase gives binding energies in good agreement with the experimental ones. On the other hand, decreasing the meson masses with density, as would be required by the models of Brown, makes the binding energies worse.

The increase in binding energy is a direct consequence of the density dependence of the mass. If we simply increase all the meson masses (equivalent to simply increasing the omega and rho masses since the scalar mass is a free parameter) by twenty percent, only a small change in the nuclear binding energy is obtained. The density dependence allows the shape of the nuclear surface to change, and with the right

choice of parameter, the surface energy can be reduced to give good binding energies. Figure 5.17 plots the charge densities of the nuclei studied and compares them with those obtained, ignoring medium modifications of mesons. The charge densities have slightly more shell-model fluctuations, but still are reasonable. Hence, density dependence of the meson masses can play a significant role in mean-field phenomenology, and if we assume that they are twenty percent heavier in nuclear matter, then we get good binding energies at the expense of slightly worse densities.

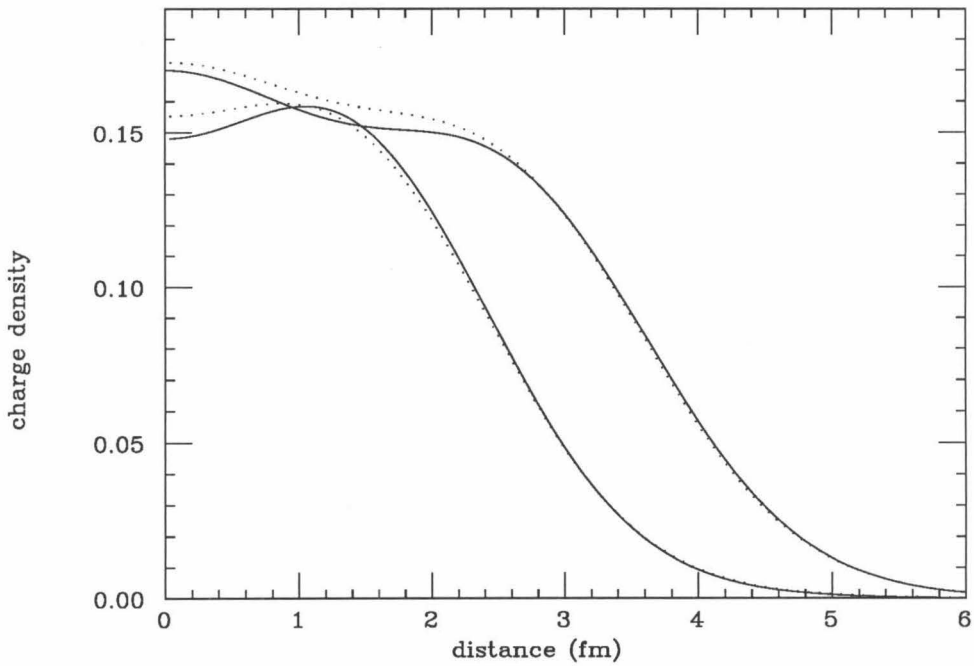

Figure 5.17 – Effect of increased meson mass in medium on charge density. The solid curves are the calculated charge densities assuming that mesons are twenty percent heavier in nuclear matter than in free space, while the dotted curves assume that there is no density dependence in the meson masses.

5.7 Discussion

In this section we summarize the results of this chapter and discuss the subject of "relativistic nuclear models", emphasizing the outstanding problems. We first discuss the status of the Walecka model as a field theory and then of its role as a model of the nucleus. Finally, we discuss issues in phenomenological models.

As a pure field theory, the interesting question is how to compute corrections to the relativistic Hartree approximation when the coupling constants are large. In particular, we need to determine when (if ever) the RHA or MFT is a good approximation to the underlying field theory. It is believed that at large densities the mean-field theory becomes increasingly valid. This suggests that we should be able to generate an expansion in M/k_f that will converge at large k_f. Such an expansion has yet to be developed. The one expansion that has been studied is the loop expansion that adds in perturbative corrections to the non-perturbative mean-field theory result. Such an expansion however is useless for studying theories with strong coupling constants. It is, however, vital that methods for calculating beyond mean field exist for hadronic field theories to have any usefulness.

We have studied the relativistic Hartree approximation to the Walecka model, which attempts to model the nucleus as pointlike nucleons interacting via the exchange of pointlike mesons, as a prospective nuclear model. Even if the model can be shown to support a well defined computational scheme, it also needs to be consistent with the composite nature of the particles involved in order to be a useful description of real nuclei. One consequence of the use of relativistic field theories is that antifermion degrees of freedom are necessarily included. For instance, the one-loop approximation to this model generates the phenomenologically successful mean-field theory along with an additional contribution that is due to vacuum polarization that

we have studied in this chapter. The vacuum polarization effects are large, but is primarily reflected in a redefinition of the bare parameters in the lagrangian. The net effect of the vacuum is to increase slightly the total binding energy of the nucleus at the expense of worse single-particle energies and hence a less successful Dirac phenomenology.

A phenomenological success of the vacuum occurs when the electromagnetic response functions are calculated using the RPA approximation that is basically a linear response theory of the RHA. Here, one gets good agreement for the longitudinal reponse that cannot be obtained without including the vacuum [42]. Hence, the status of one-loop calculations is that the vacuum makes the nuclear structure phenomenology worse, but the electromagnetic response better.

Because of the strong mean field that the negative-energy states feel, the perturbation of the Dirac sea by the mean field extends significantly to a depth of 10 GeV and is critically sensitive at a depth of 1 GeV. This result is worrisome since it suggests that such field theories are incompatible with the finite size of the physical objects that they are attempting to model, in which case the vacuum effects of the Walecka model should not be taken too seriously. If this turns out to be the case, then we could try to build in the finite size effects by inserting form factors into the model. In addition to vertex form factors that are reasonably well understood, there can also be other form factors such as form factors that suppress off-shell nucleon propagation and form factors that suppress negative energy states. The study of these kinds of form factors is just beginning. It should also be noted that the introduction of these form factors into the lagrangian makes the theory non-renormalizable, and how to develop a well-defined computational scheme is not clear, in particular, what diagrams

are double counting effects in the form factor and what, if anything, corresponds to actual physics.

Finally, another problem facing hadronic field theories is what degrees of freedom to include. If we go beyond the mean-field theory, then all particles contribute. For instance, the pion and delta resonance will play large roles. The Walecka model must be able to incorporate these particles in order to describe corrections to the mean-field theory correctly (assuming a scheme to calculate these corrections is developed) and also have a criterion for deciding what particles actually should be included.

The alternate approach to using the Walecka model is simply to build effective lagrangians that are designed to be used at the mean-field level (since this is the one calculation we know how to do) with all other physical effects built into the terms in the Lagrangian. The hope is that with a fairly small number of terms one can develop a robust Lagrangian. This program has been very sucessful in describing ground-state nuclear structure, where a Lagrangian of the form

$$\mathcal{L}_{\text{eff}} = \mathcal{L}_{\text{Walecka}} - \gamma\phi^3 - \lambda\phi^4 \tag{5.56}$$

has been shown to yield a description of spherical and deformed nuclei comparable to that obtained by using the non-relativisitic effective Skyrme-type interactions [25]. The only problem with this Lagrangian is that $\lambda < 0$, which means that the energy is unbounded from below. For such Lagrangians to be most useful, they need to describe a wide range of phenomena. It would be interesting to study the electromagnetic response in this model to see if the non-linear meson terms can generate realistic response functions.

One defect of the above effective Lagrangian is that it attributes all of the baryon density to the occupied valence Hartree orbitals. Many body effects beyond the

Hartree level will induce additional local baryon density. As we saw for the case of vacuum fluctuations, this effect can be modeled by adding vector gradient terms to the effective Lagrangian and these terms can have a significant effect on the binding energy of the nuclei.

This completes our summary of the current status of the attempt to construct hadronic models applicable to intermediate-energy, nuclear physics. Clearly, there is much work left to do.

Appendix A
Renormalization Details

This appendix discusses the one-loop renormalization of the various Lagrangians used in this thesis. The basic method of renormalization is reviewed in [2].

A.1 Self-interacting Scalar Bosons in $1+1$ Dimensions

Consider a scalar field in $1+1$ dimensions described by a Lagrangian,

$$\mathcal{L} = \frac{1}{2}\partial_\mu\phi\partial^\mu\phi - V(\phi) + \mathcal{L}_{\rm ct} \qquad (A.1)$$

where $V(\phi)$ is an arbitrary potential that is bounded below. In $1+1$ dimensions the scalar field is dimensionless, so a polynomial of any order in ϕ is renormalizable, hence the form of V(ϕ) is unconstrained. Suppose the classical vacuum corresponds to $\phi = \phi_v$, where

$$V'(\phi_v) = 0 \text{ and } V''(\phi_v) > 0. \qquad (A.2)$$

Expanding about this value gives

$$V(\phi) = V(\phi_v) + \frac{1}{2}V''(\phi_v)\eta^2 + \frac{1}{3!}V'''(\phi_v)\eta^3 + \cdots \qquad (A.3)$$

Hence, quantization about ϕ_v results in Feynman rules involving the propagator

$$\Delta^0(k) = \frac{1}{k^2 - V''(\phi_v) + i\epsilon} \qquad (A.4)$$

and an nth order ($n > 2$) vertex with coupling constant α^n, where

$$\alpha^n = -V^{(n)}(\phi_v). \tag{A.5}$$

By power counting, the only divergent one-loop graphs are those with one external vertex. The one-loop diagram with n external legs emerging from a single vertex is equal to

$$-iV^{(n+2)}(\phi_v)\xi,$$

where

$$\xi = \frac{1}{2}\int \frac{d^2k}{(2\pi)^2}\frac{i}{k^2 - V''(\phi_v) + i\epsilon}. \tag{A.6}$$

Hence, $\mathcal{L}_{\rm ct}$ can be written as

$$\mathcal{L}_{\rm ct} = \xi \sum_{n>0} V^{(n+2)}(\phi_v)\frac{\eta^n}{n!} = \xi\left[V''(\phi) - V''(\phi_v)\right], \tag{A.7}$$

where we have chosen the counterterms to cancel the one-loop contribution at zero four momentum on the external legs (i.e., so that the coupling constants written in the bare Lagrangian correspond to the physical coupling constants at zero external momentum) as shown in Figure A.1. An alternative is to cancel the one-loop contribution at external momentum on the scalar meson mass scale, in which case the coupling constants in the bare Lagrangian are equal to the ones measured in meson-meson scattering.

Finally, we evaluate ξ by performing the energy integral exactly and by cutting off the momentum integral at Λ, giving

$$\xi = \frac{1}{2}\int_{-\Lambda}^{\Lambda}\frac{dk}{2\pi}\int_{-\infty}^{\infty}\frac{dk^0}{2\pi}\frac{i}{k^{0\,2} - k^2 - V''(\phi_v) + i\epsilon}. \tag{A.8}$$

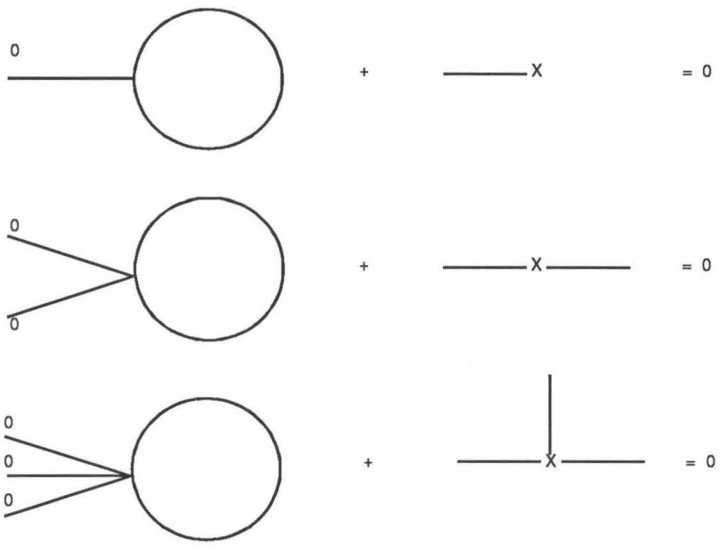

Figure A.1 – Divergent one-loop diagrams in 1+1 dimensional boson theories. The solid lines denote boson propagators and all diagrams with one external leg are divergent. All one-loop diagrams with one attached vertex are divergent. Shown are divergent diagrams with a vertex corresponding to three, four, and five external legs. In general, the 1+1 dimensional boson Lagrangian can have vertices corresponding to any number of external legs that generate an infinite one-loop diagram with two less external legs. The counterterms are chosen to cancel the diagrams at zero external four momenta.

The energy integral is easily evaluated by deforming the energy integration contour to go along the imaginary axis, resulting in

$$\xi = \frac{1}{4\pi}\int_0^\Lambda \frac{dk}{\sqrt{k^2 + V''(\phi_v)}} = \frac{1}{4\pi}\log\left[\frac{\Lambda + \sqrt{\Lambda^2 + V''(\phi_v)}}{\sqrt{V''(\phi_v)}}\right]. \qquad (A.9)$$

Since the only parts of the counterterm that matter are the parts that diverge or stay finite as $\Lambda \to \infty$ and

$$\log\left[\frac{\Lambda + \sqrt{\Lambda^2 + V''(\phi_v)}}{\sqrt{V''(\phi_v)}}\right] = \log\left[\frac{2\Lambda}{\sqrt{V''(\phi_v)}}\right] + \frac{1}{4}\frac{V''(\phi_v)}{\Lambda^2} + \mathcal{O}(\Lambda^{-4}), \qquad (A.10)$$

we can equivalently write the counterterm as

$$\xi = \frac{1}{8\pi} \log \left[\frac{4\Lambda^2}{V''(\phi_v)} \right]. \tag{A.11}$$

A.2 Self-interacting Bosons in $3+1$ Dimensions

Now consider the one-boson-loop diagrams for the Lagrangian (A.1) in $3+1$ dimensions. The propagators and vertices are as given in the previous section. Note that now $V(\phi)$ can contain only terms up to order ϕ^4 in order to be renormalizable. The divergent diagrams are the boson-loops with one (quadratically divergent) and two (logarithmically divergent) vertices. We write the counterterm Lagrangian as

$$\mathcal{L}_{\rm ct} = \mathcal{L}_{\rm ct}^{(1)} + \mathcal{L}_{\rm ct}^{(2)},$$

where $\mathcal{L}_{\rm ct}^{(1)}$ renormalizes the diagrams with one vertex and $\mathcal{L}_{\rm ct}^{(2)}$ renormalizes the diagrams with two vertices.

The diagrams with one vertex are calculated as in the previous section and are renormalized by

$$\mathcal{L}_{\rm ct}^{(1)} = \xi^{(1)} \left[V''(\phi) - V''(\phi_v) \right], \tag{A.12}$$

where

$$\xi^{(1)} = \frac{1}{2} \int \frac{d^4k}{(2\pi)^4} \frac{i}{k^2 - V''(\phi_v) + i\epsilon}. \tag{A.13}$$

The diagram with m external legs at one vertex and n external legs at the other is equal to

$$-iV^{(n+2)}(\phi_v) V^{(m+2)}(\phi_v) \frac{(n+m)!}{n!m!} \xi^{(2)}, \tag{A.14}$$

where

$$\xi^{(2)} = \frac{1}{2}\int \frac{d^4k}{(2\pi)^4}\frac{i}{(k^2 - V''(\phi_v) + i\epsilon)^2}. \tag{A.15}$$

Hence, $\mathcal{L}_{\rm ct}^{(2)}$ can be written as

$$\begin{aligned}
\mathcal{L}_{\rm ct}^{(2)} =& \frac{1}{2}\xi^{(2)} \sum_{l>0} \sum_{m+n=l} V^{(n+2)}(\phi_v) V^{(m+2)}(\phi_v) \frac{(n+m)!}{n!m!}\frac{\eta^l}{l!} \\
=& \frac{1}{2}\xi^{(2)} \sum_{l>0} \sum_{m+n=l} V^{(n+2)}(\phi_v) \frac{\eta^n}{n!} V^{(m+2)}(\phi_v) \frac{\eta^m}{m!} \\
=& \frac{1}{2}\xi^{(2)} \left[V''(\phi) - V''(\phi_v)\right]^2 .
\end{aligned} \tag{A.16}$$

Explicitly evaluating $\xi^{(1)}$ and $\xi^{(2)}$ in terms of a three-momentum cutoff Λ gives

$$\xi^{(1)} = \frac{1}{4}\int_0^\Lambda \frac{d^3k}{(2\pi)^3}\frac{1}{\sqrt{k^2 + V''(\phi_v)}} \tag{A.17}$$

and

$$\xi^{(2)} = -\frac{1}{8}\int_0^\Lambda \frac{d^3k}{(2\pi)^3}\frac{1}{(k^2 + V''(\phi_v))^{3/2}}. \tag{A.18}$$

A.3 Fermions in $1+1$ Dimensions

Consider a fermion with mass M coupled to a scalar field in $1+1$ dimensions via the Lagrangian,

$$\mathcal{L} = \bar{\psi}(i\gamma^\mu \partial_\mu - M + g_s\phi)\psi + \mathcal{L}_\phi + \mathcal{L}_{ct} \tag{A.19}$$

where $\mathcal{L}_\phi$ is the boson Lagrangian treated in the previous section and $\mathcal{L}_{ct}$ refers to the necessary one-fermion-loop counterterms. In this theory, the fermion propagator is

$$G^0(k) = \frac{\gamma_\mu k^\mu + M}{k^2 - M^2 + i\epsilon} \tag{A.20}$$

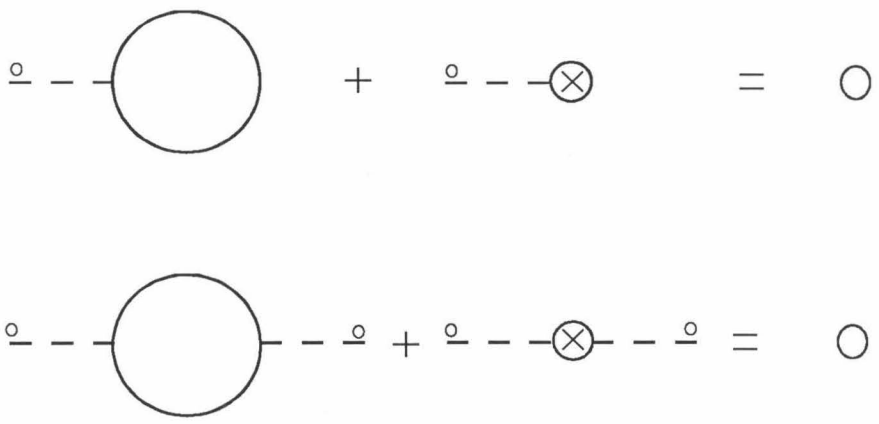

Figure A.2 – Divergent one-loop diagrams in 1+1 dimensional fermion theories. Solid lines represent the fermions and dashed lines the scalar meson. The diagrams are renormalized at zero external momentum.

and there is a fermion coupling to a single scalar field line with strength g_s. By power counting, the one-fermion-loop diagrams with one and two external meson lines are divergent, as shown in Fig. A.2

The diagram with one external meson line is $-i\alpha^1$, where

$$\alpha^1 = g_s \int \frac{d^2k}{(2\pi)^2}\, i\, tr\, \frac{\gamma_\mu k^\mu + M}{k^2 - m^2 + i\epsilon}. \qquad (A.21)$$

Evaluating the trace gives

$$\alpha^1 = g_s \int \frac{d^2k}{(2\pi)^2}\, 2i \frac{M}{k^2 - m^2 + i\epsilon}, \qquad (A.22)$$

and performing the resulting integral exactly over energy and up to a cutoff Λ over momentum gives (see the previous section for details)

$$\alpha^1 = \frac{Mg_s}{\pi}\int_0^\Lambda \frac{dk}{\sqrt{k^2+M^2}}. \tag{A.23}$$

The divergence in the diagram with two external legs is independent of the momentum flow through it in $1+1$ dimensions, so we simply need to evaluate it at zero external momentum. It equals $-i\alpha^2$, where

$$\alpha^2 = -ig_s^2\int \frac{d^2k}{(2\pi)^2}\, tr\, \frac{(\gamma_\mu k^\mu + M)(\gamma_\nu k^\nu + M)}{(k^2 - M^2 + i\epsilon)^2}. \tag{A.24}$$

Performing the trace gives

$$\alpha^2 = -ig_s^2\int \frac{d^2k}{(2\pi)^2}\frac{2(k^2+M^2)}{(k^2-m^2+i\epsilon)^2} \tag{A.25}$$

and evaluating the integral in the usual way,

$$\alpha^2 = -\frac{g_s^2}{\pi}\int_0^\Lambda \frac{dk}{\sqrt{k^2+M^2}} + \frac{g_s^2}{\pi}\int_0^\Lambda \frac{dkM^2}{(k^2+M^2)^{3/2}}. \tag{A.26}$$

We pick the counterterms to cancel the one-loop diagrams at zero external momentum, resulting in

$$\mathcal{L}_{\rm ct} = \alpha^1\phi + \frac{1}{2}\alpha^2\phi^2. \tag{A.27}$$

Observe that

$$\alpha^2 = -g_s\frac{d\alpha^1}{dM}, \tag{A.28}$$

a fact that follows simply from the identity

$$\frac{\partial G^0(k)}{\partial M} = \left[G^0(k)\right]^2. \tag{A.29}$$

The counterterm (A.18) can be written in a more convenient form by explicitly evaluating the integrals for the counterterm coefficients. Following the previous section, we find that the coefficients can be written as

$$\begin{aligned} \alpha^1 =& \frac{g_s M}{2\pi} \log\left(\frac{4\Lambda^2}{M^2}\right) \\ \alpha^2 =& -\frac{g_s^2}{2\pi} \log\left(\frac{4\Lambda^2}{M^2}\right), \end{aligned} \tag{A.30}$$

implying

$$\begin{aligned} \mathcal{L}_{\rm ct} =& -\frac{1}{4\pi} \log\left(\frac{4\Lambda^2}{M^2}\right)(g_s^2\phi^2 - 2g_s M\phi) \\ =& -\frac{1}{4\pi} \log\left(\frac{4\Lambda^2}{M^2}\right)((M^*)^2 - M^2), \end{aligned} \tag{A.31}$$

where $M^* = M - g_s\phi$.

A.4 Fermions in $3+1$ Dimensions

In this section we consider fermions coupled to a scalar and vector field in $3+1$ dimensions. The Lagrangian is

$$\begin{aligned} \mathcal{L} =& \bar{\psi}(i\gamma^\mu\partial_\mu - g_v\gamma^\mu V_\mu - M + g_s\phi)\psi \\ &+ \frac{1}{2}(\partial_\mu\phi\partial^\mu\phi - m_s^2\phi^2) - \frac{1}{4}F_{\mu\nu}F^{\mu\nu} + \frac{1}{2}m_v^2 V^\mu V_\mu + \mathcal{L}_{\rm ct}, \end{aligned} \tag{A.32}$$

where $F_{\mu\nu} = \partial_\mu F_\nu - \partial_\nu F_\mu$, and $\mathcal{L}_{\rm ct}$ is the counterterm Lagrangian. The specific renormalization of this Lagrangian is described in [26]. The Feynman diagrams in this theory consist of the usual fermion propagator plus fermions coupled to a single

scalar line with strength g_s and to a single vector line with strength $-g_v\gamma^\mu$. The scalar meson propagator is as given previously, while the vector meson propagator is

$$D^0_{\mu\nu}(k) = \left(\frac{k_\mu k_\nu}{m_v^2} - g_{\mu\nu}\right)\frac{-1}{k^2 - m_v^2 + i\epsilon}. \qquad (A.33)$$

Because the fermion-vector meson vertex conserves fermion number, only the $g_{\mu\nu}$ term in the propagator contributes.

There are five divergent one-loop diagrams in this theory: one fermion loop with 1-4 external scalar meson legs and one fermion loop with two external vector meson legs, as shown in Figure A.3. In this section, we evaluate the counterterms assuming only one species of fermions; if there are in fact N (as in the Walecka model where $N = 2$), then all the counterterms in this section should be multiplied by N. In practice, sometimes we will be dealing with parameters defined at zero external momentum and at other times with parameters defined on mass shell. We explicitly evaluate all these counterterms in terms of parameters defined at zero external momentum and then show how to compute these parameters in terms of on-shell quantities when needed.

The infinities in the 1,3, and 4 scalar-meson legs are all independent of the external momentum going through the legs, while the diagram with two scalar-meson legs has a divergence that depends quadratically on the external momentum. The diagrams with vector external legs are identically zero when the external legs have no momentum, but the diagram with two legs has a divergence that is quadratic in the momentum. Hence, it follows that the counterterm will be of the form

$$\mathcal{L}_{\rm ct} = \alpha_1\phi + \frac{1}{2}\alpha_2\phi^2 + \frac{1}{3!}\alpha_3\phi^3 + \frac{1}{4!}\alpha_4\phi^4 + \frac{1}{2}\beta_2^\phi\partial_\mu\phi\partial^\mu\phi - \frac{1}{4}\beta_2^v F^{\mu\nu}F_{\mu\nu}. \qquad (A.34)$$

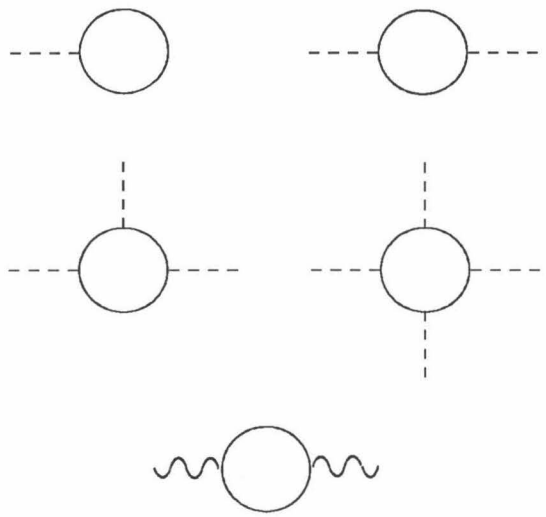

Figure A.3 – Divergent one-loop diagrams in the Walecka model. Solid lines represent the fermion propagator, dashed lines the scalar meson propagator, and wavy lines the vector meson propagator.

We now evaluate these coefficients. Consider first the diagrams with 1-4 scalar meson legs at zero external momentum. By our definitions in the expression for the counterterm, if we renormalize at zero momentum, the value of the diagram with n external lines is $-i\alpha_n$, where

$$\alpha_n = i(-1)^n g_s^n (n-1)! \int \frac{d^4k}{(2\pi)^4} tr\ \left[G^0(k)\right]^n . \qquad (A.35)$$

Equation (A.20) implies

$$\frac{\partial \left[G^0(k)\right]^n}{\partial M} = n\left[G^0(k)\right]^{n+1} , \qquad (A.36)$$

giving the general result

$$\alpha_n = -g_s \frac{d\alpha_{n-1}}{dM}. \tag{A.37}$$

The evaluation of α^1 proceeds as in Section A.2. The Feynman rules give

$$\alpha_1 = g_s \int \frac{d^4k}{(2\pi)^4}\, i\, tr\, \frac{\gamma_\mu k^\mu + M}{k^2 - m^2 + i\epsilon} \tag{A.38}$$

and is explicitly evaluated in terms of a three-momentum cutoff as

$$\alpha_1 = \frac{Mg_s}{\pi^2}\int_0^\Lambda dq\, \frac{q^2}{\sqrt{q^2+M^2}} = \frac{Mg_s}{2\pi^2}\left[\Lambda\sqrt{\Lambda^2+M^2} - M^2 \log\left(\frac{\Lambda+\sqrt{\Lambda^2+M^2}}{M}\right)\right]. \tag{A.39}$$

Observe that this expression is only quadratically and logarithmically divergent. The remaining three zero-momentum counterterms are determined by differentiating α_1 and are listed here for reference:

$$\begin{aligned}
\alpha_2 =& -\frac{g_s^2}{2\pi^2}\Big[\frac{\Lambda^3+2M^2\Lambda}{\sqrt{\Lambda^2+M^2}} - \frac{M^4}{\Lambda^2+M^2+\Lambda\sqrt{\Lambda^2+M^2}} \\
&+ M^2 - 3M^2\log\big(\frac{\Lambda+\sqrt{\Lambda^2+M^2}}{M}\big)\Big] \\
\alpha_3 =& \frac{g_s^3}{2\pi^2}\Big[\frac{2M^3\Lambda+3M\Lambda^3}{(\Lambda^2+M^2)^{3/2}} + 5M - 6M\log\big(\frac{\Lambda+\sqrt{\Lambda^2+M^2}}{M}\big) \\
&- \frac{7M^3}{\Lambda^2+M^2+\Lambda\sqrt{\Lambda^2+M^2}} + \frac{M^4}{(\Lambda^2+M^2+\lambda\sqrt{\Lambda^2+M^2})^2}\big(2M + \frac{\Lambda M}{\sqrt{\Lambda^2+M^2}}\big)\Big] \\
\alpha_4 =& -\frac{g_s^4}{2\pi^2}\Big[\frac{6M^2\Lambda+3\lambda^3}{(\Lambda^2+M^2)^{3/2}} - \frac{3(2M^3\Lambda+3M\Lambda^3)M}{(\Lambda^2+M^2)^{5/2}} + 11 \\
&- 6\log\big(\frac{\Lambda+\sqrt{\Lambda^2+M^2}}{M}\big) - \frac{27M^2}{\Lambda^2+M^2+\Lambda\sqrt{\Lambda^2+M^2}} \\
&\frac{1}{(\Lambda^2+M^2+\Lambda\sqrt{\Lambda^2+M^2}}\big(24M^4 + \frac{12\Lambda M^4}{\sqrt{\Lambda^2+M^2}} - \frac{\Lambda M^6}{(\Lambda^2+M^2)^{3/2}}\big) \\
&- \frac{2M^4}{(\Lambda^2+M^2+\Lambda\sqrt{\Lambda^2+M^2})^3}\big(2M + \frac{\Lambda M}{\sqrt{\Lambda^2+M^2}}\big)^2\Big].
\end{aligned} \tag{A.40}$$

We now evaluate the counterterms that are quadratic in the external momentum. First consider the one-fermion-loop diagram with two external scalar lines each carrying a four momentum k_μ (the vacuum polarization correction to the meson propagator of momentum k_μ) that is equal to $-i\gamma$, where

$$\gamma = -ig_s^2 \int \frac{d^4q}{(2\pi)^4}\, tr\, \frac{\gamma^\mu(k_\mu + q_\mu) + M}{(k+q)^2 - M^2 + i\epsilon} \frac{\gamma^\mu q_\mu + M}{q^2 - M^2 + i\epsilon}. \tag{A.41}$$

Evaluating the traces and using the standard Feynman parameterization gives

$$\gamma(k^2) = -i4g_s^2 \int \frac{d^4q}{(2\pi)^4} \int_0^1 dx\, \frac{-k^2x(1-x) + q^2 + M^2}{\left[q^2 - M^2 + k^2x(1-x)\right]^2}. \tag{A.42}$$

Taylor expanding this about $k^2 = 0$ gives

$$\gamma(k) = \alpha_2 + \beta_2^\phi \frac{\partial\gamma}{\partial k^2}\Big|_{k^2=0} k^2 + \mathcal{O}(k^4), \tag{A.43}$$

where the order k^4 and higher terms are all finite and

$$\beta_2^\phi = i\frac{8}{3}g_s^2 \int \frac{d^4q}{(2\pi)^4} \frac{1}{q^2 - M^{2^2}} \Big[1 + \frac{2(q^2 + M^2)}{q^2 - M^2}\Big]. \tag{A.44}$$

Similarly the fermion-loop diagram with two external vector lines each carrying a four-momentum k_μ is equal to $-i\gamma^{\mu\nu}$, where

$$\gamma^{\mu\nu} = -ig_v^2 \int \frac{d^4q}{(2\pi)^4} \mathrm{tr}\gamma^\mu \frac{\gamma_\alpha(k_\alpha + q_\alpha) + M}{(k+q)^2 - M^2} \gamma^\nu \frac{\gamma^\alpha q_\alpha + M}{q^2 - M^2}. \tag{A.45}$$

Evaluating the traces, introducing the standard x parameter, and shifting variables result in

$$\gamma^{\mu\nu} = -ig_v^2 \int \frac{d^4q}{(2\pi)^4} \int_0^1 dx\, \frac{-2x(1-x)}{(q^2 - M^2 + k^2x(1-x))^2} [k^\mu k^\nu - g^{\mu\nu}k^2]. \tag{A.46}$$

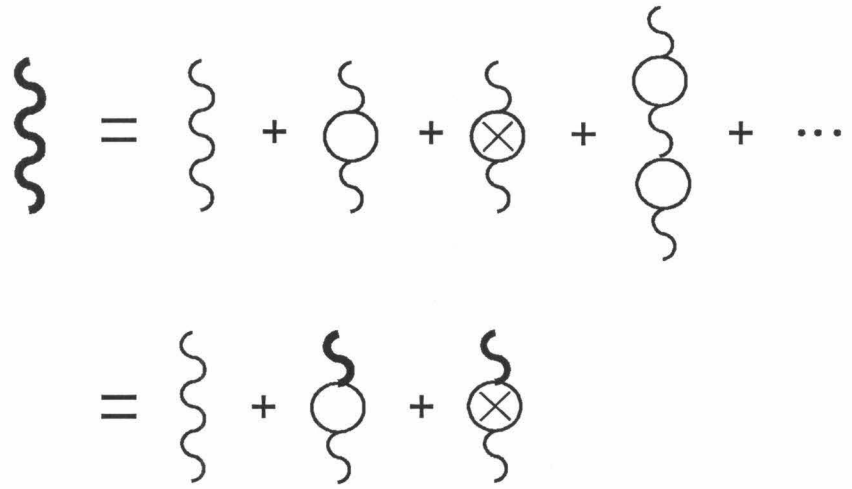

Figure A.4 – Dyson equation for the one-loop vector meson propagator. The loops denote fermion-loops, the dark wavy lines the one-loop vector meson propagator, and the light wavy lines the bare vector meson propagator. The x represents the one-loop counterterm given in Equation A.23.

Observe that there is no contribution at $k = 0$ and that the value of the required counterterm is

$$\beta_2^v = i8g_v^2 \int \frac{d^4q}{(2\pi)^4} \int_0^1 dx \frac{x(1-x)}{(q^2 - M^2)^2}. \qquad (A.47)$$

This completes the calculation of the five counterterms that are needed at the one-fermion-loop level. The counterterms have been chosen to cancel all the one-loop diagrams at zero external momentum so that all the coupling constants and masses correspond to the coefficients that are obtained in the lowest-order terms of a Taylor series expansion of the effective action. Sometimes, however, it is necessary to pick

these parameters to get some desired on-shell quantity. In this thesis the only such quantity we will be interested in is the physical mass of the vector meson. The mass of the physical vector meson corresponds to the pole of the vector meson propagator. At the one-fermion-loop level, the vector meson propagator is evaluated by summing up all the ring diagrams, as shown in Fig. A.4, which is equivalent to the equation

$$iD^1_{\mu\nu}(k) = iD^0_{\mu\nu}(k) + iD^0_{\mu\alpha}(k)(-i)\Pi^{\alpha\beta}(k)iD^1_{\beta\nu}(k). \tag{A.48}$$

Here $D^1_{\mu\nu}(k)$ is the one-loop vector boson propagator and $-i\Pi^{\mu\nu}$ is the sum of the one-loop fermion diagram and its counterterm,

$$\Pi^{\mu\nu} = \gamma^{\mu\nu} - \beta_2^v(k^\mu k^\nu - g^{\mu\nu}k^2) = \Pi(k^2)[\frac{k^\mu k^\mu}{k^2} - g^{\mu\nu}], \tag{A.49}$$

where

$$\Pi(k^2) = \frac{k^2}{\pi^2}N\int_0^1 dx\, x(1-x)\log\left(\frac{M^2 - k^2x(1-x)}{M^2}\right). \tag{A.50}$$

Note that the explicit dependence on the number of fermion species, N, has been inserted.

Inserting

$$D^1_{\mu\nu}(k) = (\frac{k_\mu k_\nu}{m_v^2} - \frac{k_\mu k_\nu}{k^2})(\frac{-1}{k^2 - m_v^2 + i\epsilon}) + (\frac{k_\mu k_\nu}{k^2} - g_{\mu\nu})D^1(k^2) \tag{A.51}$$

into Eq. A.37 gives

$$D^1(k^2) = \frac{-1}{k^2 - m_v^2 + i\epsilon} + \frac{-1}{k^2 - m_v^2 + i\epsilon}\Pi(k^2)D^1(k^2) \tag{A.52}$$

that implies

$$D^1(k) = \frac{-1}{k^2 - m_v^2 - \Pi(k^2) + i\epsilon}. \tag{A.53}$$

The pole of the propagator is at m_{phys} that is given implicitly by

$$m^2_{\text{phys}} = m_v^2 + \Pi(m^2_{\text{phys}}). \tag{A.54}$$

If the physical mass is known, then Eq. A.54 allows the appropriate value of the mass parameter defined at zero external momentum (m_v) to be determined.

Appendix B
Derivative Expansions

This appendix outlines the method for calculating derivative expansions of the effective action. The general methods are discussed in [43] and we present here a brief summary. In particular, we outline the method for calculating the boson-loop corrections to the Lagrangian

$$\mathcal{L} = \frac{1}{2}\partial_\mu\phi\partial^\mu\phi - V(\phi) \tag{B.1}$$

in n space-time dimensions. Recall from Chapter 2 that the one-loop effective action is given by

$$\begin{aligned} S_{\text{eff}} = \frac{1}{2}[&\operatorname{Tr}\log(\partial^\mu\partial_\mu + M^2(x)) \\ &- \operatorname{Tr}\log(\partial_\mu\partial^\mu - M^2)] + \mathcal{L}_{\text{ct}}, \end{aligned} \tag{B.2}$$

where $M^2(x) = V''(\phi)$. If $M^2(x)$ is independent of x, then $\partial^\mu\partial_\mu + M^2(x))$ is diagonal in momentum space and the trace in Equation B.2 is easily performed using momentum eigenstates. This yields minus the effective potential, $-V_{\text{eff}}(M^2(x))$. When $M^2(x)$ depends on x, then $\partial^\mu\partial_\mu + M^2(x))$ is not diagonal in either momentum or real space and evaluating the trace is more difficult. Nonetheless, since the momentum dependence is known, it is possible to develop an efficient method for calculating this trace perturbatively in derivatives of $M^2(x)$. The method proceeds as follows.

The trace relative to a constant field (for convenience chosen to be $M^2(0)$) can be written as

$$\begin{aligned} &\mathrm{Tr}\Big[\log(\partial^\mu\partial_\mu + M^2(0) + \delta M^2(x)) - \partial^\mu\partial_\mu + M^2(0))\Big] \\ &\quad = \int_0^1 dz\,\mathrm{Tr}\frac{1}{\partial^\mu\partial_\mu + M^2(0) + z\delta M^2(x)}\delta M^2(x), \end{aligned} \tag{B.3}$$

where

$$\delta M^2(x) = M^2(x) - M^2(0). \tag{B.4}$$

The result of this calculation will be the total effective action minus the effective potential evaluated at $M^2(0)$. Inserting position and momentum eigenstates, the trace can be evaluated as

$$\begin{aligned} &\mathrm{Tr}\frac{1}{\partial^\mu\partial_\mu + M^2(0) + z\delta M^2(x)}\delta M^2(x) \\ &= \int d^n x \frac{d^n p}{(2\pi)^n}\frac{d^n p'}{(2\pi)^n}\langle x|p'\rangle\langle p'|\frac{1}{\partial^\mu\partial_\mu + M^2(0) + z\delta M^2(x)}|p\rangle\langle p|x\rangle\delta M^2(x) \\ &= \int d^n x \frac{d^n p}{(2\pi)^n}\langle x|p\rangle\frac{1}{-p^2 + M^2(0) + z\delta M^2(i\frac{\partial}{\partial p})}\langle p|x\rangle\delta M^2(x) \\ &= \int d^n x \frac{d^n p}{(2\pi)^n}\frac{1}{-p^2 + M^2(0) + z\delta M^2(x + i\frac{\partial}{\partial p})}\delta M^2(x). \end{aligned} \tag{B.5}$$

The third equality follows from using the translation property of the momentum eigenstates to commute $\langle p|x\rangle$ to the left where it multiplies $\langle x|p\rangle$ to give 1.

The preceding tricks are the necessary tricks for formally evaluating the trace. The derivative expansion follows from a straightforward Taylor expansion. Let us define the effective Lagrangian by

$$S_{\text{eff}} = \int d^n x \mathcal{L}_{\text{eff}} \tag{B.6}$$

and the z dependent propagator

$$G(z) = \frac{1}{p^2 - M^2(0) - z\delta M^2(x)}. \tag{B.7}$$

This allows us to write the Taylor series expansion as

$$\frac{2}{i}(\mathcal{L}_{\text{eff}}(x) + V_{\text{eff}}(M^2(0))) =$$
$$-\int_0^1 dz \int \frac{d^n p}{(2\pi)^n} \sum_{n=0}^{\infty} z^n \Big[G \sum_{m=1}^{\infty} \frac{i^m}{m!} (\partial_{\mu_1} \cdots \partial_{\mu_m} \delta M^2(x)) \frac{\partial^m}{\partial p_{\mu_1} \cdots \partial_{\mu_m}} \Big]^n G\delta M^2(x). \tag{B.8}$$

Observe that the computational burden simply involves calculating derivatives of G and then performing the p and z integrals that are integrals of inverse polynomials that are straightforward to evaluate.

Since the effective action is translationally invariant, it suffices to evaluate the above expression at $x = 0$. In this case, most of the terms in Equation B.8 play no role. Only terms that involve as many powers of $\delta M^2(x)$ as differential operators contribute. For instance, consider calculating the second-order contribution to the derivative expansion in $1+1$ dimensions for a background field that varies in space. The only second order contributions are from the $n = 1, m = 2$ and $n = 2, m = 1$ terms. The $m = 1, n = 2$ contribution has the form

$$\left(\frac{dM^2(x)}{dx}\right)^2 \left(\frac{\delta M^2(x)}{[M^2(0)]^3} + \mathcal{O}(\delta^2)\right) \tag{B.9}$$

and hence does not contribute at $x = 0$. On the other hand, the $n = 1, m = 2$ contribution has the form

$$\frac{d^2 M^2(x)}{dx^2} \left(\frac{\delta M^2(x)}{[M^2(0)]^2} + \mathcal{O}(\delta^2)\right) \tag{B.10}$$

that after integrating by parts becomes

$$-\left(\frac{dM^2(x)}{dx}\right)^2\left(\frac{1}{[M^2(0)]^2}+\mathcal{O}(\delta)\right). \tag{B.11}$$

This contributes at $x=0$. Explicitly evaluating this contribution yields

$$\mathcal{L}_{\text{eff}}(0)+V_{\text{eff}}(M^2(0))=-\frac{1}{96\pi}\frac{1}{[M^2(0)]^2}\left(\frac{dM^2(x)}{dx}\Big|_{x=0}\right)^2+\mathcal{O}(\partial^4) \tag{B.12}$$

that implies

$$\mathcal{L}_{\text{eff}}(x)+V_{\text{eff}}(M^2(x))=-\frac{1}{96\pi}\frac{1}{[M^2(x)]^2}\left(\frac{dM^2(x)}{dx}\right)^2+\mathcal{O}(\partial^4). \tag{B.13}$$

The derivative expansion that we need in this thesis is for the fermion-loop contribution in the Walecka model that can be written as

$$S_{\text{eff}}=-i\text{Tr}\log\left(i\gamma^\mu\partial_\mu-M^*(x)-g_v\gamma^\mu V_\mu(x)\right)+\mathcal{L}_{\text{ct}}, \tag{B.14}$$

where $M^*=M-g_s\phi$ and the trace is over two species of fermions. Using the above technique the effective Lagrangian is evaluated to be [27]

$$\begin{aligned}\mathcal{L}_{\text{eff}}+V_{\text{eff}}(\phi)=&-\frac{1}{4\pi^2}g_s^2\log\left(\frac{M^*}{M}\right)\partial_\mu\phi\partial^\mu\phi\\&+\frac{1}{12\pi^2}g_v^2\log\left(\frac{M^*}{M}\right)G_{\mu\nu}G^{\mu\nu}\\&+\frac{1}{80\pi^2}g_s^2\left(\frac{1}{[M^*]^2}\right)(\partial^2\phi)^2\\&-\frac{1}{60\pi^2}g_v^2\left(\frac{1}{[M^*]^2}\right)(\partial_\alpha G^{\alpha\mu})(\partial^\beta G_{\beta\mu})\\&+\mathcal{O}(\frac{1}{[M^*]^4}),\end{aligned} \tag{B.15}$$

where $G_{\mu\nu}=\partial_\mu V_\nu-\partial_\nu V_\mu$. Here the renormalization has been performed at zero external momentum, meaning that a Taylor series expansion of (B.15) about zero does not contain any terms that would be renormalizable in the Lagrangian. This effective Lagrangian can also be used for different renormalization schemes as discussed in the last section of Appendix A.

Appendix C
Analytic Evaluation of Loop Corrections

In certain special cases it is possible to deduce the loop energies analytically. We present an especially straightforward method that is due to [44] to calculate boson-loops. Using the formalism developed in Chapter 3, it is possible to evaluate the loop energy if we know the bound states and continuum phase shifts of an equation of the form

$$[-\nabla^2 + V(x)]\eta_n = \omega_n^2 \eta_n, \tag{C.1}$$

where $V(x) = (M^*(x))^2 - M^2$.

Suppose we know that the energies of the bound states are $\{\omega_i\}$. Then if the potential is reflectionless, the continuum phase shift is uniquely determined by the bound states to be

$$\delta(k) = 2 \sum_i \arctan\left[\frac{M \sin(\theta_i)}{k}\right], \tag{C.2}$$

where

$$\theta_i = \arccos\left(\frac{\omega_i}{M}\right) \tag{C.3}$$

and $k^2 = \omega^2 - m^2$. In addition, recall that the counterterm energy is proportional to $\int (M^*)^2 - M^2$. This integral can be explicitly evaluated in terms of the θ_i as

$$\int_{-\infty}^{\infty} dx\, M^*(x)^2 - M^2 = -4M \sum_i \sin\theta_i. \tag{C.4}$$

Putting all this together the boson-loop energy,

$$E_{\rm bl} = \frac{1}{2}\sum_i(\omega_i - M) + \lim_{\Lambda\to\infty}\Big[-\frac{1}{2\pi}\int_M^\Lambda \delta(\omega)d\omega + E_{\rm ct}(\Lambda)\Big], \qquad (C.5)$$

is explicitly

$$E_{\rm bl} = -\frac{M}{\pi}\sum_i(\sin\theta_i - \theta_i\cos\theta_i). \qquad (C.6)$$

Hence, any time that we have reflectionless potentials, we can calculate the boson-loop corrections analytically. In particular, the classical kink soliton yields a reflectionless potential. The kink soliton has two bound states with energies $\omega_i = 0$ and $\sqrt{3}m/2$ corresponding to theta parameters $\theta_i = \pi/2$ and $\pi/6$ from which the phase shifts and energy follow. These results can also be used for fermion-loop problems when the potential that appears in the second-order equations for the upper and lower components involves a reflectionless potential. Such a situation occurs when fermions are coupled to the classical kink soliton solution, for example.

Appendix D
Numerical Methods

This appendix lists the various numerical methods used in this thesis. The first section describes the solution of various meson equations, both with and without source terms. The following section describes the techniques used for solving the Dirac equation in 1 and 3 spatial dimensions. In general, our methods involve discretizing the problem on a lattice and using various finite difference schemes.

D.1 Solving Meson Equations

First consider solving for the meson fluctuation modes. In $1+1$ dimensions these modes obey an equation of the form

$$\Big[-\frac{d^2}{dx^2}+\omega^2-M^2(x)\Big]\eta(x)=0, \tag{D.1}$$

where $M^2(x)\to M^2$ as $x\to\infty$ and $M^2(x)=M^2(-x)$. The solutions are classified by their parities, implying the boundary conditions

$$\begin{aligned}\eta_{\rm odd}(0)&=0\\ \eta'_{\rm odd}(0)&=c\end{aligned} \tag{D.2}$$

and

$$\begin{aligned}\eta_{\rm even}(0)&=c\\ \eta'_{\rm even}(0)&=0,\end{aligned} \tag{D.3}$$

where c is an arbitrary constant. Using these boundary conditions, Equation (D.1) can be integrated out from the origin by discretizing η on a lattice and using an

appropriate algorithm. We use the fifth-order Numerov algorithm [45] that relates the value of a function at one lattice point to its values at the two previous lattice points

$$\eta^{n+1} = f_N(\eta^n, \eta^{n-1}). \tag{D.4}$$

For a lattice with the $i = 0$ lattice point corresponding to zero, the boundary conditions at zero are implemented by

$$\begin{aligned} \eta^0_{\text{odd}} &= 0 \\ \eta^1_{\text{odd}} &= c \end{aligned} \tag{D.5}$$

and

$$\begin{aligned} \eta^0_{\text{even}} &= 0 \\ \eta^1_{\text{even}} &= f_N(\eta^0_{\text{even}}, \eta^{-1}_{\text{even}}) \\ &= f_N(\eta^0_{\text{even}}, \eta^1_{\text{even}}). \end{aligned}$$

Observe that η^1_{even} is determined implicitly from the Runge-Kutta algorithm.

The continuum solutions ($\omega^2 > M^2$) are produced by integrating out from the origin. We are interested in the phase shifts. These are determined by comparing the zeros of the exact solution with the zeros of the free solutions, which are simply sines and cosines. Explicitly,

$$\begin{aligned} \delta_{\text{odd}} &= \lim_{n\to\infty} n\pi - kx_n \\ \delta_{\text{even}} &= \lim_{n\to\infty} (n - \frac{1}{2})\pi - kx_n \end{aligned}, \tag{D.6}$$

where x_n is the nth zero of the continuum solution with $x > 0$ and $k = \sqrt{\omega^2 - M^2}$. Numerically, the phase shifts are determined by evaluating Eq. (D.6) at successive n until convergence is obtained. For the exponentially falling potentials that we study, such convergence occurs rapidly beyond the boundary of the potential.

The bound-state solutions occur at discrete energies corresponding to those solutions that obey the boundary condition

$$\eta(x) = \exp(-\kappa x) \ , \ x \to \infty. \tag{D.7}$$

These energies are found by simultaneously integrating a solution out from the origin as discussed above and by integrating a solution inwards from infinity that obeys the boundary condition, Eq. (D.7). The two solutions are then normalized to be equal at some point x_{match} and their derivatives are compared. The bound-state solutions are found when the derivatives are equal. It is easily verified that all solutions are found by checking the number of nodes in each solution and making sure that they increase by one from solution to solution.

The above techniques can also be used in $3+1$ dimensions where we need to solve equations of the form

$$\Big[\frac{d^2}{dr^2} + \omega^2 - \frac{l(l+1)}{r^2} - M^2(r)\Big]\eta_l(r) = 0. \tag{D.8}$$

Here,

$$\begin{aligned} \eta_l(0) &= 0 \\ \eta_l'(0) &= c \end{aligned} \tag{D.9}$$

so that the methods used for the odd solutions in one spatial dimension generate all the solutions needed in three dimensions. Since the phase shift in the l^{th} partial wave is defined by $\eta_l(x) \to \sin(kx - l\pi/2 + \delta_l)$ as $x \to \infty$, the phase shifts are calculated by

$$\delta_l = \lim_{n\to\infty} n\pi - kx_n + \frac{l\pi}{2}. \tag{D.10}$$

More efficient calcuations can be performed by using the zeros (u_n) of the exact free-continuum solutions $(j_l(u_n) = 0)$ in terms of which

$$\delta_l = \lim_{n\to\infty} u_n - kx_n. \tag{D.11}$$

We now turn to the solution of meson field equations with source terms. These equations need to be solved when determining self-consistent solutions. For $1+1$ dimensional solitons, the equation to be solved is

$$-\frac{d^2}{dx^2}\phi_{\rm cl} + V'(\phi_{\rm cl}) = S_f(\phi_{\rm cl}), \tag{D.12}$$

where S_f is the scalar density of the fermions that depends implicitly on $\phi_{\rm cl}$ through the dependence of the fermion sector on $\phi_{\rm cl}$. The boundary conditions obeyed by the soliton are

$$\begin{aligned} \phi_{\rm cl}(0) &= 0 \\ \phi_{\rm cl}(\infty) &= M. \end{aligned} \tag{D.13}$$

First, consider the case $S_f = 0$ that corresponds to the classical soliton. Equation (D.12) can be written as

$$h(\phi_{\rm cl})\phi_{\rm cl} = 0, \tag{D.14}$$

where

$$h(\phi) = -\frac{d^2}{dx^2} + \frac{V'(\phi)}{\phi}. \tag{D.15}$$

Note that $V'(\phi)/\phi$ exists at $\phi = 0$ for all physical potentials. This non-linear equation is solved iteratively using the imaginary time-step technique [46],

$$\phi_{(n+1)} = [1 - \lambda h(\phi_n)]\phi_n, \tag{D.16}$$

where the subscript denotes the iteration number, which for λ not too large projects out the lowest eigenvalue of h, subject to the desired boundary conditions. This generates the classical solution on the given sized lattice we are using. Denote this solution $\phi^0_{\rm cl}$ and define $\eta(x)$ by $\phi_{\rm cl} = \phi^0_{\rm cl} + \eta$. The boundary conditions on $\eta(x)$ are that it vanishes at $x = 0$ and $x = \infty$. In the presence of a source term, S_f, η obeys

$$-\frac{d^2}{dx^2}\eta + V'(\phi_{\rm cl}) - V'(\phi^0_{\rm cl}) = S_f(\phi_{\rm cl}) \tag{D.17}$$

that can be rewritten

$$-\frac{d^2}{dx^2}\eta(x) + V''(\phi^0_{\rm cl})\eta(x) = S_b(\phi_{cl}) + S_f(\phi_{\rm cl}), \tag{D.18}$$

where

$$S_b(\phi_{\rm cl}) = -V'(\phi_{\rm cl}) + V'(\phi^0_{\rm cl}) + V''(\phi^0_{\rm cl})\eta(x). \tag{D.19}$$

We discretize the second derivative in Equation (D.18) using the standard three-point formula. The discretized operator $-d^2/dx^2 + V''(\phi^0_{\rm cl})$ is a tridiagonal matrix that can be efficiently inverted [45]. This generates the iteration scheme

$$\eta^{(n+1)} = \frac{1}{-\frac{d^2}{dx^2} + V''(\phi^0_{\rm cl})}\left[S_f(\phi^{(n)}_{\rm cl}) + S_b(\phi^{(n)}_{\rm cl})\right] \tag{D.20}$$

that works effectively for the problems that we consider.

In our three-dimensional work we need to solve equations of the form

$$-\nabla^2\phi + M^2\phi = S_f(\phi) \tag{D.21}$$

for spherically symmetric meson fields, in which case this equation can be written

$$-\frac{1}{r}\frac{d^2}{dr^2}r\phi(r) + M^2\phi(r) = S_f(\phi). \tag{D.22}$$

The operator on the left hand side can be inverted by using the Green's function appropriate to the boundary conditions of an expoentially decaying solution at infinity and a finite solution at the origin [23], implying

$$\phi(r) = \int_0^\infty dr' \, (r')^2 S_f(r') G(r, r'), \tag{D.23}$$

where

$$G(r, r') = \frac{1}{Mrr'} \sinh(Mr_<) \exp(-Mr_>). \tag{D.24}$$

Here $r_<$ is the smaller of r and r' and $r_>$ is the greater of the two. The integral in Equation (D.23) is performed numerically on a lattice using Simpsons rule.

D.2 Solving the Dirac Equation

In $1+1$ dimensions the Dirac equation for fermions coupled to a scalar field can be written as the set of coupled linear differential equations

$$\begin{aligned} \frac{dF}{dx} &= g\phi F + \omega G \\ \frac{dG}{dx} &= -\omega F - g\phi G. \end{aligned} \tag{D.25}$$

We integrate this equation by discretizing it on a lattice and using a fourth-order Runge Kutta algorithm [19] that can be schematically written as

$$\begin{pmatrix} F_{n+1} \\ G_{n+1} \end{pmatrix} = M_{\mathrm{RK}}(\phi_{n+1}, \phi_{n+1/2}, \phi_n) \begin{pmatrix} F_n \\ G_n \end{pmatrix}. \tag{D.26}$$

Here the subscripts denote lattice points. Observe that the meson field needs to be computed on a lattice twice as fine as the fermion lattice. In practice the meson field is calculated on the same sized lattice as the fermions, and the values at the intermediate points are calculated by interpolation.

Since the equation is first order, the only boundary conditions we need are the values of F and G at the origin. For an antisymmetric scalar field, F and G have definite and opposite parities. Hence, the solutions obey one of the two boundary conditions

$$\begin{aligned} F(0) &= 0 \\ G(0) &= c \end{aligned} \tag{D.27}$$

or

$$\begin{aligned} F(0) &= c \\ G(0) &= 0. \end{aligned} \tag{D.28}$$

For a symmetric scalar field, the linear combinations $F+G$ and $F-G$ have definite and opposite parities, implying that the boundary conditions are

$$F(0) = G(0) \tag{D.29}$$

and

$$F(0) = -G(0). \tag{D.30}$$

The continuum solutions are generated by integrating these boundary conditions out from the origin. The phase shifts of the even and odd components are determined as in the previous section. The bound states are determined by matching solutions generated by integrating out from the origin and in from infinity. If $g\phi(x) \to M$ as $x \to \infty$, then the boundary condition is

$$\frac{F}{G} = -\frac{M - \sqrt{M^2 - \omega^2}}{\omega}. \tag{D.31}$$

Now consider the Dirac equation in $3+1$ dimensions coupled to spherically symmetric scalar and vector fields,

$$\left[i\gamma\cdot\nabla - M + S(r) + \gamma^0 V^0\right]\psi = \gamma^0\omega\psi. \tag{D.32}$$

The angular and spin dependence can be factored out (see Section 4.2) leaving a set of coupled first-order equations for the radial part of the upper and lower components,

$$\begin{aligned}\frac{d}{dr}G(r) + \frac{\kappa}{r}G(r) - \alpha(\omega,r)F(r) &= 0\\ \frac{d}{dr}F(r) - \frac{\kappa}{r}F(r) + \beta(\omega,r)G(r) &= 0,\end{aligned} \tag{D.33}$$

where

$$\begin{aligned}\alpha(\omega,r) =& \omega + M - V^0(r) - S(r)\\ \beta(\omega,r) =& \omega - M - V^0(r) + S(r),\end{aligned} \tag{D.34}$$

and κ is a non-zero integer that specifies the total angular momentum of the state and the orbital angular momentum of the individual components. Both F and G must vanish at the origin, and for r near zero their behavior is determined by the κ terms as long as the scalar and vector potentials stay finite. In this case the solutions near zero satisfy for $\kappa > 0$,

$$\frac{G}{F} = \frac{\alpha(\omega,0)}{2\kappa+1}r \tag{D.35}$$

and for $\kappa < 0$,

$$\frac{F}{G} = \frac{\beta(\omega,0)}{2\kappa-1}r. \tag{D.36}$$

In our numerical calculations, these boundary conditions are imposed on the first lattice point corresponding to $r > 0$. The differential equation (D.33) is integrated using the Runge-Kutta algorithm. In order to determine the bound states, we also need to integrate in from infinity where the boundary condition is

$$\frac{G}{F} = -\sqrt{\frac{M-\omega}{M+\omega}} \tag{D.37}$$

and match the solution with one integrated out from the origin.

References

[1] A. Fetter and J. Walecka, *Quantum Theory of Many Particle Systems*(McGraw-Hill,New York, 1971).

[2] C. Itzykson and J. Zuber, *Quantum Field Theory* (McGraw-Hill,New York, 1980).

[3] R. F. Dashen, B. Hasslacher, and A. Neveu, Phys. Rev. **D10**, 4114 (1974);**D10**, 4130 (1974).

[4] H. B. G. Casimir, Proc. Kon. Ned. Akad. Wetenshap. **B51**, 793 (1948).

[5] W. Greiner, B. Müller, and J. Rafelski, *Quantum Electrodynamics of Strong Fields* (Springer-Verlag, Berlin, 1985).

[6] A. Iwazaki and S. Kumano, University of Illinois preprint ILL-(TH)-88-8 (1988); Y. S. Hirata and H. Minakata, Tokyo Metropolitan University preprint TMUP-HEL-8819 (1988); C. J. Horowitz, Indiana University preprint IU/NTC 88-19 (1988).

[7] R. K. Bhaduri, *Models of the Nucleon*(Addison-Wesley, Redwood City, CA, 1988).

[8] L. S. Celenza, B. Rosenthal, and C. M. Shakin, Phys. Rev. **C31**,232 (1985); U. G. Meissner, Phys. Lett. **B220)**, 1 (1989).

[9] B. D. Serot and J. D. Walecka, Adv. in Nucl. Phys. **16**,1 (1986).

[10] J. Iliopolous, C. Itzykson, and A. Martin, Rev. Mod. Phys. **47**, 164 (1975).

[11] P. Ramond, *Field Theory: A Modern Primer* (Benjamin, Reading, MA, 1981).

[12] S. Coleman and E. Weinberg, Phys. Rev. **D7**, 1888(1973).

[13] G. Ripka and S. Kahana, Phys. Lett. **155B**, 327(1985); R. J. Perry, Nucl. Phys. **A467**, 717(1987).

[14] M. Li, R. J. Perry, and L. Wilets, Phys. Rev. **D36**, 596(1987); M. Li and R. J. Perry, Phys. Rev. **D37**,1670(1988).

[15] C. J. Horowitz and B. D. Serot, Phys. Lett. **140B**, 181 (1984).

[16] R. J. Perry, University of Washington preprint 40048-24-N7 (1987);T. D. Cohen, M. K. Banarjee, and C.-Y. Ren, Phys. Rev. **C36**, 1653 (1987).

[17] Eugen Merzbacher, *Quantum Mechanics*(Wiley, New York, 1970).

[18] R. Rajaraman, *Solitons and Instantons* (North-Holland, Amsterdam, 1987).

[19] M. Abramowitz and J. Stegun, *Handbook of Mathematical Functions*(Dover, New York, 1969).

[20] A. Messiah, *Quantum Mechanics* (North-Holland, Amsterdam, 1961).

[21] G. Baym, *Lectures on Quantum Mechanics* (Benjamin/Cummings, Reading, Mass, 1969).

[22] B. C. Clark, S. Hama, R. Mercer, L. Ray, and B. Serot, Phys. Rev. Lett. **50**, 1644 (1983).

[23] C. J. Horowitz and B. D. Serot, Nucl. Phys. **A368**, 503 (1981).

[24] R. Machleidt, K. Holinde, and Ch. Elster, Phys. Rep. **149**,1 (1987).

[25] R. J. Furnstahl, C. E. Price, and G. E. Walker, Phys. Rev. **C36**, 2590 (1987).

[26] S. A. Chin and J. D. Walecka, Phys. Lett. **52B** (1974) 24.

[27] R. J. Perry, Phys. Lett. **182B** (1986) 269 and Nucl. Phys. **A467** (1987) 717.

[28] R. J. Furnstahl, R. J. Perry, and B. D. Serot, Indiana University preprint IU/NTC 88-18 (1988).

[29] H. J. Pirner, Phys. Lett. **85B**(1979)190.

[30] R. Brockmann and W. Weise, Phys. Lett. **69B** (1977)167. J. Boguta and J. Bohrmann, Phys. Lett. **102B**(1981)93.

[31] H. Ruta , H. Stöcker, P.G. Reinhard, J. Maruhn, and W. Greiner, J. Phys. **G13**(1987)143.

[32] Y. Jin and D. S. Only, Phys. Rev. **C38**, 813 (1988).

[33] N. Auerbach , A. Goldhaber, M. Johnson, L. Miller, and A. Picklesimer, Phys. Lett. **182B** (1986)221.

[34] D. Marlow *et al.*, Phys. Rev. **C25**(1982)2619.

[35] P. B. Siegel, W. B. Kaufmann, and W. R. Gibbs, Phys. Rev. **C31**(1985)2184.

[36] G. E. Brown, C. B. Dover, P. B. Siegel, and W. Weise, Phys. Rev. Lett **60**(1988)2723.

[37] B. C. Clark, private communication.

[38] T. D. Cohen, Phys. Lett. B (1988).

[39] E. Kiritsis and R. Seki, Caltech preprint MAP-117 (1988); T. D. Cohen, University of Maryland preprint 89-127 (1989).

[40] H. Kurasawa and T. Suzuki, Phys. Lett. **B208**, 160 (1988).

[41] D. Griegel and T. Cohen, University of Maryland preprint 89-068 (1988).

[42] Xiangdong Ji, Caltech preprint MAP-110 (1988); C. J. Horowitz, Indiana University preprint IU/NTC 88-4 (1988).

[43] L. H. Chan, Phys. Rev. Lett. **54**, 1222 (1985); **55**, 21 (1985); O. Cheyette, Phys. Rev. Lett. **55**, 2394 (1985).

[44] K. Cahill, A. Comtet, and R. Glauber, Phys. Lett **64B**, 283 (1976).

[45] S. E. Koonin, *Computational Physics* (Benjamin/Cummings, Menlo Park, CA, 1986).

[46] K. T. R. Davies, H. Flocard, S. Krieger, and M. S. Weiss, Nucl. Phys. **A342**, 111 (1980).